The Effects of Surface Free Energy on the Aqueous Processing of $LiNi_{0.5}Mn_{1.5}O_4$ Cathodes

Zur Erlangung des akademischen Grades eines

Doktors der Ingenieurwissenschaften (Dr.-Ing.)

von der KIT-Fakultät für Maschinenbau
des Karlsruher Instituts für Technologie (KIT)

angenommene

Dissertation

von

M.Eng. Andreas Weber

Hauptreferent:	Prof. Dr. rer. nat. Christian Greiner
Koreferent:	Prof. Dr. rer. nat. Helmut Ehrenberg
Prüfungsvorsitz:	Prof. Dr.-Ing. Frederik Zanger

Tag der mündlichen Prüfung: 05.06.2025

Affidavit

I hereby confirm that this thesis is the result of my own work. All sources and/or materials applied and used in and for this thesis are listed and quoted. The statutes for Safeguarding Good Research Practice of the KIT have been respected and followed.

Furthermore, I confirm that this thesis has not yet been submitted as part of another examination process neither in identical nor in similar form.

Karlsruhe, 12.03.2025

Kurzfassung

Diese Dissertation untersucht die wässrige Verarbeitung von Lithium-Nickel-Mangan-Oxid ($LiNi_{0,5}Mn_{1,5}O_4$, LNMO) in positiven Elektroden für Lithium-Ionen-Batterien (LIB) unter Verwendung von wasserverarbeitbaren oder -löslichen Bindemitteln zur Verbesserung der mechanischen Eigenschaften und der elektrochemischen Leistung von LIBs.

Im ersten Kapitel werden die Grundlagen für diese Arbeit gelegt und durch Vorbehandlung des Aktivmaterials der Einfluss des Eintauchens in Wasser auf LNMO untersucht. Die Untersuchungen zeigen, dass LNMO in reinem und angesäuertem Wasser zur Auslaugung von Lithium sowie von Mangan- und Nickelionen bei Phosphorsäurezusatz neigt. Die Auslaugung verhindert den Einsatz von Polyvinylidenfluorid-Latices, da die resultierende Konzentration an mehrwertigen Ionen eine schnelle Koagulation der Latices auslöst. Eine Verarbeitung im sauren Milieu führt somit aufgrund der Koagulate zu massiven Beschichtungsdefekten. Das Eintauchen in reines Wasser führt hingegen zu einem vorteilhaften Entfernen von resistiven Oberflächenverunreinigungen – Rückstände von Kalium, Natrium, Schwefel und Sauerstoff –, was zu einer Verbesserung der Rateneigenschaften der Kathoden führt. Obwohl es durch die Zugabe von H_3PO_4 zur Bildung von kristallinem Li_3PO_4 kommt, welches die Langzeit-Kapazitätserhaltung fördert, schränkt der damit verbundene Verlust von Lithium- und Übergangsmetall-Ionen die Verwendung in der wässrigen LNMO-Verarbeitung ein.

Ein Hauptaugenmerk der Arbeit liegt auf der Untersuchung des Einflusses der freien Oberflächenenergie auf die Eigenschaften von Kathoden. Der erste Teil der Untersuchung beschäftigt sich mit Leitadditiven und bewertet die Wechselwirkungskräfte zwischen den Elektrodenbestandteilen durch Berechnung der freien Oberflächenenergien. Die Ergebnisse zeigen, dass die freie Oberflächenenergie des Leitadditivs eine entscheidende Rolle bei der Verteilung des Binders innerhalb der Elektrode spielt. Es wurde eine bevorzugte Adhäsion der verwendeten Carboxymethylcellulose und des Polyvinylidenfluorid-Latex an Leitadditiv-Oberflächen mit maßgeblich dispersiver freier Oberflächenenergie beobachtet, was zu ausgeprägten Kohlenstoff-Binder-Domänen und einer geschwächten mechanischen Integrität aufgrund der begrenzten freien Verfügbarkeit des Bindemittels führt. Es wurden zwei Ansätze zur Verbesserung der Adhäsionskraft ermittelt: die Verkleinerung der Leitadditiv-Oberfläche zur Erhöhung der freien Polymerverfügbarkeit und die Verwendung von Kohlenstofffasern mit geringerer Binderaffinität. Neben der höheren Adhäsion, verbessern die eingesetzten Kohlenstofffasern die Zyklenstabilität, da sie aufgrund ihrer geringeren spezifischen Oberfläche weniger Reaktionsstellen für parasitäre Elektrolytreduktion bieten.

Darüber hinaus wurde untersucht, wie sich der Einsatz von Polyvinylidenfluorid-Latexbindern mit variierenden Oberflächenenergie-Beiträgen auf die Elektrodeneigenschaften auswirkt. Ein Latex mit einem hohen polaren Beitrag weist eine gleichmäßigere Verteilung innerhalb der Kathode auf, was zu einer größeren Haftfestigkeit auf Kosten eines erhöhten Grenzflächen- und Volumenwiderstandes, aufgrund der isolierenden Wirkung der Latexpartikel, führt. Die Untersuchung zeigt auch, dass Latices mit höherer Polarität ein höheres

Wasserrückhaltevermögen aufweisen, was sich auf die langfristige Kapazitätserhaltung auswirkt, da Restwasser die Bildung einer ausgeprägten Feststoff-Elektrolyt-Grenzfläche verstärkt. Durch eine verstärkte Trocknung können diese Unterschiede jedoch minimiert und eine Kapazitätserhaltung von ca. 70 % über 1000 Zyklen bei allen getesteten Kathoden erreicht werden. Dies deutet darauf hin, dass hochpolare PVDF-Latices bei angemessener Trocknung verbesserte Haftungseigenschaften bieten.

Der dritte Teil der Untersuchungen zur freien Oberflächenenergie betrachtet den Einfluss des Aluminiumstromsammlers. Hierfür wurde unter Einsatz verschiedener wasserlöslicher Binder die Oberflächenenergie des Stromsammlers gezielt durch eine Coronabehandlung modifiziert. Die Behandlung hat eine Verbesserung der Benetzbarkeit durch die wässrigen Pasten zur Folge. Durch intensive Behandlung der Aluminiumfolie sinkt der Kontaktwinkel der Paste um 50-60°. Es zeigt sich jedoch auch, dass hohe Intensitäten der Coronabehandlung zu einer Abnahme der Haftfestigkeit der Kathode führt, da sie zu einer verstärkten Wechselwirkung des Aluminiums mit Wasser, jedoch einer verringerten Wechselwirkung mit den Bindemitteln, führt.

Durch Anwendung und Kombination aller Erkenntnisse konnten LNMO-Kathoden mit hoher Aktivmaterial-Beladung (3,8 mAh/cm²), hoher Haftung (27,8 N/m), geringem spezifischem Widerstand (1,72 Ω·cm) und moderater Tortuosität (3,00) hergestellt werden. Elektrochemische Tests zeigen vergleichbare Rateneigenschaften zu Kathoden mit niedriger Aktivmaterial-Beladung (1,9 mAh/cm²), bis zu einer C-Rate von 1 C. Coronabehandlung (25,5 J/cm²) der Kathode führte zu deutlich verbesserter Ratenfähigkeit, in besonderem Maße bei höheren C-Raten. Unter Einsatz der Elektrolyt-Additive LiBOB und TMSP erzielen die Elektroden eine Kapazitätserhaltung von 80 % über 1000 Zyklen.

Diese Arbeit liefert wesentliche Erkenntnisse zur wasserbasierten Verarbeitung von LNMO und identifiziert optimale Bedingungen für Adhäsion, Leitfähigkeit und Langzeit-Kapazitätserhaltung zur Herstellung hochleistungsfähiger Kathoden für Lithium-Ionen-Batterien.

Abstract

This dissertation investigates the aqueous processing of lithium nickel manganese oxide ($LiNi_{0.5}Mn_{1.5}O_4$, LNMO) in positive electrodes for lithium-ion batteries (LIB) using water-processable or -soluble binding agents to enhance the mechanical properties and electrochemical performance of LIBs.

A primary objective was to assess the influence of submersion in pure and acidified water on LNMO, which was found to facilitate the leaching of lithium-ions, as well as manganese and nickel ions when exposed to phosphoric acid. This leaching impedes the use of polyvinylidene fluoride (PVDF) latices, as the resultant multivalent ion concentration triggers rapid coagulation, rendering acidified processing unviable. Submersion in pure water, however, led to a beneficial removal of resistive surface impurities – identified as residues of potassium, sodium, sulfur, and oxygen – that improved the electrode's rate capabilities. Thus, while acidification forms crystalline Li_3PO_4 species improves long-term capacity retention, its associated lithium and transition metal loss restricts its use in aqueous LNMO processing.

The study further evaluated the interaction forces among electrode constituents by calculating interfacial free energies. Findings indicate that surface free energy (SFE) of the conductive additive (CA) plays a pivotal role in binder distribution within the electrode. Preferential binder adhesion to CA surfaces with highly dispersive SFE was observed, leading to pronounced carbon-binder domains (CBDs) and weakened mechanical integrity due to limited free binder availability. Two approaches to enhance adhesion strength were identified: reduction of CA surface area to increase free polymer availability, and the use of vapor-grown carbon fibers (VGCFs) with lower binder affinity. Beyond improved adhesion, VGCFs enhanced cycling stability by offering less reaction sites for parasitic electrolyte reduction   .

Furthermore, it was investigated how SFE components of PVDF latex binders impact electrode properties. A latex with a high polar component displayed uniform distribution across slurry components, yielding strong adhesive strength at the expense of increased interface and bulk resistivity due to the insulating nature of latex particles. Analysis also showed that latices with higher polarity retain more water, impacting long-term cycling performance by promoting pronounced solid-electrolyte interphase (SEI) formation. However, extended drying mitigated these differences resulting in capacity retentions of approx. 70 % across all tested cathodes, suggesting that high-polarity PVDF latices offer improved adhesion if adequately dried.

Corona treatment of aluminum current collectors was tested to investigate the impact of the current collectors SFE on aqueous slurry wetting and electrode adhesion. Intense treatment improved wettability, lowering the contact angle by 50° - 60° through increased slurry-current collector interaction. However, adhesion strength benefitted only from low-intensity treatment. High-intensity treatment resulted in an increasingly stronger interaction of the current collector with water at the expense of the interaction with the binders which effectively resulted in a lower adhesion strength.

Finally, combining these findings enabled the production of robust high-loading LNMO cathodes (3.75 mAh/cm²) with excellent adhesion (27.8 N/m), low bulk resistivity (1.72 Ω cm), and moderate tortuosity (3.00). Electrochemical tests showed that these cathodes perform comparably to low-loading counterparts up to 1C, with enhanced rate capability at higher C-rates following corona treatment at 25.5 J/cm². Additionally, additives LiBOB and TMSP improved long-term stability, achieving 80% capacity retention over 1000 cycles. This work advances the understanding of aqueous processing for LNMO, identifying optimal conditions for adhesion, conductivity, and lifetime of cathodes suitable for high-performance lithium-ion batteries.

Table of Contents

List of Illustrations

List of Tables

List of Abbreviations

AM	Active Material
CA	Conductive Additive
CB	Carbon Black
CBD	Carbon Binder Domain
CC	Current Collector
CCCV	Constant Current Constant Voltage
CELEST	Center for Electrochemical Energy Storage
CMR	Carcinogenic, Mutagenic and Toxic to Reproduction
DIM	Diiodo Methane
DMSO	Dimethyl Sulfoxide
DSA	Drop Shape Analysis
EDS	Energy Dispersive X-ray Spectroscopy
EG	Ethylene Gylcol
EIS	Electrochemical Impedance Spectroscopy
IAM	Institute of Applied Materials
ICP-OES	Inductively Coupled Plasma Optical Emission Spectroscopy
KIT	Karlsruhe Intitute of Technology
LIB	Lithium-Ion Battery
LFP	Lithium Iron Phosphate
LNMO	Lithium Nickel Manganese Oxide
NMC	Lithium Nickel Manganese Cobalt Oxide
NMP	N-Methyl-2-Pyrrolidone
N/P	Negative to Positive Electrode Capacity Ratio
OWRK	Owens-Wendt-Rabel-Kälble

PSE	Personal Safety Equipment
PVDF	Polyvinylidene Fluoride
SEM	Scanning Electron Microscopy
SFE	Surface Free Energy
VGCF	Vapor Grown Carbon Fibers
vOCG	van Oss-Chaudhury-Good

Acknowledgement

1 Introduction

According to the European Commission the transportation sector is predicted to experience significant growth in the passenger vehicle fleet until 2050 which makes it the only industrial sector to increase in the emission of greenhouse gases. [1–3] Concerning the EU, transportation accounted for 29.2 % of CO_2 emissions and 29.2 % of the overall energy consumption in 2021. [1] Thus, a change from internal combustion engine vehicles to electric vehicles, which allow for the usage of renewable energy, is highly incentivized. As a consequence the demand for various energy storage systems has surged over the last decades, with particular focus on high energy density LIBs. [2] The manufacturing process of batteries has been thoroughly optimized throughout recent years. As the required production capacity is expected to continuously increase within the next decades the further reduction of manufacturing cost and energy consumption remain highly pertinent subjects of interest. [4]

The state-of-the-art manufacturing process of positive electrodes is still based on the application of NMP due to its good PVDF solubility. PVDF is a widely established binder as it offers a high dispersion quality in the slurry, good electrolyte wettability, and great electrochemical stability during cycling. [5–7] The major disadvantages of NMP are its high material cost and its reproductive toxicity leading to its classification as a CMR (carcinogenic, mutagenic, and toxic to reproduction) substance which in turn necessitates large capital investments to ensure work safety, appropriate waste gas treatment and solvent recovery.

Aqueous processing of negative electrodes for LIBs has been extensively investigated and industrially established for over a decade. [8,9] Research of positive electrodes has particularly focused on industrially established active materials such as lithium nickel manganese cobalt oxide (NMC) and lithium iron phosphate (LFP) [10–12]. There still exists a deficit of knowledge and experience in the water-based processing of promising, yet industrially less established, materials. One such material is lithium nickel manganese oxide ($LiNi_xMn_yO_4$, LNMO), which offers excellent properties as a cathode active material, as for example a nominal cell voltage of 4.7 V (vs. Li^+/Li) and a theoretical capacity of 147 mAh/g. Due to the high nominal cell voltage, LNMO offers a specific energy density of 464 Wh/kg (based on realistic graphite full cell capacities of 120 mAh/g). Therefore, it surpasses both current state-of-the-art active materials $LiNi_{0,6}Mn_{0,2}Co_{0,2}O_2$ (NMC 622) and $LiNi_{0,8}Mn_{0,1}Co_{0,1}O_2$ (NMC 811) delivering 416 Wh/kg and 448 Wh/kg, respectively. LNMO offers further advantages as the ability to be fully lithiated and delithiated during the discharging and charging process without experiencing structural damage. [13] Moreover, LNMO is free of highly debated cobalt and fully exploits the redox capacity of nickel. This results in material cost savings of 50 % which translate to 10-20 % savings at cell-level. [14] However, the favorable high potential of LNMO (up to 5.0 V vs. Li/Li+) imposes high requirements on the electrochemical stability of the applied materials. Concerning the conductive additive, several authors have demonstrated that carbon blacks suffer from limited stability at voltages beyond 4.5 V leading to instable cathode-electrolyte interface (CEI) and solid-electrolyte interface (SEI) formation in full cells. [15–18] The issue of insufficient oxidative stability also extends to the polymeric binders. One of the most commonly applied latex binders in both water-

based anode and cathode systems, styrene–butadiene–rubber (SBR), was shown by several authors to be electrochemically oxidized above 4.3 V due to C=C double bonds in its structure. It was further demonstrated that both CMC and PVDF are oxidatively stable as they are saturated polymers. [19,20] New developments have enabled the transfer of non-water soluble PVDF's favorable properties to water-based cathodes. Through synthesizing the PVDF via emulsion polymerization and stabilizing the primary particles by the use of various surfactants an aqueous suspension of colloidal PVDF particles can be obtained, which allows for its application in aqueous processing, thus, rendering the usage of NMP obsolete. [21]

Yet, there is still a variety of issues to be solved with regard to water-borne cathodes. These issues include the corrosion of the current collector as a result of high slurry pH values, agglomeration effects leading to coating defects, and low mechanical integrity of the final electrode. Water-based cathodes further suffer from inferior electrochemical performance as well as unfavorable degradation mechanisms of the active material while submerged in water during processing. [22–24] This work will address the aforementioned issues divided into the following chapters:

1. Submersion of LiNi$_{0.5}$Mn$_{1.5}$O$_4$ in Water

The first investigative chapter is dedicated to the research of the effect of aqueous submersion on LNMO and serves to establish a baseline for this work. There are several publications addressing the challenge of high slurry pH values. Following the approach of pH neutralization by addition of phosphoric acid according to Kuenzel et al. [24], particular focus of the investigation was on the leaching behavior of the lithium and transition metal ions and its subsequent impact on slurry processability and electrochemical performance.

2. Surface Free Energy in Aqueous Processing of LiNi$_{0.5}$Mn$_{1.5}$O$_4$ Cathodes

The main focus of this work is on addressing the low mechanical integrity of water-based systems as it is one of the most frequently mentioned drawbacks of water-borne electrodes in literature holding relevance for both anodes [25–27] as well as cathodes [28–30]. Employing the methodology of surface free energy, the influence of varying surface energies on adhesion as well as other key electrode properties will be investigated. The chapter is, therefore, further subdivided into the investigation of the carbon additive, the PVDF latex binder, and the aluminum current collector.

3. Manufacturing of High-Loading LiNi$_{0.5}$Mn$_{1.5}$O$_4$ Cathodes

The final chapter serves as demonstration, combining the findings made throughout this work, to manufacture an aqueously processed LNMO cathode with an industrially relevant high areal loading of 3.75 mAh/cm² or 25.5 mg/cm².

2   Theory

This chapter provides a concise review and summary of the theoretical background relevant to this work. The design and functionality of lithium-ion batteries are discussed to provide a general understanding of the roles of various battery components and their impact on overall battery performance. An overview of the current state-of-the-art electrode manufacturing process is also presented, highlighting its advantages and limitations. Given that these topics are generally well-known to the target audience, the summaries are intentionally brief. To give an introduction into adhesion, the different conventional adhesion theories are presented. The main focus of this work, the influence of surface free energy on aqueous processing, is then summarized. Starting with the historical evolution of the theory, different models are introduced. The model applied throughout this work is then discussed in great detail and contrasted with a newer less-established method.

2.1   Lithium-Ion Batteries

2.1.1 Design

Lithium-ion batteries are secondary batteries, where charge transfer is based on lithium-ions involved in fully reversible redox reactions. All LIBs consist of the same five main components: casing, cathode, separator, anode, and electrolyte. [31] Besides the main parts several other complementary pieces are used to ensure the proper positioning of the main components in the cell, such as spacers or springs, in coin cells, or as processing aids during assembly, e.g. winding mandrels, in cylindrical cells. [32]

Figure 1 illustrates two of the most commonly used cell designs, the coin cell and the pouch cell. While the coin cell's main application is in laboratory scale research and small electronic devices, pouch cells come into use in all application fields ranging from small mobile applications, such as smartphones, over large mobile applications, such as electric vehicles, to large stationary energy storage systems, e.g. grid balancing. There it shares its place with two other established cell formats, the cylindrical and the prismatic cell. As of 2021, the market share of each format is highly dependent on the country of origin with China, being the main manufacturer of battery cells, producing around 78 % of prismatic cells with respect to China's total production capacity. In comparison, the predominant format in Europe is the pouch cell with approx. 60 % and regarding the US market cylindrical cells have a share of roughly 73 %. [32]
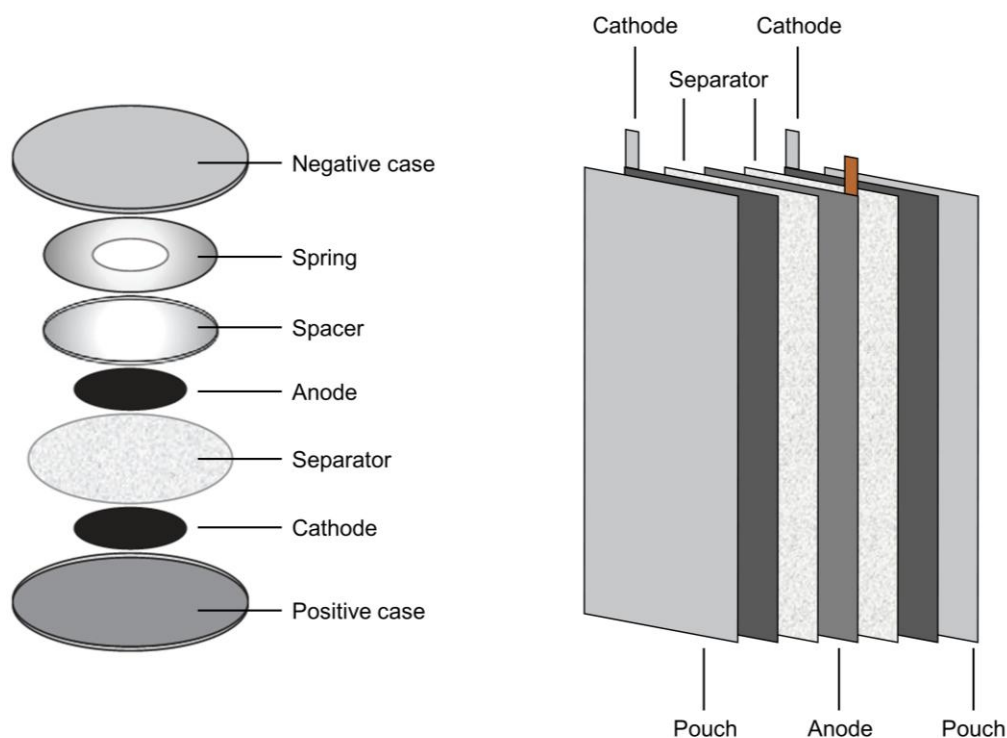
Figure 1 - Schematic of a coin cell (left) adapted from Murray et al. [33] and a pouch cell (right) adapted from Yoo et al. [34]

At the core of the cell is the electrochemical couple, consisting of the anode and cathode. The anode, typically made from graphite, serves as the host for lithium-ions during the discharge process, while the cathode, often composed of a lithium metal oxide such as lithium nickel manganese cobalt oxide ($LiNi_xMn_yCo_{1-x-y}O_2$) or lithium iron phosphate ($LiFePO_4$), acts as the lithium source during charging. The electrodes are coated onto a metallic foil acting as current collector, usually aluminum on the cathode side and copper on the anode side. They are either in direct contact with the case or with connectors outside the case to allow for electric charge transfer as soon as connecting an electric device closes the circuit. Separating the anode and cathode is the separator, a microporous polymer membrane that physically isolates anode and cathode to prevent electrical short circuits while allowing ionic transport. All three components are soaked with electrolyte, a lithium-ion-conducting medium that enables the movement of ions between the electrodes during charge and discharge cycles. The electrolyte is usually a liquid organic solvent containing a lithium salt, such as lithium hexafluorophosphate ($LiPF_6$), which provides the necessary ionic conductivity. The cell components are housed within a protective casing that shields the internal elements from environmental factors and provides structural integrity. Each component is precisely customizable from the size and shape of the case to the exact chemical composition of cathode, anode, or electrolyte to fit the desired final application. [31,35]

2.1.2 Operating Principle

Current state-of-the-art rechargeable LIBs are often based on intercalation active materials, where positively charged lithium-ions are released or intercalated from the active material crystal structure. The principle behind the charge transfer is called the rocking chair principle. The charge carriers, namely Li^+ in LIBs, shuttle from the positive to the negative electrode and vice versa during operation, while not significantly affecting the composition of the electrolyte. [36,37] Besides Li^+, a variety of rocking chair batteries relying on other metal ions, e.g. Na^+, K^+, Zn^{2+}, and Al^{3+}, or non-metal ions, e.g. NH^{4+} and Cl^-, as charge carriers has emerged over the last few years. [31,37] Figure 2 schematically illustrates the processes of charge transfer inside a generalized LIB.
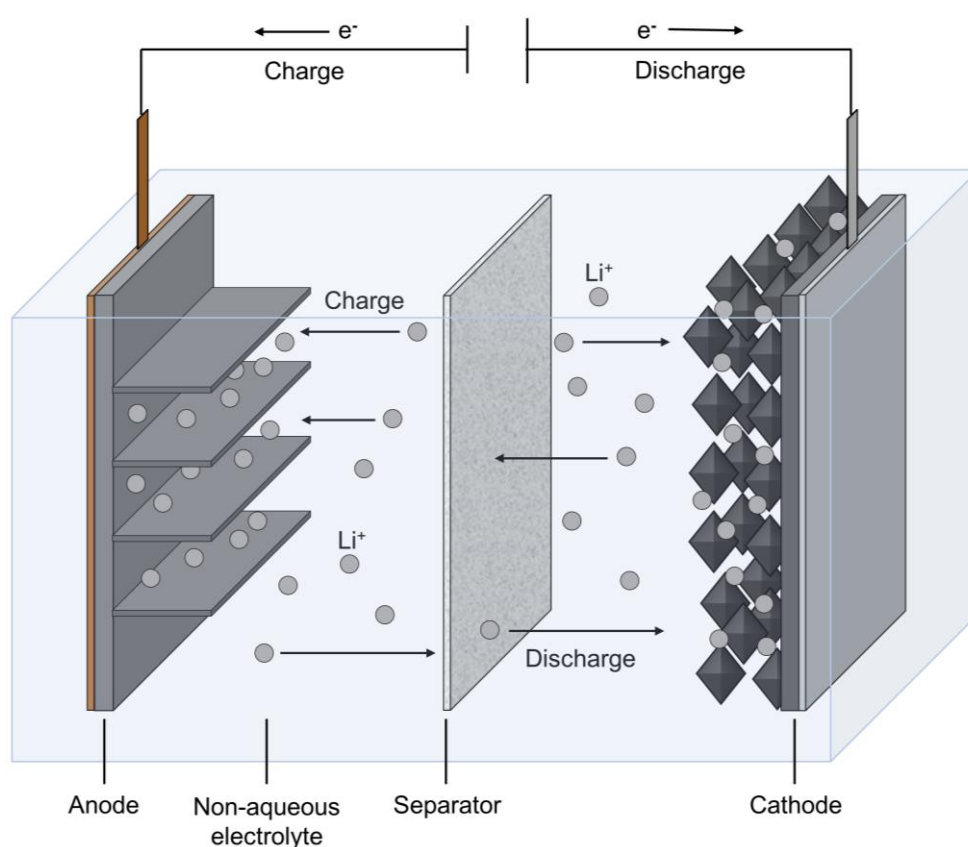
Figure 2 - Schematic of the charge transfer mechanism inside a LIB during charging and discharging adapted from Ghiji et al. [38]

For the charge reaction to take place electric charge is needed while the discharge reaction releases the electric charge. In both cases the electrons are conducted through an external connection given that either a charging device or an electronic consumer is closing the circuit between anode and cathode, forcing or enabling the flow of an electric current, respectively. Simultaneously, diffusion of the lithium-ions takes place through both the electrolyte and separator to the respective electrode. Two redox reactions govern the the charge transfer mechanism: during discharging the lithium-ions are reduced at the cathode, while during charging the reduction of the lithium-ions takes place at the anode. The individual charge reactions for an exemplary lithium

metal oxide at the cathode and graphite as anode active material are summarized in Equations 1-3: [35–37]

Cathode:

$$LiMO_2 \rightleftharpoons Li_{1-x}MO_2 + x\, Li^+ + x\, e^- \tag{1}$$

Anode:

$$C_6 + y\, Li^+ + y\, e^- \rightleftharpoons Li_y C_6 \tag{2}$$

Overall:

$$LiMO_2 + \frac{x}{y} C_6 \rightleftharpoons \frac{x}{y} Li_y C_6 + Li_{1-x}MO_2 \tag{3}$$
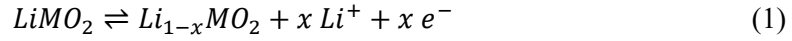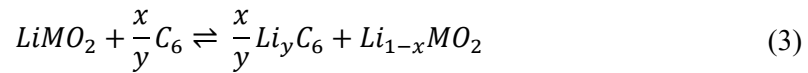
Herein, the individual active materials in use and their standard free Gibbs energy determine the exact reaction equation and further the voltage of the generated current. Moreover, the standard free Gibbs energy of the redox couple dictates the energy i.e. potential required to induce the intercalation of lithium-ions into the active material on the anode side. As theoretically the same amount of energy is released during discharge, with current LIBs having a coloumbic efficiency of often more than 99.98 %, a vast difference in standard free Gibbs energy of anode and cathode allows for a higher energy density. [36,37]

2.1.3 Electrode Structure

Both cathode and anode are composite materials consisting of several constituents. The active material (AM) provides and hosts the lithium-ions which travel from cathode to anode during charging and vice versa during the discharge procedure. Both act as reactants in the intercalation reaction with each material exhibiting its characteristic redox reactions. The conductive additive (CA) creates electronic percolation pathways enabling the transfer of electrons to the reaction sites. Several different types of CA have been established in the manufacturing of electrodes. The variety ranges from high surface area carbon blacks, graphene or carbon nanotubes to low surface area carbon fibers or graphite. Each of them comes with their own unique set of benefits and challenges. As illustrated in Figure 3, the binding agent has to fulfill a multitude of tasks.
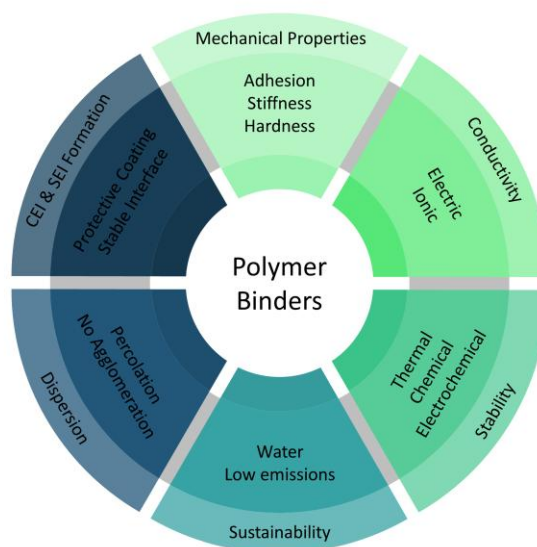
Figure 3 - Desired properties of water-processable polymer binders used in electrode manufacturing adapted from Cholewinski et al. [39]

The most important one is the formation of a mechanically stable bond towards all other of the other components and the current collector (CC), thereby ensuring both cohesive and adhesive strength. It is further used as a dispersing agent to properly deagglomerate the CA in the slurry and is sometimes described in literature to function as a protective coating on the active material, preventing unwanted side reactions. [23] The majority of polymer binders are electronically insulating, essentially impeding the flow of electrons through the electrode. By addition of a sufficiently high amount of CA to the electrode and proper deagglomeration or distribution of the CA, the percolation threshold can be exceeded, rendering the entire network electrically conductive. The structures of intermingled CA and binder are generally referred to as carbon-binder-domains (CBD). While it is crucial to provide a sufficiently high electric conductivity, the incorporation of excessive amounts of CA is also disadvantageous as they lead to low mechanical integrity of the electrode. [40] Overall, large amounts of both CA and binder not only decrease the energy density of the electrode but also result in the reduction of the residual electrode porosity which in turn leads to a lessened ionic conductivity and thus worse performance of the electrode. This ultimately necessitates a trade-off between mechanical strength and electric conductivity which translates to a precisely balanced amount and ratio of CA and binder. [41] In Figure 4 the microstructure of an electrode as described is schematically illustrated.
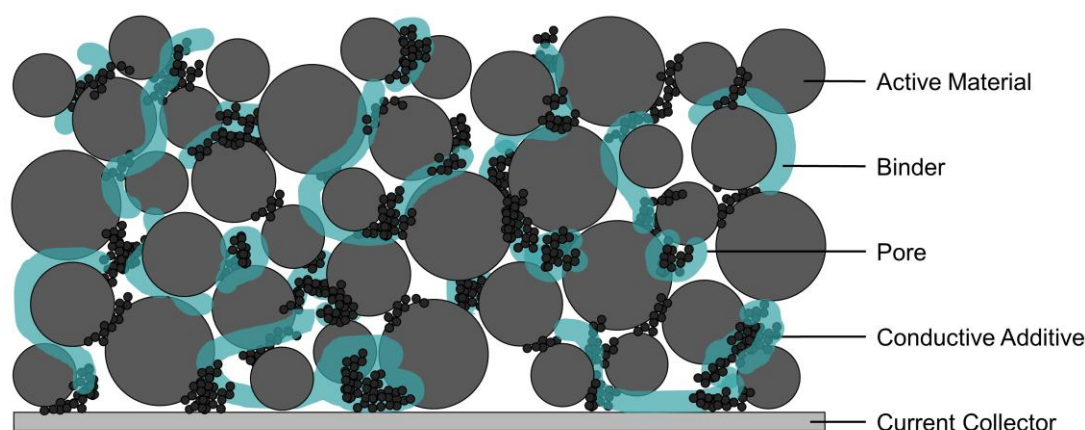
Figure 4 - Schematic of the microstructure of an electrode comprised of active material, binder and conductive additive coated onto a metallic current collector adapted from Gyulai [42]

2.1.4 Manufacturing

The state-of-the-art manufacturing of electrodes has been for many years and still is based on the coating of slurries. While the process has been greatly optimized over the last two decades, the process design itself remains identical. [43] Starting with the preparation of the slurry, the binder is first dissolved in harmful N-Methyl-2-pyrrolidone (NMP) which still represents the current state-of-the-art solvent for homogeneous and stable slurries. [9] Subsequently, the AM and the CA are dispersed in the solution where the polymer binder acts as a dispersant. The resulting viscous slurry is then coated onto a current collector in a roll-to-roll coating line at web speeds ranging from 30 m/min to 100 m/min at industrial scale. The slurries can either be coated by slot die extrusion or doctor-blade achieving superior electrode quality at the aforementioned high web speeds. [43,44] Concluding the electrode manufacturing process is the drying in a series of convection ovens, where evaporation and recovery of the solvent vapor takes place. The entire process chain of LIB manufacturing includes several subsequent steps, such as calandering, secondary drying, cutting, stacking, assembling, and formation, which are all equally important for the final performance of the LIB. The process is schematically illustrated in Figure 5 listing the advantages of aqueous over the organic solvent-based processing. The described setup has been optimized to reduce scrap, maximize web speed and therefore reduce overall manufacturing cost.

Solvent	Mixing	Coating	Drying	Distillation
NMP	Handling requires ventilation and PSE	Controlled environment necessary	Solvent vapor must not be released into atmosphere	Required to recycle expensive solvent
Water	Handling of powders requires only PSE	Can be carried out in air	No recovery needed	Not needed
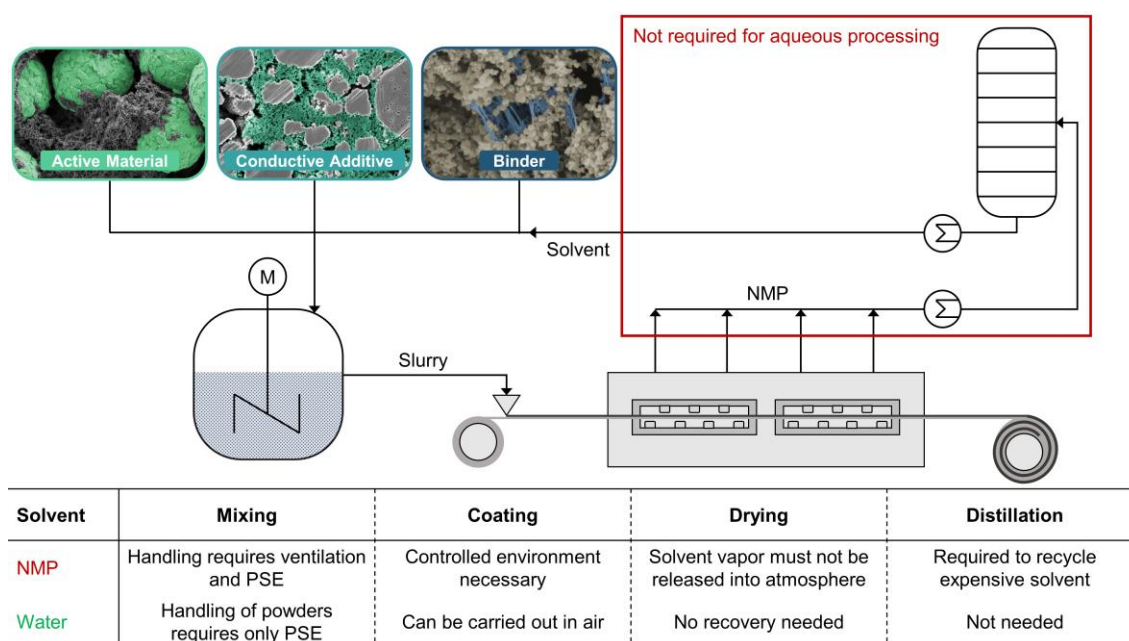
Figure 5 - Schematic comparison of the organic solvent-based and the water-based manufacturing process of electrodes adapted from Bresser et al. [8]

The optimization potential, however, is limited as the major drawbacks of this process arise from the necessity to evaporate the required solvent. Liu et al. [9] states that 47 % of the overall energy consumption can be accounted for by solvent recovery which translates to nearly 5 % of the LIBs cost. Based on a cost breakdown by Wood. et al. [45] the substitution of NMP by water offers the by far largest potential for cost savings without requiring changes to the process design. The use of NMP comes at high material (1-3 $/kg) as well as environmental and occupational safety and health cost. Due to its reproductive toxicity and consequently its classification as a CMR (carcinogenic, mutagenic and toxic to reproduction) substance, the NMP vapor is first recovered and then distilled to be reused in slurry preparation. Both process steps entail large capital investments and operating costs. [9] Over the last decade water has gained increasingly more attention in slurry preparation and coating as it offers not only significantly lower material cost (0.015 $/L) but also renders the need for solvent recovery and distillation obsolete. [8] Additionally, it can easily be observed on lab and pilot scale that water-borne electrodes dry significantly faster than NMP-based ones. In fact, Susarla et al. [46] reported that aqueously processed electrodes dry approx. 4.5 times faster while simultaneously requiring around 10 times less energy compared to NMP-processed electrodes. The finding is based on the equilibrium vapor pressure of water being 35 times lower than that of NMP, which corresponds to the considerably lower boiling point (100 °C vs. 203 °C). This is particularly in view of the fact that the latent heat of vaporization of water is 4 times greater than for NMP. With regard to negative electrodes, aqueous processing has been established at an industrial scale for over a decade. [8,9] Yet, water-based processing of cathodes still poses a variety of challenges as for example high pH values of the slurries and thus corrosion of the metallic current collector, deterioration of the AM upon water contact, agglomeration effects or poor mechanical strength. [22–25,29]

2.1.5 Polyvinylidene Fluoride Latices

PVDF latices, i.e. a dispersion of PVDF in an aqueous medium, have emerged as a significant innovation in the production of LIB electrodes. [47] These latices are typically synthesized via emulsion polymerization. In this process vinylidene fluoride monomers are dispersed in an aqueous phase and initiators, e.g. ammonium persulfate, are introduced to create reactive radicals triggering polymerization. By addition of ionic or non-ionic surfactants the dispersed monomers are stabilized to a stable emulsion. The polymerization then proceeds under regulated temperature and pressure conditions, resulting in the formation of nano-sized PVDF particles. In the final process step, the latex undergoes filtration and concentration to achieve the desired particle size distribution and solid content. [47–49] The resulting PVDF latices allow for the transfer of PVDF's beneficial properties, such as its high electrochemical stability, a good dispersion quality in the slurry, and its favorable electrolyte wettability, to aqueous processing while simultaneously diminishing one of PVDF's major drawbacks, the reliance on organic solvents, namely NMP. Thus, they offer a more environmentally friendly and cost-effective alternative to traditional PVDF binders. Moreover, several authors have demonstrated that water-based, PVDF latex containing, cathodes offer improved electrochemical performance over conventional NMP-based cathodes with conventional PVDF as binding agent. [22,50,51]

2.2   Adhesion Theories

While there is no exact agreement in literature about all the mechanisms involved in the interaction of materials. Numerous theories regarding the causes for adhesion have emerged over the years reaching from the mechanical anchoring of the coating in clefts and cavities of the substrate over contact charging or diffusion of molecules, dipole-dipole interactions, mirror forces due to polar functional groups up to chemical reactions between coating and substrate and hydrogen bridging bonds (Figure 6). [52] Assigning adhesion to solely one of the mechanisms is most often difficult as they certainly all have an effect on bond strength with each mechanism having a different impact depending on the system under investigation. [53] The five most established theories will be further elaborated on in the following chapters.
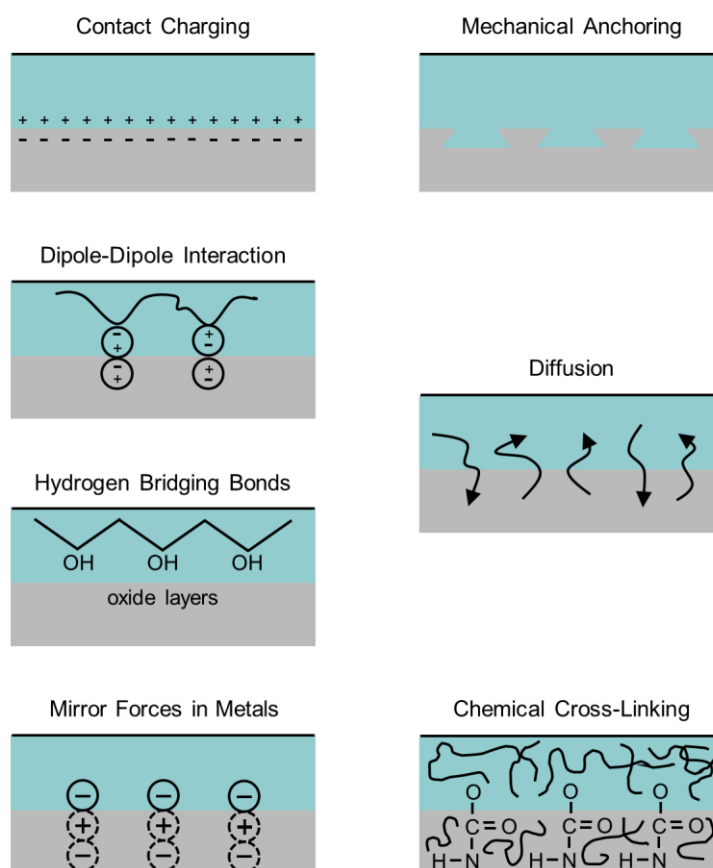
Figure 6 - Schematic of physical and chemical mechanisms behind the adhesion of coatings (green) and substrate (grey) adapted from Streitberger et al. [52]

2.2.1 Mechanical Theory

The mechanical theory of adhesion, as the earliest of theories, postulates that the bonding between two surfaces primarily arises from surface irregularities or microscopic surface roughness where an adhesive can penetrate pores, cavities, and other surface features of the substrate where it then solidifies, creating a mechanical, rather than a chemical bond or other intermolecular forces. The created mechanical bond provides resistance to both tensile and shear strength. Porous and abraded surfaces are frequently reported to form stronger adhesive bonds than smooth surfaces. Yet, it is worth noting that excessive roughness of the adherend might lead to voids at the interface, consequently weakening the adhesive bond. [54,55] Besides surface roughness there are other factors affecting mechanical adhesion, such as the viscosity and the wettability of the adhesive, the degree of deformation of the surface irregularities or the contact pressure. One of the limitations of this theory is the existence of strong bonds between smooth surfaces demonstrating that while surface roughness has an influence, it does not solely determine bond strength. It can further not be clearly distinguished whether enhanced adhesion after treatment of the adherend intended for increasing surface roughness is due to improved mechanical interlocking, cleaning of the substrate, formation of highly reactive surfaces or an increase in surface area. It is, therefore, highly debated whether mechanical interlocking itself leads to strong bonds or if the increased surface area is responsible for enhancing other adhesion mechanisms. [52,53,56]

2.2.2 Electrostatic Theory

Originally proposed by Derjaguin et al. [57], the electrostatic theory rests on the assumption of charge transfer across the interface of adhesive and adherend due to different electronic band structures. This results in the formation of electrical double layers. These electrostatic forces account for the resistance against separation of the interface. Their evidence was based on several peeling experiments in which they rapidly peeled flexible polymer films from solid substrates. Today it is a well-known dark room experiment to demonstrate the occurrence of electrical discharge during the quick removal of adhesive tapes from a glass substrate. By measuring the discharge voltage and distance as function of gas pressure, they were able to calculate the condenser discharge energy and correlate it to the measured work of adhesion. Given the fact, that no one has since tried to confirm their findings of changing peel strength in dependence of gas pressure, and that the observed phenomenon can potentially also occur while only accounting for an insignificant percentage of the measured peel strength was greatly criticized. Concerning the application of the theory on rubbery polymers, Voyutskii et al. [58] pointed out that if the assumption of electrical double layers responsible for adhesion were to be true, dissimilar polymers should be more adherend to one another than similar polymers due to higher differences in potential voltage. They further stated that according to the electrostatic theory adhesion between and towards carbon black containing polymers would be impossible due to their highly conductive nature while referencing works that demonstrated the bonding of such materials to themselves as well as metals. This led to the large neglect of the theory except in specific fields of polymer-metal adhesion bonds. [53,57,58]

2.2.3 Diffusion Theory

The diffusion theory finds its application particularly in polymeric systems. According to this theory, adhesion occurs due to the interdiffusion of molecules between the adhesive and the adherend, primarily when both materials are polymers. The distinctive difference between the other adhesion theories and the diffusion theory lies in the inclusion of polymeric substances' most characteristic properties. Characteristics, such as the chain structure, glass transition temperature, molecular weight, molecule flexibility and the ability of Brownian movement are decisive in the diffusion process which involves the movement of polymer chains across the interface. Voyutskii et al. [58] and later Derjaguin et al. [59] demonstrated that another factor influencing the extent of diffusion and, consequently, the adhesion strength is mutual solubility. They postulated the idea of judging adhesion by compatibility data and suggested the polarity of polymers as determining factor in the approximation of the compatibility. The process of diffusion results in the disappearance of a clear boundary but an interfacial layer with a typical thickness between 1 and 100 nm. In certain cases, e.g. in the presence of a solvent in which both polymers are either soluble or capable of swelling, it can even lead to the formation of a bond that is a gradual transition rather than an interface from the adhesive to the adherend. This interpenetration of polymer chains across the interface creates a physical entanglement that contributes significantly to the overall adhesive strength. Diffusion theory, therefore, considers adhesion a volume rather than an interface phenomenon. It, furthermore, accounts for the discrepancies of other theories such as the adsorption theory which lacks to explain the differences between peel work measurements and the work calculated to overcome molecular forces in polymeric adhesive bonds. [52,53,58]

2.2.4 Chemical Bonding Theory

The chemical bonding theory ascribes adhesion between two materials to the formation of chemical bonds across their interface. The prerequisition for chemical bonding is the presence of chemically reactive groups in both materials. Under certain conditions, usually good adsorption and close contact between the adhesive and the substrate, chemical reactions in the form of covalent bonds can occur. As a result, the mechanism is often referred to as chemisorption. The strength of these bonds (150-1080 kJ/mol) far exceeds that of secondary van-der-Waals forces (2-30 kJ/mol). It is generally more common in polar materials which contain hydroxyl or carboxylic acid groups. However, the overall adhesive strength is dependent upon the number of formed bonds and their respective strength.[53,56,60,61]

2.2.5 Adsorption and Wetting Theory

The adsorption or wetting theory states that adhesion is the result of the molecular contact between adhesive and adherend at their interface. Through the formation of attractive secondary van-der-Waals forces the adhesive molecules adsorb onto the substrate. The different types of intermolecular forces, ordered from highest to lowest bond energy, are as follows:

Dipole-dipole (Keesom) interaction (2-25 kJ/mol): [53]
Occurs between two permanent dipoles (polar molecules) with the positive end of one molecule attracting the negative end of another.

Hydrogen bonding (25 kJ/mol): [53]
A specific, stronger type of dipole-dipole interaction that occurs between a hydrogen atom bonded to a highly electronegative atom (F, O, N, or S) and another electronegative atom in a different molecule

Dipole-induced dipole (Debye) interaction (2-10 kJ/mol): [62]
A permanent dipole induces a dipole in a nonpolar molecule.

Fluctuating-dipole-induced-dipole (London dispersion) interaction (2 kJ/mol): [53]
Results from the instantaneous formation of dipoles (induced dipoles) due to the movement of electrons around the nuclei.

As van-der-Waals forces are highly dependent upon the distance between molecules, adhesive and adherend must make extremely close contact with only several angstroms in distance for these forces to apply. The mechanism of achieving and maintaining continuous contact between adhesive and the surface of the substrate is referred to as "wetting". There are two differentiations to make when evaluating wetting behavior. As illustrated in Figure 7, good wetting is observable when the adhesive readily flows into the irregularities and cavities of the substrate maximizing the interfacial contact area. Poor wetting results from the adhesive preferring cohesion over adhesion therefore minimizing its own surface area. This behavior then results in the adhesive bridging over the irregularities of the substrate surface leaving air pockets, which entails a reduced actual contact area between the binding agent and the adherend and ultimately leads to lower adhesion strength. [52,53,56,60]
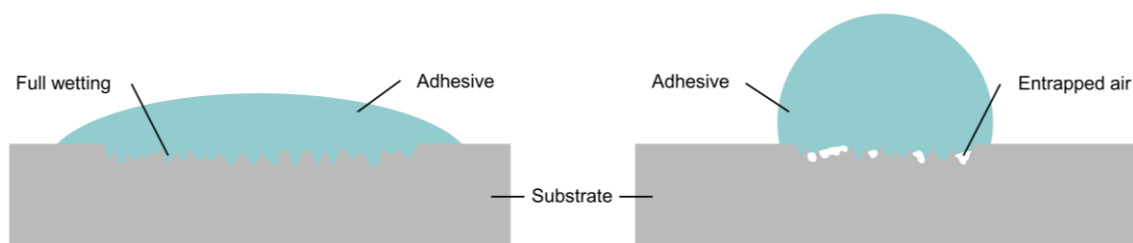
Figure 7 - Schematic of good wetting (left) where the adhesive fills all irregularities of the substrate and poor wetting (right) with the adhesive partially bridging cavities resulting in air entrapments adapted from Petrie [60]

Wetting can be quantified through the measurement of the contact angle between a drop of the adhesive and the adherend. If an adhesive spontaneously and uniformly spreads, i.e. it forms a

thin covering film, over the substrate, this is considered complete wetting and the contact angle is zero. For good wetting to take place it is essential that the surface tension of the substrate exceeds that of the adhesive as it is then energetically favorable for the adhesive to maximize the interface with the substrate. In application this leads to most organic adhesives readily wetting metal surfaces due to their high surface tensions resulting in high adhesion. The surface tension of many polymeric surfaces, however, is lower than that of common adhesives which leads to poor wetting and as a result weak adhesion strength. The concept of surface tension or surface free energy will be discussed in detail in the following chapter. [52,53,56,60]

2.3   Surface Free Energy

As of today, the surface free energy (SFE) method offers the most holistic approach in explaining interactions in colloid and interface science. [63] At the core of the method stands the contact angle which is the angle of a droplet at the three-phase boundary, i.e. the boundary of the liquid drop with a solid surface and a surrounding vapor, as visualized in Figure 8.
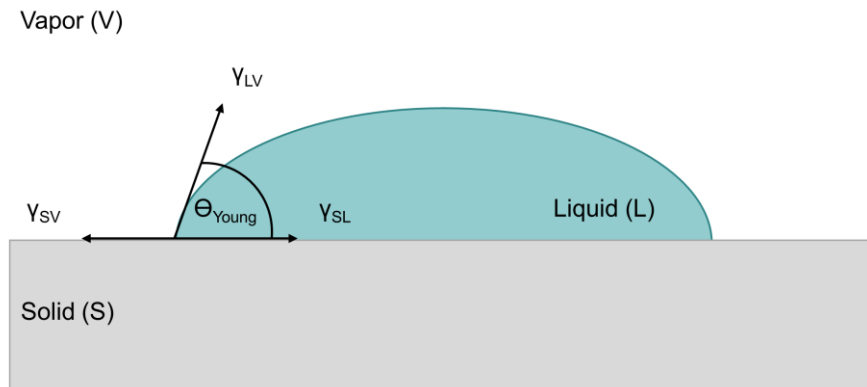
Figure 8 - Schematic of the Young contact angle at the three-phase boundary between liquid drop, solid and surrounding vapor adapted from Weber and Keim et al. [64]

By applying a tangent to the profile of the drop the contact angle can be measured. The contact angle is conventionally measured from the liquid side. It was first described by Thomas Young [65] who linked the wetting behavior of a liquid to the resulting contact angle and postulated the so-called Young's equation:

$$\theta_{Young} = \frac{\gamma_{SV} - \gamma_{SL}}{\gamma_{LV}} \tag{4}$$

Equation 4 is the expression of a force balance between the acting interfacial tensions where θ_{Young} is the Young contact angle, γ_{SL} the solid-liquid, γ_{SV} the solid-vapor, and γ_{LV} the liquid-vapor interfacial tension. Young's equation allows for the formulation of universally applicable conclusions for instance the tendency of high surface energy solids (i.e. high γ_{SV}) to form low contact angles when wetted by a liquid while low energy surfaces generally exhibit high contact angles. Young's equation is, however, limited in the regard that it only applies to atomically smooth, chemically homogeneous surfaces, which are non-deformable and do not react when in contact with the liquid drop. Real surfaces can therefore lead to discrepancies between θ_{Young} and θ_{App}, which is the apparent or measured contact angle. Figure 9 schematically visualizes the contact angle hysteresis of an ideal and a real surface. [66–68]
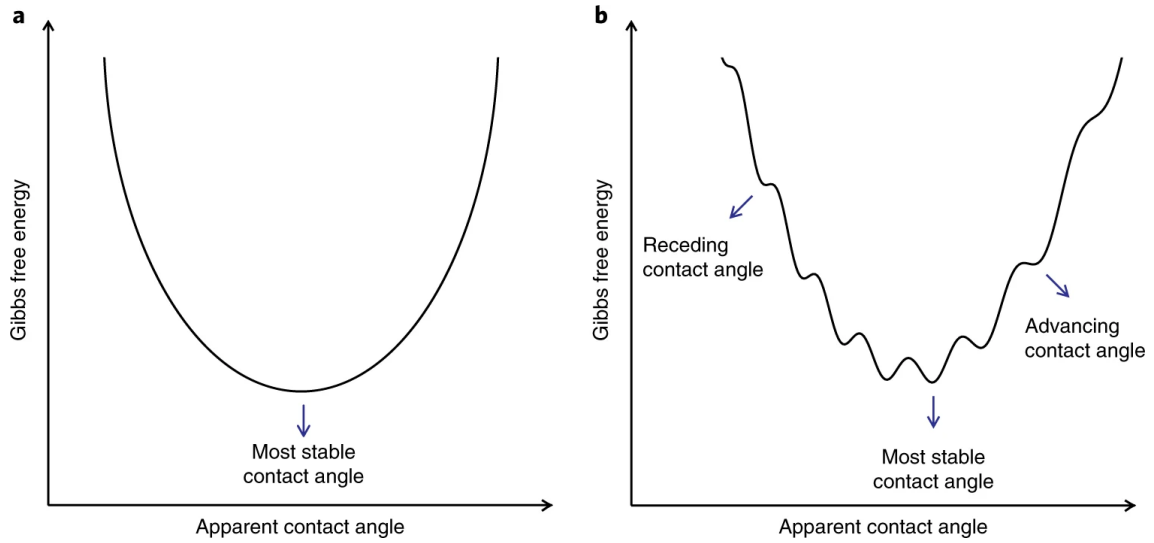
Figure 9 - Contact angle hysteresis of an ideal wetting system with only a single free energy minimum, corresponding to the Young contact angle (a) and the wetting system of a real, imperfect surface which also has only one global minimum free energy but also several metastable static contact angles (b) reproduced from Huhtamäki et al. [67]

The hysteresis is limited by the advancing and the receding contact angle. While the hysteresis of an ideal surface only exhibits one global free energy minimum which corresponds to the Young contact angle, a real imperfect surface has a global free energy minimum accompanied by several local free energy minima. [67] This leads to the possibility of measuring several different Θ_{App}. There are two possible solutions to this problem, the first one being the use of mechanical vibrations of the sample surface to overcome the energy barriers between the individual minima and the second one being multiple repetitions of the same contact angle measurement to minimize the measurement error. As demonstrated in literature, the first option yields the most accurate contact angles. [69] However, there are, as of today, no commercially available goniometers incorporating this technique, necessitating the use of repeated measurements throughout this work. Over the years several authors developed more advanced relationships to better describe the surface of real samples. The Wenzel equation for example expanded Young's equation by surface roughness of the sample. The work of Cassie and Baxter then further elaborated on the Wenzel equation by taking air inclusion between sample surface and liquid drop into account. [68] In 1869, Dupré [70] postulated the concept of reversible work of adhesion W_{SL}^{ad} between a solid and a liquid which is equal to the negative free energy of interfacial interaction ΔG_{SL}^{IF} by expessing γ_{SL} as the sum of the interfacial tensions:

$$W_{SL}^{ad} = \gamma_{SV} + \gamma_{LV} - \gamma_{SL} = -\Delta G_{SL}^{IF} \tag{5}$$

The equation is the thermodynamic expression that the separation of the liquid drop from the solid surface requires work equal to the free energy of interaction released during interface formation. Inserting the equation into Equation 4, results in the Young-Dupré equation:

$$-\Delta G_{SL} = \gamma_{LV} (1 + \cos(\theta)) \tag{6}$$

Fowkes Method

To understand surface tension in greater detail Fowkes [71–73] suggested in a theoretical consideration that the total free energy of a surface is a sum of individual contributing intermolecular forces and can therefore be partitioned into:

$$\gamma_{SV} = \gamma_{SV}^d + \gamma_{SV}^p + \gamma_{SV}^h + \gamma_{SV}^i + \gamma_{SV}^{AB} \tag{7}$$

The total surface free energy is thus comprised of dispersion interaction γ_{SV}^d, dipole-dipole interaction γ_{SV}^p, hydrogen bonding γ_{SV}^h, induced dipole-dipole interaction γ_{SV}^i, and acid-base components γ_{SV}^{AB}. In his original model Fowkes [71] then postulated the solid interfacial tension as:

$$\gamma_{SL} = \gamma_{SV} + \gamma_{LV} - 2\sqrt{\gamma_{SV}^d \cdot \gamma_{LV}^d} \tag{8}$$

The expression is true when considering a surface that only exhibits a dispersion component. After combining Equation 8 with the Young-Dupré equation this allows for determining γ_{SV} through Θ_{App}.

Owens-Wendt-Rabel-Kälble Method

Owens and Wendt [74] later expanded on the Fowkes model. Rabel [75] and Kälble [76] published similar equations shortly after. Consequently, the method was coined the OWRK method by later publications. Their works were all based on the assumption that solid and liquid surface free energy consist of a dispersion component γ^d and a polar component γ^p, arising from hydrogen-bonding and dipole-dipole interactions, which allows for the expression of γ_{SV} and γ_{LV} as:

$$\gamma_{SV} = \gamma_{SV}^d + \gamma_{SV}^p \tag{9}$$

$$\gamma_{LV} = \gamma_{LV}^d + \gamma_{LV}^p \tag{10}$$

By assuming a geometric mean form of the polar component, in parallel to the Fowkes method in Equation 8, γ_{SL} can be derived and expressed by:

$$\gamma_{SL} = \gamma_{SV} + \gamma_{LV} - 2\sqrt{\gamma_{SV}^d \cdot \gamma_{LV}^d} - 2\sqrt{\gamma_{SV}^p \cdot \gamma_{LV}^p} \tag{11}$$

Combining Equation 11 with the Young-Dupré equation results in:

$$\gamma_{LV}(1 + cos(\theta)) = 2\sqrt{\gamma_{SV}^d \cdot \gamma_{LV}^d} + 2\sqrt{\gamma_{SV}^p \cdot \gamma_{LV}^p} \tag{12}$$

Since there are only two unknown terms γ_{SV}^d and γ_{SV}^p left, they can be calculated through determining θ_{App} with at least two different liquids where both γ_{LV}^d and γ_{LV}^p are known. By rewriting Equation 12 one obtains:

$$\frac{\gamma_{LV}(1 + cos(\theta_{Young}))}{2\sqrt{\gamma_{LV}^d}} = \sqrt{\gamma_{SV}^p}\frac{\sqrt{\gamma_{LV}^p}}{\sqrt{\gamma_{LV}^d}} + \sqrt{\gamma_{SV}^d} \tag{13}$$

Plotting $\gamma_{LV}(1 + cos(\theta))/2\sqrt{\gamma_{LV}^d}$ against $\sqrt{\gamma_{LV}^p}/\sqrt{\gamma_{LV}^d}$ and performing a linear fit on the data obtained from the contact angle measurements with at least two different solvents γ_{SV}^d and γ_{SV}^p can be determined. [66,77] For higher accuracy and reliability of the fit of the data to the model, it is recommendable to perform contact angle measurements with a larger set of solvents than the two required to solve the equation. Figure 10 schematically visualizes the determination of the dispersive and polar component of a sample surface by contact angle measurement of three distinct reference liquids and subsequent application of the OWRK method. The dispersive component is then obtained from the y-intercept of the regression line and the polar component from the slope. [78]
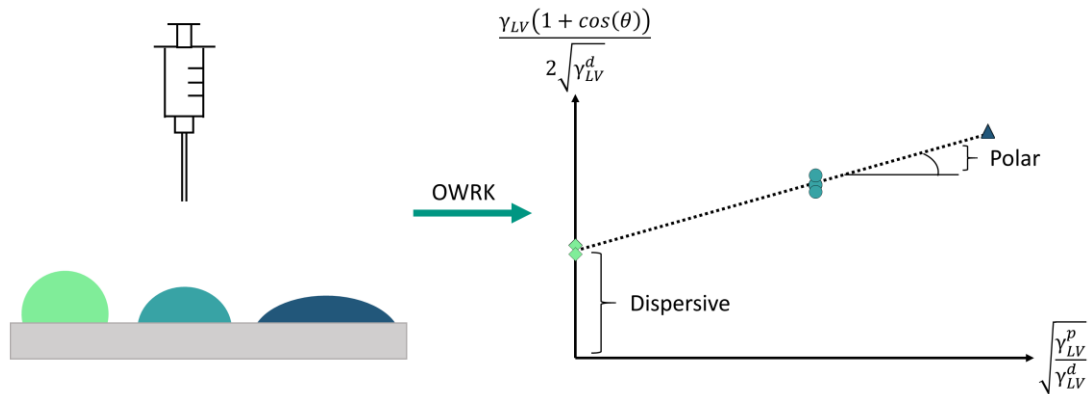
Figure 10 - Schematic of the surface free energy determination according to the OWRK method by linear regression – the reference liquids are color-coded for improved comprehension adapted from Weber and Keim et al. [64]

Kitazaki Method

Kitazaki et al. [79] expanded on the OWRK method by further partitioning the polar contribution of solid and liquid surface free energy into dipole-dipole and hydrogen-bonding interactions, designated as γ^p and γ^h, respectively and stated that:

$$\gamma_{SV} = \gamma_{SV}^d + \gamma_{SV}^p + \gamma_{SV}^h \tag{14}$$

$$\gamma_{LV} = \gamma_{LV}^d + \gamma_{LV}^p + \gamma_{LV}^h \tag{15}$$

Analogous to the OWRK method all contributions can be written as a geometric mean:

$$\gamma_{SL} = \gamma_{SV} + \gamma_{LV} - 2\sqrt{\gamma_{SV}^d \cdot \gamma_{LV}^d} - 2\sqrt{\gamma_{SV}^p \cdot \gamma_{LV}^p} - 2\sqrt{\gamma_{SV}^h \cdot \gamma_{LV}^h} \tag{16}$$

After combination with the Young-Dupré equation the three unknown terms γ_{SV}^d, γ_{SV}^p, and γ_{SV}^h can be calculated from contact angle measurements with at least three solvents with known γ_{LV}^d, γ_{LV}^p and γ_{LV}^h. However, in practical application the Kitazaki method is seldomly referenced. This leads to a lack of literature on the surface tension components of reference solvents, rendering the method impractical. [78]

van Oss-Chaudhury-Good Method

In contrast to the aforementioned authors, van Oss et al. [63,80,81] suggested a different partition of surface free energy into Lifshitz-van der Waals interactions γ^{LW} which include dipole-dipole (Keesom), induced dipole-dipole (Debye), and dispersion (London) interactions and an extended concept of polar interactions γ^{AB} comprising, besides hydrogen-bonding, all electron-acceptor-electron-donor, i.e. Lewis acid-base interactions. Thus, the solid and liquid surface tensions are expressed as:

$$\gamma_{SV} = \gamma_{SV}^{LW} + \gamma_{SV}^{AB} \tag{17}$$

$$\gamma_{LV} = \gamma_{LV}^{LW} + \gamma_{LV}^{AB} \tag{18}$$

Herein

$$\gamma^{AB} = 2\sqrt{\gamma^+ \cdot \gamma^-} \tag{19}$$

with γ^+ and γ^- being the electron acceptor (Lewis acid) and the electron donor (Lewis base) parameter, respectively. By again assuming the geometric mean form the equation becomes:

$$\gamma_{SL} = \gamma_{SV} + \gamma_{LV} - 2\sqrt{\gamma_{SV}^{LW} \cdot \gamma_{LV}^{LW}} - 2\sqrt{\gamma_{SV}^+ \cdot \gamma_{LV}^-} - 2\sqrt{\gamma_{SV}^- \cdot \gamma_{LV}^+} \qquad (20)$$

Combining with the Young-Dupré equation leaves three unknowns, namely γ_{SV}^{LW}, γ_{SV}^+, and γ_{SV}^-. Similar to the aforementioned methods, they can be calculated through experimentally determining the contact angles of three liquids with known γ_{LV}^{LW}, γ_{LV}^+, and γ_{LV}^-. Equation 17 clearly states that the LW and AB components of the surface energy are additive. Even so, γ^+ and γ^- are not additive. It is possible for a liquid or solid to exhibit only a γ^+ or a γ^- parameter. According to van Oss et al. [82] these materials are designated as monopolar. However, it becomes apparent from Equation 19 that a single parameter will not contribute to the total SFE unless the parameter of the opposite sign is present either in another part of the same molecule or in a different molecule. Consequently, γ^{AB} results in zero and therefore the total surface free energy of a monopolar material equals γ^{LW}. Yet, it is possible for monopolar materials to interact by their remaining AB parameter with bipolar materials such as water where the water molecule delivers the opposing AB parameter. A drawback of the method is the fact that there are no known absolute values of γ^+ and γ^- for any substance. To estimate the AB parameters of a material the method is reliant on an assumed value of a reference compound. Van Oss et al. [83] postulated the value of water to be $\gamma_{water}^+ = \gamma_{water}^- = 25.5$ mJ/m².

While the vOCG method is a further development step of the OWRK method, there is still no real scientific consensus on which method to use. The partition of surface free energy components according to the vOCG method provides explanations for certain, exceptional cases where the OWRK method falls short. From a practical point of view the OWRK method remains the method of choice for SFE determination in most commercially available goniometers and literature. The interpretation of the results should, however, be conducted according to vOCG. [78]

Interpretation of Results

Inversely to the work of adhesion, the affinity of two surfaces or to be more precise the tendency of two materials to spontaneously form interfaces between them can be expressed by the free energy of interfacial interaction ΔG^{IF}. Considering that, according to Fowkes [82,84], the disperse and polar components of the free energy of interfacial interaction are additive it can be stated that:

$$\Delta G^{IF} = \Delta G^d + \Delta G^p \tag{21}$$

Depending on the sign of ΔG^{IF}, it provides two indications. Positive values of ΔG^{IF} denote that particles experience repulsion. Conversely, negative values signify attraction between particles and a propensity for interface formation. [63,85] According to van Oss et al. [63,86] a distinction between several cases has to be made based on the system under investigation:

1. Free energy of cohesion of a single material 1 with

$$\Delta G_{11}^d = -2\gamma_1^d \tag{22}$$

   where ΔG^d_{11} is always negative, indicating attraction.

2. Free energy of adhesion between materials 1 and 2 (material 2 can also be a liquid) with

$$\Delta G_{12}^d = -2\sqrt{\gamma_1^d \gamma_2^d} \tag{23}$$

   where ΔG^d_{12} is always negative, indicating attraction.

3. Free energy of interaction between two surfaces of material 1, submerged in liquid 3 with

$$\Delta G_{131}^d = -2\left(\sqrt{\gamma_1^d} - \sqrt{\gamma_3^d}\right)^2 \tag{24}$$

   where ΔG^d_{131} is always negative, indicating attraction.

4. Free energy of interaction between different materials 1 and 2, submerged in liquid 3 with

$$\Delta G_{132}^d = -2\left(\sqrt{\gamma_1^d} - \sqrt{\gamma_3^d}\right)\left(\sqrt{\gamma_2^d} - \sqrt{\gamma_3^d}\right) \tag{25}$$

   where ΔG^d_{132} is positive, indicating repulsion if: $\gamma^d_1 < \gamma^d_3 < \gamma^d_2$ or $\gamma^d_1 > \gamma^d_3 > \gamma^d_2$.

Equations 22 through 25 having d as superscript are equally valid with superscript p. Equations 22 and 23 describe the direct interaction of particles of the same material and the direct interaction of two materials with each other, respectively. The conditions for direct interaction are given in dry powder mixing for dry electrode production as demonstrated by Ludwig et al. [87,88]. With regard to this work, focusing on aqueous processing of cathodes, investigating the interaction of

different electrode constituents while being immersed in water is of special interest. Therefore, equations 24 and 25 hold the most relevance for the investigations conducted in the following chapters.

3 Methods

The field of battery research includes a broad spectrum of analytical and experimental methods, each contributing to the understanding of battery performance, degradation, and efficiency. Traditionally, research in this area has predominantly focused on well-established techniques such as cyclic voltammetry [89], electrochemical impedance spectroscopy (EIS) [90], potentiostatic charge-discharge cycling [91], and inductively coupled plasma optical emission spectroscopy (ICP-OES) [92]. These methods are integral to the field and have been extensively documented in the literature, providing a robust foundation for battery characterization and analysis.

However, as battery technologies evolve and new materials and chemistries are explored, there is a growing need to apply and develop less conventional methods. These lesser-known techniques may offer unique insights, particularly in areas where traditional methods fall short or where novel challenges arise. For instance, techniques dedicated to surface free energy are beginning to play an increasingly important role in understanding complex phenomena, such as electrode microstructure, within batteries that are not easily captured by established methods.

This chapter focuses exclusively on these less-established or emerging methods within the context of battery research. By narrowing the scope, the aim is to highlight the potential of these techniques, provide new perspectives and enhance the understanding of battery systems. The discussion will intentionally omit the more well-established methods, not because they lack relevance, but to allow for a more detailed review of these innovative approaches that may otherwise receive less attention.

3.1 Contact Angle Measurements

Regarding the necessity for the measurement of contact angles as mentioned in the previous chapter and the requirements and limitations of the sample material's form, the need for several different methods arises.

3.1.1 Sessile Drop

The most accurate method to determine the interaction energy between a solid and a liquid, remains at present the contact angle measurement via sessile drop also known as drop shape analysis (DSA), first described by Thomas Young in 1805. [63,65] The method is based on image analysis for the determination of the contact angle between a sessile drop and a solid surface. It can further be used for the deduction of the surface tension of a pendant drop. A defined volume of a reference liquid with known γ_L^D and γ_L^P is dosed onto a solid surface resulting in the formation of a sessile drop, as depicted in Figure 11.
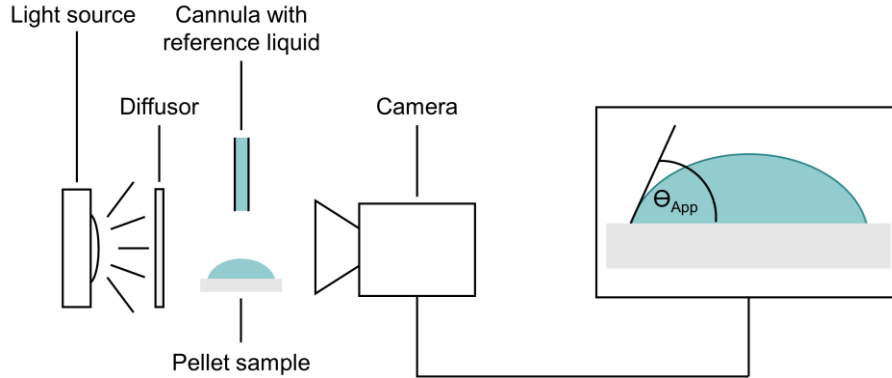
Figure 11 - Schematic of a measurement according to the sessile drop method adapted from Weber and Keim et al. [64]

Using a camera, a photograph of the droplet is captured and transmitted to a DSA software. Initially, the software conducts a contour recognition by analyzing the grayscale of the image. Next, the droplet contour is fitted with a geometric model to describe its shape. With a multitude of geometric models available for droplet description, the model employed in this work is the one according to Bashforth and Adams. [93] As noted in chapter 2.3, the apparent contact angle θ_{App} may differ from the contact angle defined by Young's equation (θ_{Young}). Decker et al. [94] proposed a solution involving small vibrations to surpass the metastable energy minima. Without access to this technique, a single measurement of the contact angle using the sessile drop method might yield inconsistent values due to contact angle hysteresis. Consequently, it is essential to perform multiple reproducible measurements to ensure that θ_{App} can be reliably used as a key parameter. The thereby determined contact angles of a set of reference liquids with the solid sample surface can then be inserted into Equation 12 allowing for the calculation of the sample's SFE.

3.1.2 Washburn Method

The flow of a rising liquid through a packaged powder or fibers is conceptualized by the Washburn method as a series of minuscule, parallel capillaries. [95] By utilization of the Hagen-Poiseuille equation the flow rate inside cylindrical capillaries can be calculated:

$$h^2(t) = \frac{r\gamma_L \cos(\theta_{adv})}{2\eta} \cdot t \tag{26}$$

with h being the travelled height of the liquid front, r the inner radius of the capillary, γ_L the surface free energy of the probing liquid, θ_{adv} the advancing contact angle, t the time of flow and η the viscosity of the reference liquid. The weight-based approach using a force tensiometer is preferred over the direct measurement of the height of the liquid front h as a precise measurement is rather difficult to achieve. The arrangement of placing the sample powder/fibers in a test capillary however, allows for a straightforward relationship between the liquid height h and the mass gain resulting from the absorbed liquid. If a cylindrical column is formed by the liquid with a given density ρ, having a radius of R and a height of h, and a sample porosity of ϕ, the resulting mass gain m can be expressed as follows:

$$m = \rho \cdot \phi \cdot V = \rho \cdot \phi \cdot \pi R^2 h \tag{27}$$

which results in

$$m^2(t) = r\phi^2(\pi R^2)^2 \cdot \frac{\rho^2 \gamma_L \cos \theta_{a\,dv}}{2\eta} \cdot t \tag{28}$$

also known as the modified Washburn equation, where $r\phi^2(\pi R^2)^2$ can be summarized as the capillary constant C. [95] To determine the capillary constant a referencing measurement with a fully wetting liquid ($\theta_{adv} = 0°$) is required, which is usually approximated for n-hexane. [96–98] Whilst C is heavily influenced by the particle dimensions of the sample powder and its packing density, the reproducibility of sample preparation is of utmost importance. [99] In the case of locally uneven packing, with some areas being packed tighter than others, gap formation between particles will occur upon first contact with the ascending probing liquid. This results in a strongly asymmetrical liquid front rising through the capillary, making the measurement of the length of travel inaccurate. [97,98]
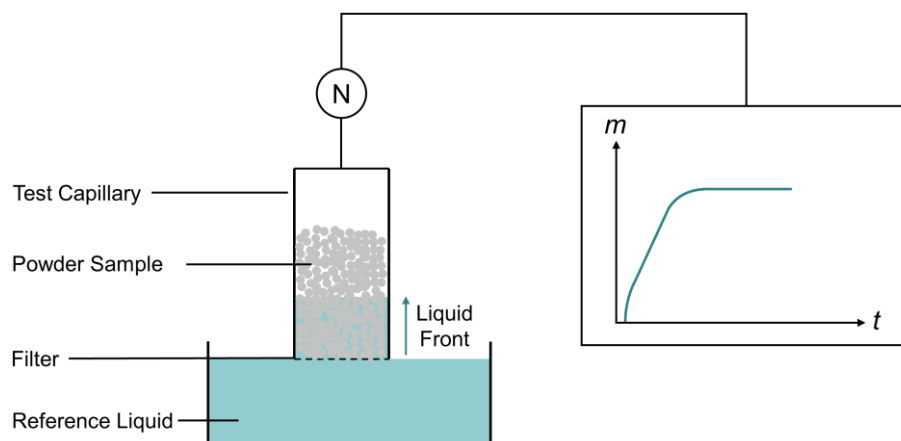
Figure 12 - Schematic of a measurement according to the Washburn method adapted from Weber and Keim et al. [64]

As illustrated in Figure 12 the measurement of the contact angle is conducted by loading a precisely measured quantity of sample material into a test capillary covered by a permeable filter on the bottom. To achieve comparable results the tap density is set to the same level for each measurement by tapping the bottom of the test tube. After mounting the capillary to a tensiometer, the powder is contacted by the probe liquid from below, simultaneously determining the weight gain of the sample. [97] With the analysis of several different test liquids, the surface free energy of the sample can be computed according to chapter 2.3 by solving Equation 12.

3.1.3 Pendant Drop

When aiming at determining the overall SFE of liquids, the pendant drop method (see Figure 13), which is comprised of four consequtive steps, can be applied.
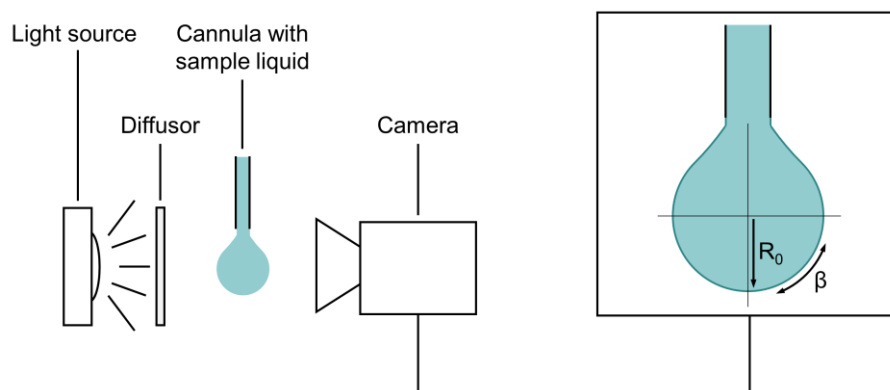
Figure 13 - Schematic of a measurement according to the pendant drop method adapted from Weber and Keim et al. [64]

In the first step the contour of a hanging drop is recorded, and turned into a greyscale image. In the following step, the size parameters R_0 and β are calculated from the profile of the drop. Several different models for the description of the drop profile have been established. The model utilized in this work, which is derived from the Young-Laplace equation is the model of Rotenberg et al. [100]. The overall surface tension of the liquid can then be calculated according to Equation (29:

$$\gamma = \frac{\Delta\rho g R_0^2}{\beta} \tag{29}$$

with the difference in mass density between the drop and the surrounding medium designated as $\Delta\rho$ and the gravitational constant as g. The radius of curvature at the drop apex is given as R_0 and β is the shape factor, derived from the shape of the drop, for which a value greater than 0.6 indicates a sufficient fit. To divide the overall SFE of the sample liquid into the dispersive and polar components a contact angle measurement with a purely dispersive surface, e.g. PTFE, according to the sessile drop method is required. Lastly, from the contact angle measurement both components can be determined by combining Equations 6 and 8. [100,101]

To give an overview of the elaborate process presented in chapter 2.3 and this chapter, Figure 14 visualizes the interconnection of the different theories, how they build on contact angle measurements in dependency of the sample under investigation and the key figures which can be obtained by their application.
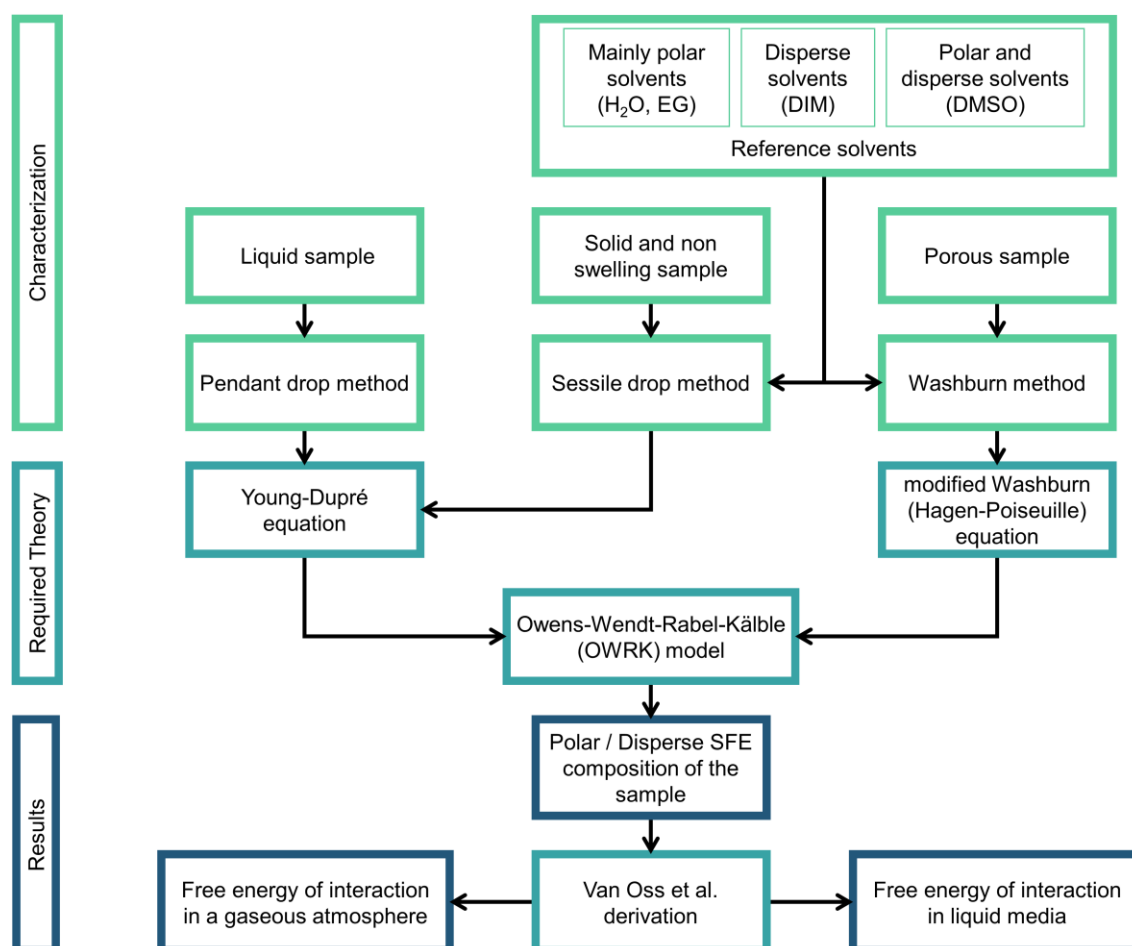
Figure 14 - Flowchart showing the step by step procedure of how to measure and interpret surface free energy starting with contact angle measurements to the free energy of interaction with its underlying theory

3.2   Karl-Fischer Titration

The Karl-Fischer titration, first described in 1935, is a chemical method for the determination of the water content in various substances. [102] While historically the procedure was based on the volumetric Karl-Fischer method, modern setups determine the water content in the sample coloumetrically utilizing the Eugen-Scholz method. The coulometric Karl-Fischer reagent is composed of sulfur dioxide, an organic base, and iodide in alcohol, preferably methanol. The required iodine is created in situ in a special coulometry cell. There it is oxidized to iodine at a platinum mesh electrode which in turn reacts with water according to the following equations: [103]

$$SO_2 + MeOH + B \rightleftharpoons MeSO_3^- + HB^+ \tag{30}$$

$$MeSO_3^- + H_2O + I_2 + 2B \rightarrow MeSO_4^- + 2HB^+ + 2I^- \tag{31}$$
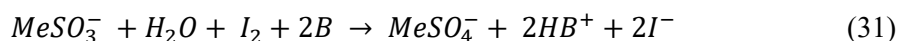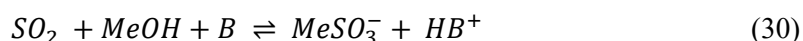
Instead of measuring the volume of the reagent, the current needed for the generation of the iodine is determined in the coulometric method. It is consequently used to calculate the molar mass of iodine generated according to Farraday's law of electrolysis which in turn allows for the calculation of the amount of water. Due to the emission of electrons during the oxidation of iodide, a corresponding cathode reaction is required. In certain setups this is carried out using a separate reagent generating hydrogen. The anode and cathode reactions can be expressed as: [103]

Anode:

$$2I^- \rightleftharpoons I_2 + 2e^- \tag{32}$$

Cathode:

$$2H^+ + 2e^- \rightarrow H_2 \uparrow \tag{33}$$

Modern setups, as visualized in Figure 15, are composed of a preceding molecular sieve which dries the carrier gas. The sample is heated inside a predried vial to evaporate the residual water. The dried carrier gas then transfers the residual water into the titration setup. Using a polarized detector electrode either a potential drop or a current increase is measured indicating an excess of iodine which marks the end of the titration.
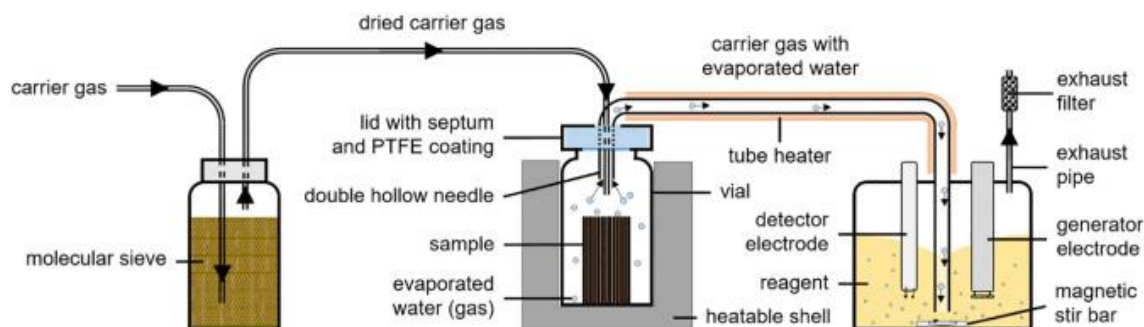
Figure 15 - Schematic of an indirect coulometric Karl-Fischer-Titration reproduced from Kosfeld et al. [104]

The indirect coulometric Karl-Fischer titration offers several advantages. Due to the measurement being indirect, meaning the sample does not come into direct contact with the reagent, the risk of side reactions and contamination inside the titration vessel is greatly reduced. [104] While the sensitivity of the volumetric method ranges between 10-50 mg, the coulometric Karl-Fischer titration lies between 500-1000 µg. [103] The coulometric method is, therefore, far more sensitive than the volumetric method making it ideal for investigations of materials with very low water contents, such as LIB electrodes. [104]

3.3   Corona Discharge

Typical corona discharge setups consist of a high frequency generator for frequency ranges between 10-40 kHz, an electrode with a high electrical potential of 10-40 kV, and a counter electrode at ground potential. The counter electrode usually comes in the form of a roller carrying the material which is to be treated. The roller is coated with a dielectric coating. This leads to a mostly uniform distribution of microdischarges on the surface of the substrate. As the discharges preferably occur on microscopic elevations the treatment does not lead to a homogeneously treated surface. However, it can be largely adjusted through the process parameters to optimize the wetting characteristics of the substrate surface. The electrodes are arranged in parallel to the substrate with distances of 2-3 mm between the high potential electrode and the substrate. In relation to the described setup, corona discharge is also often referred to as barrier discharge, since the discharge path is limited by the dielectric coating of the grounded (roller) electrode. [105]

At frequencies between 10-40 kHz and an alternating voltage of approx. 10-20 kV, the corona discharge occurs as a characteristically glowing high-voltage discharge. Ambient air most commonly serves as corona atmosphere with regard to conventional technical applications. The electrons emitted by the electrode are highly accelerated in the electric field and consequently collide with oxygen and nitrogen molecules in the surrounding atmosphere. During the collisions the electrons partly transfer their energy to the molecules, which in turn become dissociated or ionized. While the conversion of oxygen into reactive forms readily takes place, the conversion of nitrogen in the air into a reactive form only occurs to a very small extent due to the high bond energy (950 kJ/mol) of the nitrogen molecule. If the incorporation of nitrogen atoms into the substrate surface is desired, it can be more effectively achieved under a corona atmosphere containing nitrogen oxides. [105]

As the energy of the electrons colliding with the substrate exceeds the bond energy of various molecular bonds, e.g. C-C (3.8 eV) or H-C (4.5 eV), the molecular bonds are broken and result in free valences. The gaseous reaction products of the corona discharge can then interact with the free valences. In the presence of atomic oxygen and ozone mostly oxidation reactions occur leading to the formation of polar groups on the surface of the substrate, which in turn affect the wettability of the substrate. [106,107] Besides, the chemical alteration of the surface the collision of the electrons also affects the surface structure, creating micro-pits and indentations.

The energy introduced during the treatment is referred to as Watt density E and is given by:

$$E = \frac{W}{b \cdot v \cdot N} \qquad (34)$$

W designates the total power output of the electrode, b the width of the corona electrode, v the web speed of the treated sample and N the number of simultaneously treated sides.

4   Experimental

Electrode Manufacturing

The various electrode slurries were prepared by disc agitation (Dispermat CA60, VMA Getzmann, Germany) of LNMO, the conductive additive, the binder and deionized water. The solid content of the slurries was set to 60 wt%. The slurries were coated onto an 18 µm thick aluminum current collector (Batte-Foil-0004W, Pi-Kem, UK) by doctor blade on a roll-to-roll coating line (KTFS, Mathis AG, Switzerland). Web speed was set to 0.2 m/min. The electrodes were dried in-line in two consecutive convection ovens at 25 °C under circulating air. The pH values of all slurries were measured at 10.8 ± 0.1 irrespective of the slurry composition. While several publications report on the corrosion of the aluminum current collector due to the high pH of aqueous LNMO slurries [24,108], drying at low temperatures in the aforementioned way proved to be an effective way of coating the electrode without a detectable onset of corrosion. The electrodes were subsequently calendered at 50 °C (GKL200, Saueressig, Germany) to a porosity of approximately 30 %. The formulations of the different cathodes and the active material loadings are given in the respective chapters.

Anodes for full cell testing consist of 96 wt% graphite (SMG-A3, Hitachi, Japan), 1.5 wt% CB (C-NERGY Super C65, Imerys Graphite & Carbon, Switzerland), 1.25 wt% CMC (Walocel CRT 2000 PA, DuPont, USA), and 1.25 wt% styrene-butadiene rubber (SBR) (TRD 2001, JSR Micro, Belgium). Slurries were prepared by disc agitation (Dispermat CA60, VMA Getzmann, Germany) and coated onto copper foil with a thickness of 10 µm. The loading was set to 2.2 mAh/cm². By calendering at 50 °C (GKL200, Saueressig, Germany) the porosity was set to 48 %.

Cell Assembly

Cells were built from electrodes calendered at 50 °C. Coin cells in full cell setup were built inside an argon filled glove box (200B, M.Braun Inertgas-Systeme GmbH, Germany) with both electrodes having a diameter of 12 mm, a glass fiber separator (Whatman GF/C, Sigma-Aldrich, USA) and 200 µL of LP30 (1:1 EC:DMC, 1 M $LiPF_6$, Sigma-Aldrich, USA) containing 1 wt% of lithium bis(oxalato)borate (LiBOB, Sigma-Aldrich, USA) and tris(trimethylsilyl) phosphite (TMSP, Sigma-Aldrich, USA) each. Following the manual assembly, the cells were pressed by applying a nominal force of 5.2 MPa for 10 seconds. To check reproducibility, three coin cells with a negative to positive electrode capacity (N/P) ratio of approx. 1.1 were built and tested for each coating.

Cell Cycling and Rate Capability

The assembled cells rested for 48h prior to the electrochemical testing to assure full wetting of all components inside the cells by the electrolyte. Rate capability and long-term cycling tests were performed at 25 °C within a voltage interval of 3.5 V - 4.9 V vs Li/Li^+, assuming 147 mAh/g as specific capacity of LNMO.

Starting with the initial formation of the cells, three cycles at 0.1 C (charge/discharge) were performed. Rate capability was then tested according to the following charge/discharge pattern: 0.5 C/0.5 C; 0.5 C/1 C; 0.5 C/2 C; 0.5 C/5 C; 0.5 C/10 C, 0.5C/1C for 5 cycles each. Charging of the cells consisted of a constant current mode up to 4.9 V and a subsequent constant voltage step with 0.05 C as cut-off limit (constant current – constant voltage (CCCV)).

Formation of the cells for long-term cycling was carried-out as mentioned above. The cells were then cycled for 1000 cycles at 0.5 C/1 C (charge/discharge). Every 50th cycle a C-rate of 0.1 C/0.1 C was applied. CCCV charging as described above was also used in long-term cycling.

Surface Free Energy

With regard to solid samples, either the Washburn (WB) or the sessile drop (SD) method was applied, as discussed in chapter 3.1. Each individual cathode component was tested depending on the feasibility of preparing a sample with a dense surface without changing its surface chemistry. Liquid samples were tested according to the pendant drop method (PD). The SD and PD drop methods were performed on a drop shape analyzer (DSA30, Kruess Scientific, Germany). Contact angle measurements on porous samples were conducted according to the WB method on a force tensiometer (K100, Kruess Scientific, Germany). The preceding reference measurement of the sample's capillary constant as required by the WB method was performed using n-hexane as fully wetting liquid. The physicochemical properties of the applied reference liquids, most commonly referenced in literature, are given in Table 1. Each measurement was repeated three times.

Table 1 - Physicochemical properties of reference liquids at 20 °C [109]

Reference liquid	ρ (g/mL)	η (mPa·s)	γ_{LV}	γ_{LV}^d	γ_{LV}^p
			(mJ/m²)		
n-Hexane	0.661	0.326	18.4	18.4	0.0
Water	0.998	1.000	72.8	21.8	51.0
Diiodomethane (DIM)	3.325	2.762	50.8	50.8	0.0
Dimethyl sulfoxide (DMSO)	1.100	1.996	44.0	36.0	8.0
Ethylene glycol (EG)	1.109	21.81	48.0	29.0	19.0

Adhesion Strength Testing

The adhesion strength of the electrodes was measured in a 90° peel test using a zwickiLine Z2.5/TN (ZwickRoell, Germany). Electrode stripes with dimensions of 60 mm x 17 mm were fixed to double-sided adhesive tape with the coating facing downwards to a metallic holder and pressed with a nominal load of 0.3 MPa for 10 s. Afterwards, the aluminum foil was peeled off from the electrode layer at a 90° angle at a constant speed of 600 mm/min. The adhesion strength in N/m was determined in accordance with ISO 813:2019 through a 10 N load cell and evaluated as the mean value of the force on a peel length of 40 mm – dismissing the data gathered on the

first and last 10 mm of the test – and divided by the width of the sample. [110] Details regarding the treatment of the samples prior to measuring are given in the individual chapters.

SEM and EDS analysis

SEM micrographs were taken on a Gemini (Carl Zeiss, Germany) at an acceleration voltage of 2 kV. EDS was conducted on an Ultim Extreme Detector (Oxford Instruments, UK). The acceleration voltage was set to 4 kV. Cross sections were prepared by ion milling on a TIC3X (Leica Microsystems, Germany).

Resistivity Measurements

Both interface resistance and bulk resistivity were simultaneously measured on a Hioki RM2610 (Hioki E.E. Corp., Japan) based on the finite volume method (FVM). Measurements were repeated five times for each cathode. Measuring points were chosen at random.

Tortuosity by EIS

Tortuosity was measured in a symmetrical cell configuration. Three coin cells were built for each coating that had undergone calendering at 50 °C and annealing at 175°C for 40 minutes consisting of two cathodes with a diameter of 16 mm, a trilayer PP/PE/PP separator (H2013, Celgard, USA) and an electrolyte with non-intercalating conditions, namely EC:DMC (1:1 vol:vol) with 0.01 M tetrabutylammonium perchlorate (TBAClO$_4$, Sigma Aldrich, >99.0 %).

Potentiostatic impedance spectra were obtained over a frequency range of 100 kHz to 20 mHz. The measurement was repeated 50 times with an OCV step of one hour between individual measurements. The equivalent circuit model, according to Landesfeind et al. [111], applied for fitting the data is illustrated in Figure A 3.

Karl-Fischer Titration

Electrode sheets were prepared as if used in a cell. They were calendered to a porosity of 30 % and dried for 4 h at 110 °C under vacuum or 24 h at 110 °C under vacuum and an additional 24 h under vacuum at room temperature. The electrodes were cut into approximately 60 mm x 17 mm samples and put into vials which were predried for 16 h at 120 °C under vacuum. To evaporate the residual water in the sample, the sample chamber was heated to a temperature of 160 °C for 12 minutes. The carrier gas was also dried using a molecular sieve. The setup was located in a dry room with a dew point of -60 °C.

Corona Treatment

The corona treatment of the current collector was performed in-line on a roll-to-roll coating line (KTFS, Mathis AG, Switzerland). The differences in treatment intensity are given in the respective chapter.

5 Submersion of LiNi$_{0.5}$Mn$_{1.5}$O$_4$ in Water

LNMO has been investigated as a cathode active material for more than 20 years. Despite the extensive amount of research conducted on the topic, the transfer of LNMO's promising properties into stable battery cells is still problematic. [112] Especially the aqueous processing of LNMO poses a variety of challenges that still have to be overcome in order for it to be applied at an industrial scale. Among the most prominent challenges are the high pH value of the water-based slurries leading to corrosion of the current collector, the dissolution of manganese and the associated degradation of graphite anodes, and the low mechanical integrity of the cathodes, consequently resulting in degradation due to delamination. Regarding the high pH values of aqueous slurries, the benefits of using various acids as additives in aqueous processing of LNMO are well reported in literature. Kuenzel et al. [24] demonstrated the beneficial effects of citric and phosphoric acid as slurry additives as both can be used to neutralize the high pH above 11 of aqueous LNMO slurries resulting from the formation of LiOH, effectively mitigating the corrosion of the aluminum current collector which is reported to be stable in the range of 4 to 8.5. [113] Stokes-Rodriguez et al. [114] further showed that by applying polyacrylic acid (PAA) it serves as both a binding and buffering agent, allowing for pH control without the need for additional processing additives. With respect to the adhesion strength of aqueously processed LNMO cathodes, Bauer et al. [115] demonstrated that the usage of acid additives can, due to the small molecule size of most acids, also result in the deterioration of the adhesive bonds between current collector and cathode coating. However, Yao et al. [16] showed that mechanical integrity is one of the key factors of successful long-term cycling of LNMO cathodes, especially when aiming at industrially relevant high areal mass loadings. Nevertheless, Kuenzel et al. [24] reported on the benefits of citric acid as cross-linking agent in combination with CMC to improve the mechanical integrity of aqueously processed cathodes and consequently the long-term capacity retention. In addition, Pieczonka et al. [116] demonstrated that the application of high molecular weight LiPAA results in higher adhesion strengths compared to NMP-processed PVDF electrodes due to improved interaction between the polar moieties of LiPAA with LNMO as well as the conductive additive. They further addressed the dissolution of manganese from the active material, arguing that LiPAA results in the formation of an artificial CEI, significantly suppressing the detrimental side reactions of the LNMO which was also confirmed by the independent work of He et al. [23] In fact, several other authors have addressed this issue in their works and proposed a variety of solutions such as passivation layers on the LNMO [24,116–118], different electrolyte additives [119–122] or doping of the active material [123,124]. As the conditions and the extent of the results in all of the aforementioned publications greatly differ – from particle size, specific surface area, morphology and type of synthesis of the LNMO to the processing parameters – the following chapter serves to establish a baseline for the investigations conducted throughout this work.

5.1   Experimental

Materials

Table 2 - Materials - water submersion

Reference	Name	Manufacturer
LNMO	TBM-129	Haldor Topsoe, Denmark
C65	C-NERGY Super C65	Imerys Graphite & Carbon, Switzerland
PVDF	Solef 5130	Solvay, France
NMP	Supelco	Sigma-Aldrich, USA

The active material samples LNMO$_{H2O}$ and LNMO$_{H2O+H3PO4}$ were prepared by disc agitating (Dispermat CA60, VMA Getzmann, Germany) 50 g of LNMO in 32.75 g of deionized water (Millipore, Merck, Germany) or 32.75 g of deionized water (Millipore, Merck, Germany) plus 0.375 g of a H$_3$PO$_4$ solution with an 85 wt% concentration (Sigma-Aldrich, USA) for 1 h at 1000 rpm, respectively. The phosphoric acid in the solution amounts to 0.75 wt% of the LNMO. The powders were recovered by a) evaporating the water or b) by vacuum filtration. In the case of a) the dispersion was placed inside a petri dish with a diameter of 150 mm and placed inside an oven filled with ambient air at 50 °C for 2 h. Regarding the time it takes the water to evaporate, the actual submersion time of the LNMO is estimated to be somewhere around 2.5 h. The vacuum filtration b) was carried out at room temperature using a glass fiber filter with a pore size of 1.8 µm. The filtrate was kept for further analysis and again filtered through a syringe filter with a pore size of 1.0 µm. Whether the characterizations were performed using dried or vacuum filtered LNMO will be specified for each characterization.

Electrode Manufacturing

Table 3 - Cathode properties - water submersion

Reference	LNMO	PVDF	C65	Areal capacity
	(wt%)			(mAh/cm²)
LNMO$_{pristine}$	92.6	4.6	2.8	1.80
LNMO$_{H2O}$	92.6	4.6	2.8	1.79
LNMO$_{H2O+H3PO4}$	92.6	4.6	2.8	1.84

Differing from the manufacturing as described in chapter 4, the slurries were prepared using NMP as solvent and dried in-line in two consecutive convection ovens at 40 °C and 80 °C.

Cell Assembly

Foregoing the assembly of the cells, as described in chapter 4, the electrodes were dried at 110 °C for 4 h in a vacuum oven to evaporate residual water. Deviating from the description in chapter 4, rate capability tests were performed on half cells using 250 µm thick lithium metal disks as anodes.

5.2 Results and Discussion

SEM and EDS analysis

The results of the EDS analysis, performed on the pristine powder revealed the presence of a layer, consisting of O, Na, S and K on the surface of the LNMO (Figure 16 (A)). With regard to the submerged samples p$_{H2O}$ and p$_{H2O+H3PO4}$, recovered after water evaporation, it can be observed that the uniform layer vanishes, hinting at a good solubility in water. However, it appears that the residues that have dissolved off the LNMO are locally precipitating as the concentration in the spandrels between active material particles rises upon evaporation of the water. The large precipitations, seen in Figure 16 (B) and (C), indeed consist of the aforementioned concentrated residues. The distortion (white lines) in the SEM image of p$_{H2O+H3PO4}$ results from the charge-up of the sample. As this effect is only visible on the samples containing the concentrated impurity it hints at low conductivity of the impurity. Moreover, the formation of phosphates ranging from small (<200 nm) to very large (~8 µm) crystals was evidenced on sample p$_{H2O+H3PO4}$ treated with 0.75 wt% phosphoric acid. The absence of Ni and Mn in the phosphate compounds can also be observed through EDS (Figure A 1). It is therefore argued that mainly Li$_3$PO$_4$ is formed upon submersion in phosphoric acid.
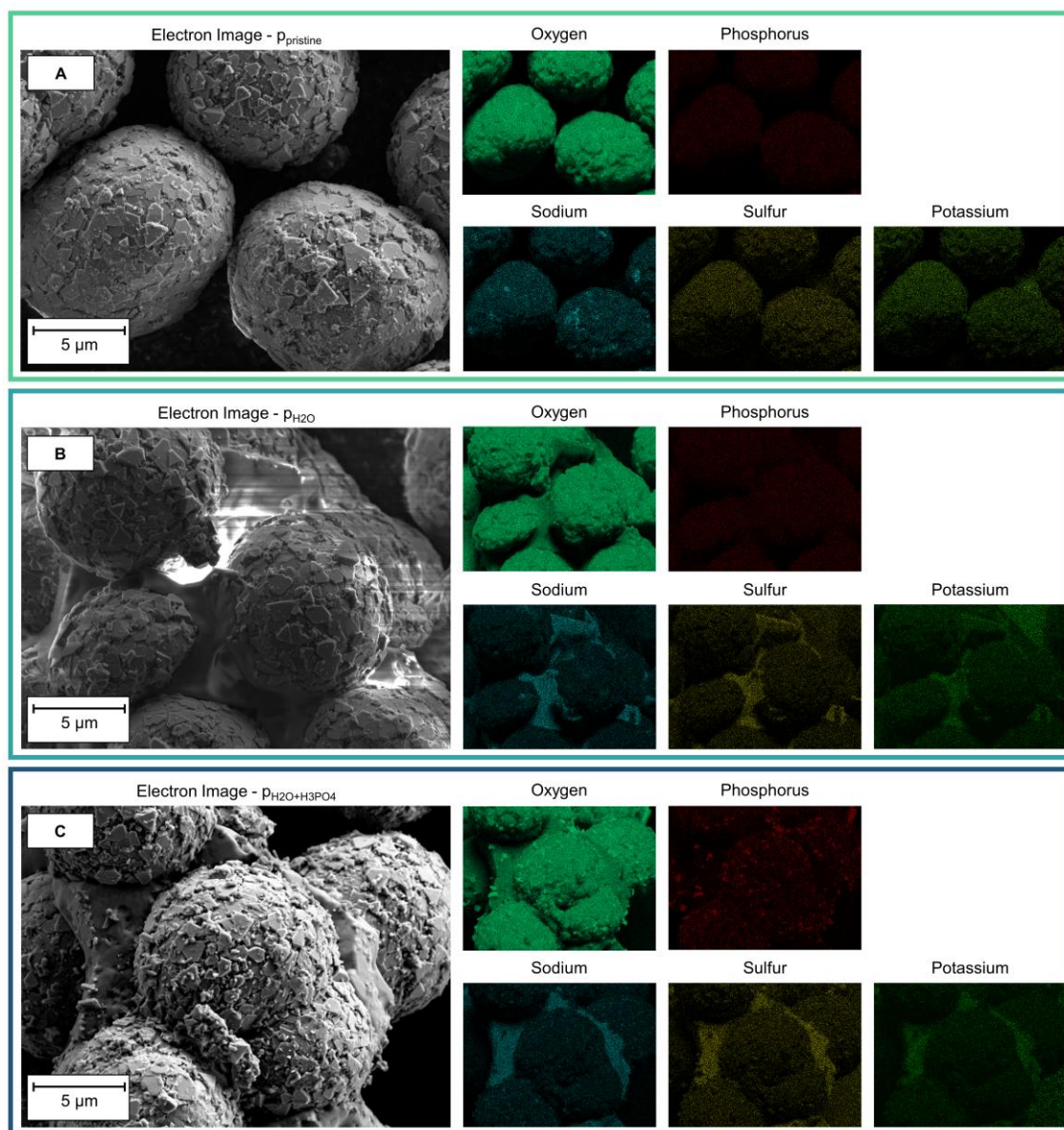
Figure 16 - EDS analysis of (A) pristine LNMO, (B) LNMO submerged in H$_2$O for 1h and air-dried, (C) LNMO submerged in H$_2$O + H$_3$PO$_4$ for 1h and air-dried

ICP-OES

To identify the impurities, which were found to be water-soluble, ICP-OES was also performed on the concentrated impurity after evaporating the water recovered from vacuum filtration of p$_{H2O}$. ICP-OES measurements further confirmed the impurities found via EDS analysis, namely O, Na, S and K. The results of the elemental analysis are compiled in Table 4.

Table 4 - Composition of isolated surface impurity of LNMO obtained by vacuum filtration as determined by ICP-OES ± standard deviation

Element	Detection Limit	Impurity	
	(wt%)		(mol)
O	3.4	40.0 ± 2.4	2.5 ± 0.15
Na	0.3	9.0 ± 0.3	0.39 ± 0.01
S	0.4	18.3 ± 1.0	0.57 ± 0.03
K	0.1	30.4 ± 1.1	0.78 ± 0.03
Sum		97.7	

Under consideration of the standard deviations a possible stoichiometry of the residue might be K$_4$Na$_2$(SO$_4$)$_3$. [125] In fact, with regard to the charge-up of the SEM sample, the low electrical and ionic conductivity of sodium containing sulfates is well described in literature. [126,127] Furthermore, transition metal sulfates as well as potassium and sodium in the form of hydroxides are known educts often used in the synthesis of lithium metal oxides [128–131]. It is therefore concluded that the analyzed surface impurity stems from the synthesis process and remains on the surface of the LNMO as a residue.

Additionally, ICP-OES was performed on the filtrate recovered after 1 h of submersion to quantify the amounts of ions leaching into solution over the course of slurry preparation. The results are compiled in Table 5. The pH values of the filtrates are 10.93 and 5.86 for p$_{H2O}$ and p$_{H2O+H3PO4}$, respectively. The LNMO submerged in solely deionized water exhibits only a very low concentration of lithium-ions and negligible concentrations of Mn and Ni. With the addition of 0.75 wt% H$_3$PO$_4$ lithium dissolution increases eightfold. However, regarding the transition metal ions the dissolution is drastically exacerbated in the presence of acidic species with concentrations rising by three orders of magnitude.

Table 5 - Ion leaching due to submersion as determined by ICP-OES ± standard deviation performed on the filtrate recovered from the preparation of LNMO$_{H2O}$ and LNMO$_{H2O+H3PO4}$

Element	Detection Limit	LNMO$_{H2O}$	LNMO$_{H2O+H3PO4}$
		(ppm)	
Li	0.6	55.3 ± 1.5	461 ± 13
Mn	0.0009	0.0568 ± 0.0012	207 ± 5
Ni	0.0048	0.0267 ± 0.0004	140 ± 2
Sum		55.386	808

Later investigations in chapters 6.1 and 6.2 use PVDF in the form of latex, i.e. the PVDF is synthesized by emulsion polymerization and the resulting primary particles are stabilized in an aqueous solution. When applying phosphoric acid, the concentration of ions within the slurry, especially the transition metal ions, carrying multiple charges was found to have a significant impact on the stabilization of the PVDF latices. As depicted in Figure 17, the average primary particle size of the PVDF latex significantly increases from 145 nm to 7.48 μm when exceeding the critical coagulation concentration of the latex. The slurry then becomes unprocessable due to the large coagulated particles within the slurry, which leads to strong grooves in the coating when applied by a doctor blade.
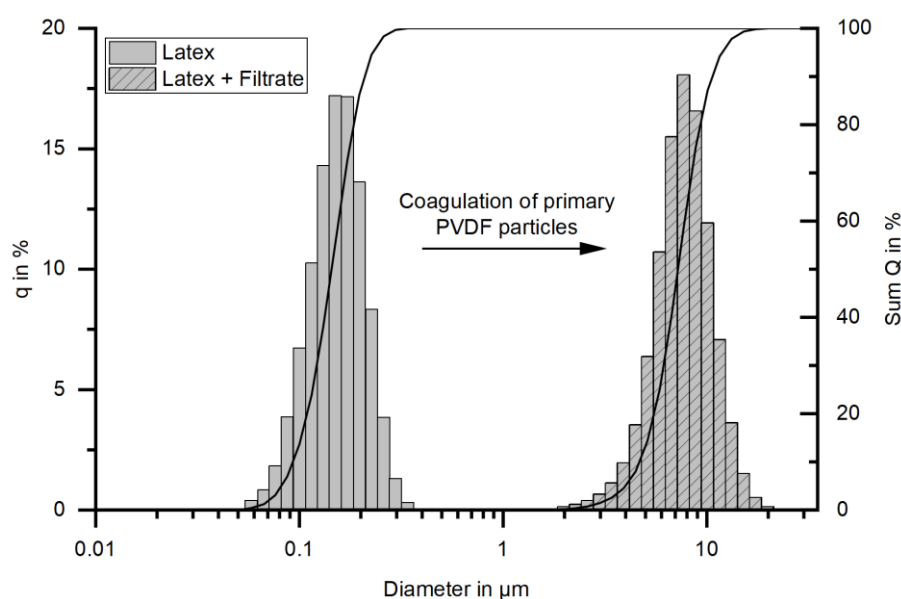
Figure 17 - Representative particle size analysis of PVDF latex spiked with acidified filtrate recovered from the preparation of p$_{H3PO4}$

Electrochemical Characterization

Rate capability tests on coin cells in half cell configuration, illustrated in Figure 18, from 0.5 C up to 10 C show a superior rate performance of cathode LNMO$_{H2O}$. While LNMO$_{H2O}$ already outperforms cathodes LNMO$_{pristine}$ and LNMO$_{H2O+H3PO4}$ and at low C-rates up to 1 C, the difference in rate capability becomes even more evident at C-rates above 2 C. While LNMO$_{H2O+H3PO4}$ yields slightly lower discharge capacities as LNMO$_{pristine}$ up to 2 C, a shift can be observed starting at 5 C. Succeeding the rate test the cells were cycled for 70 cycles at 0.5 C / 1 C (charge/discharge). LNMO$_{H2O+H3PO4}$ exhibits a significantly lesser degree of degradation than both LNMO$_{pristine}$ and LNMO$_{H2O}$.

Long-term cycling experiments of coin cells in full cell configuration show the same ranking in terms of initial capacity with LNMO$_{H2O}$ exhibiting an increased discharge capacity of approx. 5 % compared to both LNMO$_{pristine}$ and LNMO$_{H2O+H3PO4}$ at the first cycle after formation as well as after 1000 cycles. Analogue to the rate capability tests the degradation of LNMO$_{H2O+H3PO4}$ within the first 130 cycles is slightly less pronounced than in cathodes LNMO$_{pristine}$ and LNMO$_{H2O}$. As evidenced through EDS analysis, upon treatment of the LNMO with water acidified by 0.75 wt% H$_3$PO$_4$, phosphate species form on the surface of the active material. Stüble et al. [124]

demonstrated that the addition of 1 wt% Li$_3$PO$_4$ to LNMO cathodes significantly reduces the degradation of graphite full cells by acting as a proton scavenger and consequently suppressing the reaction between LiPF$_6$ and H$^+$ which results in the formation of HF. They further suggested the direct immobilization of transition metal ions by Li$_3$PO$_4$ or its anions leading to less crossover of dissolved transition metal ions to the anode where Mn^{2+} is known to trigger the continuous growth of the SEI under consumption of Li$^+$.[132] However, the amount of phosphate species formed from 0.75 wt% H$_3$PO$_4$ in the submersion fluid is argued to be insufficient to effectively suppress degradation over the course of 1000 cycles.
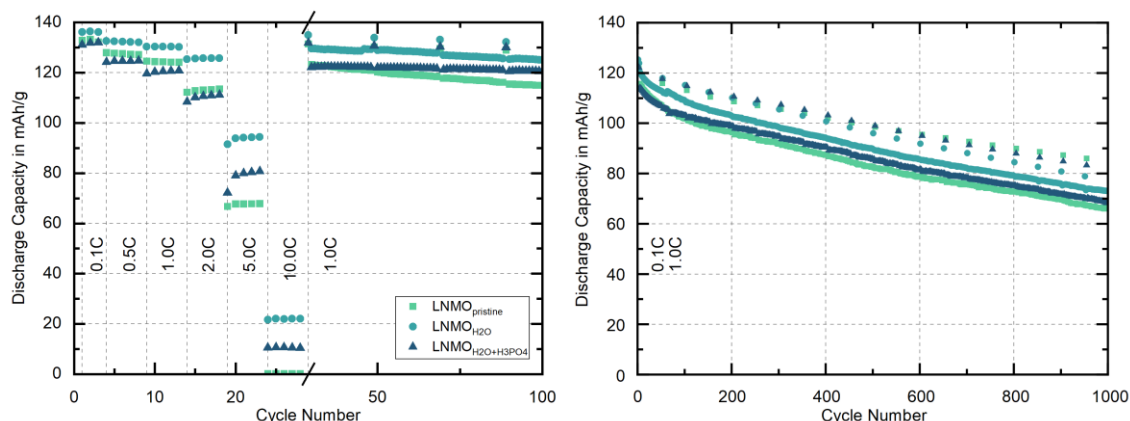
Figure 18 - Rate capability in half cell configuration (left) and long-term full cell cycling performance (right) of cathodes manufactured with NMP from differently pre-treated LNMO powders

Differential capacity curves of the cells are illustrated in Figure 19. The dQ/dV plot of cycle 2 which is the second formation cycle at a charge/discharge rate of 0.1 C shows identical polarization of the different cathodes. However, when cycling at higher C-rates, e.g. in cycle 250 with an asymmetrical charge/discharge rate of 0.5 C/1.0 C, differences in polarization between the cathodes can be observed. LNMO$_{H2O}$ and LNMO$_{H2O+H3PO4}$ both show polarization to a similar extent, with LNMO$_{H2O+H3PO4}$ having lower peak intensities, while LNMO$_{pristine}$ exhibits higher polarization during both charging and discharging. In later cycles, namely cycles 500, 750 and 1000 the overall polarization of all cathodes increases. Yet, the differences between the cathodes remain rather constant during the charging step at 0.5 C. Focusing on the discharge steps at 1.0 C, the dissimilarities between the submerged LNMO samples and the pristine LNMO become more pronounced, with LNMO$_{pristine}$ experiencing stronger polarization which is due to LNMO$_{pristine}$ being covered in the resistive sulfate residue as evidenced in Figure 16. [133] As the polarization curves of LNMO$_{H2O}$ and LNMO$_{H2O+H3PO4}$ are almost identical and only vary in peak intensitiy it is argued that the differences in discharge capacity stem from the loss of active lithium due to the ion leaching during submersion in acidified water. [134,135] In fact, investigations on layered oxides as well as other spinel active materials by several authors, have shown that transition metal and lithium-ion dissolution due to the superficial attack of acidic species results in a reduction of electrode capacity. [136–138]
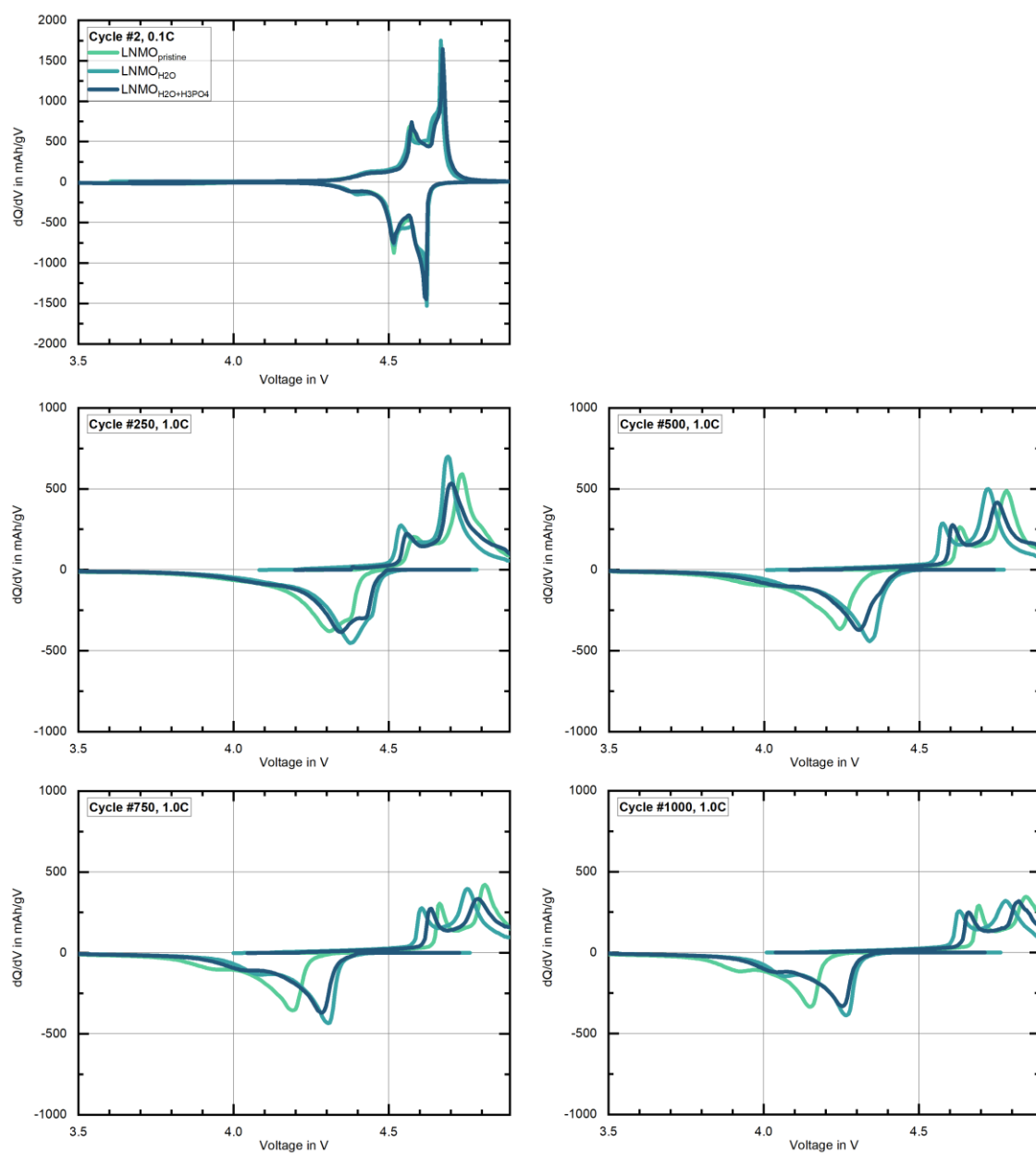
Figure 19 - Comparison of differential capacity curves of LNMO$_{pristine}$, LNMO$_{H2O}$ and LNMO$_{H2O+H3PO4}$ of cycles 2, 250, 500, 750 and 1000

5.3 Conclusion

To identify the impact of submersion on commercially available LNMO during aqueous processing, LNMO was submerged in water as well as water acidified by 0.75 wt% H$_3$PO$_4$ as the addition of phosphoric acid is frequently recommended in literature on water-based processing of several active materials including LNMO. Through ICP-OES measurements on the filtrates recovered from submersion, it was found that only small amounts of Li and negligible amounts of transition metals are leached into the submersion liquid when using only water. However, using acidified water results in a pronounced increase of lithium-ion and a drastic increase of Mn- and Ni-ion leaching. Concerning the application of PVDF latices in later investigations, the high concentration of multivalent ions in the solvent led to the rapid coagulation of the latices' primary particles, rendering the addition of H$_3$PO$_4$ impractical. Further, EDS analysis as well as ICP-OES measurements revealed the presence of a water-soluble surface impurity, consisting of K, Na, S, and O, which was found to dissolve during submersion and locally redeposits upon drying. With respect to the state-of-the-art synthesis process of cathode active materials, it is argued that the impurity stems from the educts and remains on the material as residue. Rate capability tests in half-cell configuration showed that LNMO after submersion in water, outperforms both pristine LNMO and LNMO submerged in acidified water at all investigated C-rates. Long-term capacity retention tests on full cells exhibited the same trend. To summarize, LNMO benefits from the removal of the resistive impurity coating upon submersion in water. While the formation of Li$_3$PO$_4$ during submersion in acidified water is advantageous for long-term capacity retention, the use of H$_3$PO$_4$ also entails the loss of active lithium and transition metal ions and is not applicable when working with PVDF latices.

6   Surface Free Energy in Aqueous Processing of LiNi$_{0.5}$Mn$_{1.5}$O$_4$ Cathodes

Throughout their cycle life electrodes are subjected to various mechanical stresses, such as cutting before the assembly, swelling before the formation, or large volume changes during cycling. It is one of the main tasks of the binder to ensure a sufficiently high mechanical integrity of the electrode to withstand these stresses and prevent delamination which ultimately leads to a rapid capacity fade. [139] There are several approaches to address low adhesion between the coating and the current collector as well as cohesion between the individual electrode constituents. Multiple authors have shown that by adjusting electrode formulations towards higher binder contents the adhesion strength of the coating can be raised significantly. Son et al. [140] demonstrated in their work on aqueously processed graphite anodes that raising the binder content from 2 wt% over 4 wt% to 8 wt% results in an increase in adhesion strength in approx. 45 % and 70 %, respectively. Meyer et al. [141] showed the same tendency in their work on high-loading NMC 111 cathodes applying PVDF as the binder. There, the adhesion strength of the coating increased by 89 % and 156 % by adjusting the binder content from 3 wt% to 4 wt% and 5 wt%, respectively. While raising binder content might be the simplest solution to adjust the mechanical integrity of electrodes, this comes at the expense of the electrode's energy density as part of the active material content is substituted by binder. Meyer et al. [141] further demonstrated that high CA and binder contents result in greater compaction resistance during calandering necessitating higher line loads and temperatures to achieve the required porosities. Moreover, Zhang et al. [142] showed that increasing the binder content can lead to lower specific discharge capacities as an excess of insulating polymer binder can lead to inferior electrical conductivity.

A different approach to optimize adhesion strength without altering the composition of electrodes towards higher binder contents is the investigation of the drying conditions, i.e. the influence of kinetics. Baunach et al. [143] investigated the adhesion strength of aqueously processed graphite anodes with respect to the drying temperature. They found that an increase of the drying temperature by 25 °C, which in turn means an increased drying rate, results in a decrease of the electrode's adhesion strength by 41 % due to pronounced migration of binder and CA away from the current collector towards the top of the electrode. Westphal et al. [144] further demonstrated that an increase in drying rate, irrespective of it being caused by higher temperature or air flow, results in the deterioration of the electrodes' adhesive properties. Klemens et al. [145] later showed that the findings on anodes are also viable for cathodes, showcasing NMC 111 as active material. Moreover, they all found the migrated binder to have a substantial influence on electrode resistivity, ultimately leading to inferior electrochemical performance. Thus, the drying rate of electrodes should be kept low. As this leads to reduced production efficiency and higher cost, industrial scale production has implemented a multi-temperature gradient drying process. [146]

While there is a large field of battery research dedicated to the investigation of the influence of kinetics on the interaction and behavior of slurry components, thermodynamic forces are generally neglected. The investigation of surface free energy has been well established in various other industrial applications such as lubrication [147], printing [148], painting [147], detergent formulation [149,150] or adhesive joining [151]. The methods associated with the determination of SFE are low in complexity and cost. However, in battery research, there are only a few works utilizing SFE in their investigations of electrode performance. Ludwig et al. demonstrated the significance of SFE in dry processing on the microstructure and the electrochemical performance of LCO and NMC 111 cathodes. By measuring the SFE of the electrode components, they were able to not only explain the differences in microstructure between dry-coated and slurry-cast electrodes but also utilize their findings to predict and optimize the carbon additive distribution. [87,88,152] Li et al [153] demonstrated under consideration of SFE of a poly(ethyleneimine) based LFP slurry and an aluminum current collector (CC) that the exact energy density of a corona treatment of the CC can be calculated to maximize the interaction or wetting of the slurry which resulted in improved rate capability and long-term capacity retention of the cathode. Yet, literature on application of the concept of SFE in solvent-based processing, is solely focused on the slurry and its processability while fully disregarding the interaction of the individual electrode components. The objective of the following chapter is to address this gap and investigate the influence of surface free energy on aqueous processing of LNMO and the resulting electrode properties.

6.1   Influence of the Conductive Additive

The findings of this chapter were also published in the Journal of the Electrochemical Society, Volume 171, Number 4 on April 16th, 2024 as "The Role of Surface Free Energy in Binder Distribution and Adhesion Strength of Aqueously Processed LiNi$_{0.5}$Mn$_{1.5}$O$_4$ Cathodes". The following chapter investigates how SFE and surface area of different conductive additives influence the properties and the electrochemical performance of aqueously processed LNMO cathodes. The chosen conductive additives cover a range of different SFE distributions from primarily dispersive to mainly polar contributions and range from low surface to high surface areas.

6.1.1 Experimental

Materials

Table 6 - Materials - influence of the conductive additive

Reference	Name	Manufacturer	BET (m²/g)
LNMO	TBM-129	Haldor Topsoe, Denmark	0.3
C65	C-NERGY Super C65	Imerys Graphite & Carbon, Switzerland	62.0
C45	C-NERGY Super C45	Imerys Graphite & Carbon, Switzerland	45.0
VGCF	VGCF-H	Resonac Corporation, Japan	12.0
CMC	Walocel CRT 2000 PA 07	DuPont, USA	-
PVDF Latex	Kynar, experimental	Arkema, France	-

Electrode Manufacturing

Table 7 - Cathode properties - influence of the conductive additive

Reference	LNMO	CMC	PVDF	CA	Type of CA	Areal capacity
	(wt%)					(mAh/cm²)
C65$_{0.0wt\%}$	95.2	1.9	2.9	0.0	-	2.0 ± 0.1
C65$_{1.4wt\%}$	93.9	1.9	2.8	1.4	C65	2.1 ± 0.1
C65$_{2.8wt\%}$	92.6	1.8	2.8	2.8	C65	2.0 ± 0.1
C65/VGCF$_{1.4+1.4wt\%}$	92.6	1.8	2.8	1.4 + 1.4	C65 + VGCF	1.9 ± 0.1
VGCF$_{2.8wt\%}$	92.6	1.8	2.8	2.8	VGCF	1.9 ± 0.1
C45$_{2.8wt\%}$	92.6	1.8	2.8	2.8	C45	2.0 ± 0.1
C65/VGCF$_{norm.}$	94.12	1.19	1.85	1.42 + 1.42	C65 + VGCF	2.0 ± 0.1
VGCF$_{norm.}$	95.68	0.56	0.87	2.89	VGCF	1.9 ± 0.1

Cell Assembly

Foregoing the assembly of the cells, as described in chapter 4, the electrodes were annealed at 175 °C for 40 minutes in a convection oven and later dried at 110 °C for 4 h in a vacuum oven to evaporate residual water.

Surface Free Energy

Achieving samples with closed surfaces able to hold liquid drops was not possible for the powder/fiber samples, namely LNMO and the conductive additives. They were consequently measured by the WB method. The polymer binders were also in powder form. However, they could not be measured by the WB method as they prevented the rise of the probing liquids by clogging the pores of the filter fixed to the bottom of the testing capillary. The PVDF latex was consequently pressed into a pellet with a diameter of 14 mm by applying a nominal load of 500 kPa after drying at 50 °C under vacuum. The CMC sample was prepared by coating an approximately 20 µm layer onto a glass substrate. The measurement of the aluminum foil was performed on a 14 mm circular punch-out. The contact angle of these samples was then determined by sessile drop.

Adhesion Strength Testing

Measurements were conducted before and after calendering at 50 °C (GKL200, Saueressig, Germany) and 175 °C (GK300L, Saueressig, Germany) as well as after annealing in a convection oven at 175 °C (T$_{melt\ PVDF}$ = 163 °C) for 10 and 40 minutes.

6.1.2 Results and Discussion

Mechanical Properties

As illustrated in Figure 20, the adhesion strength results for all coatings containing 2.8 wt% CA indicate poor mechanical integrity in their uncalendered state. Adhesion strength can be improved by approximately 100 % for most coatings through calendering at 50 °C with a roll speed of 1 m/min. However, both C65$_{2.8wt\%}$ and C45$_{2.8wt\%}$ show only a slight enhancement. The manufacturer specifies the PVDF melting temperature as 163 °C. Therefore, hot calendering at 175 °C with a roll speed of 1 m/min leads to a further increase of adhesion strength. Yet, annealing the coatings at 175 °C after the calendering step shows the most significant improvement in mechanical strength, reaching a plateau after 40 minutes, as can be seen in Figure A 2. The coatings containing C65 exhibit a smaller relative increase in adhesion strength compared to coatings C45$_{2.8wt\%}$, C65$_{0.0wt\%}$, and VGCF$_{2.8wt\%}$ after 10 minutes of heat treatment. However, extending the heat treatment to 40 minutes yields results similar to VGCF$_{2.8wt\%}$. For C65$_{2.8wt\%}$, heat treatment only has a negligible effect on adhesion strength, regardless of duration. The dashed red line represents a reference of a PVDF (Solef 5130, Solvay, France) cathode calendered to 30 % porosity with a 4.6 wt% binder content, manufactured using the conventional organic solvent (NMP) process.
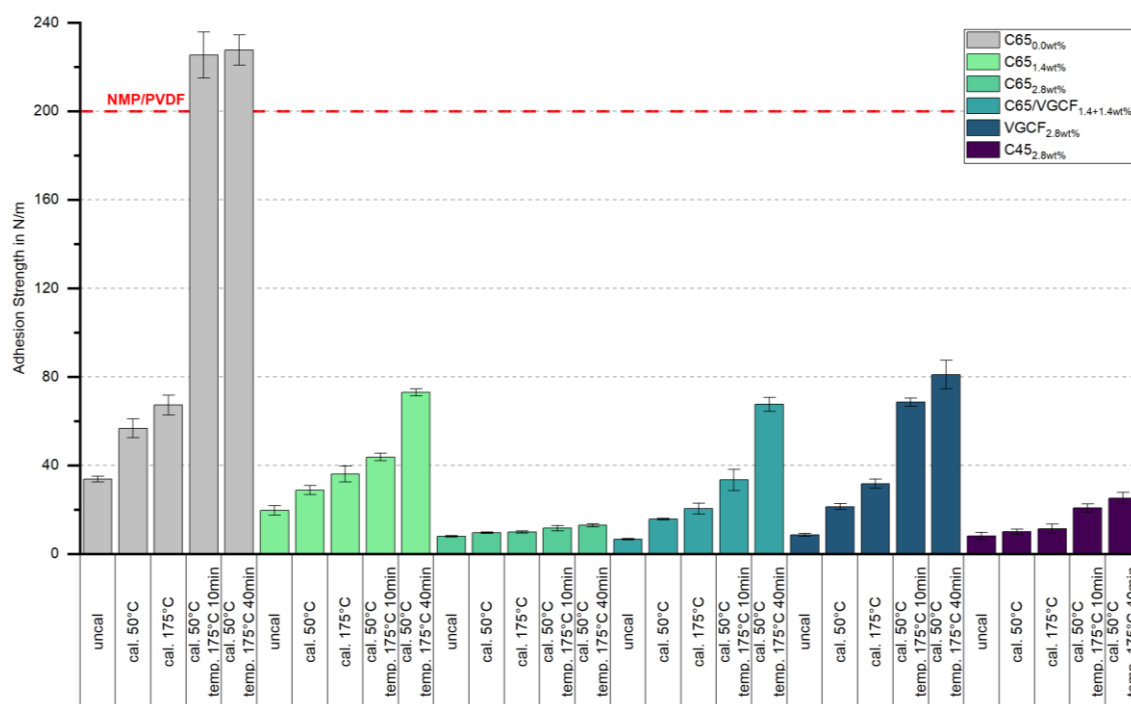
Figure 20 - Adhesion strength of uncalendered, calendered, and heat-treated cathodes, n=3, adapted from Weber et al. [154]

The low surface area VGCF (S = 12 m²/g) slightly reduces the mechanical strength of the cathode, evidenced by a decrease from 72.9 N/m for C65$_{1.4wt\%}$ to 67.5 N/m for C65/VGCF$_{1.4+1.4wt\%}$ in heat-treated samples. Nonetheless, the negative impact of VGCF on adhesion is significantly smaller than that of the high surface area C65 (S = 62 m²/g). Despite having the same CA amount as

C65/VGCF$_{1.4+1.4wt\%}$, the adhesion strength for C65$_{2.8wt\%}$ was measured at only 12.9 N/m. Looking at the adhesion strength of C45$_{2.8wt\%}$ which is at 25.2 N/m, it fits right into the measurement series with regard to the lower surface area of C45 (S = 45 m²/g).

A binder's ability to adhere to the various solid components and effectively bind them is essential for ensuring the mechanical integrity of an electrode. PVDF, being a semi-crystalline polymer, exhibits properties ranging from leathery to brittle below its melting temperature, dependent upon its molar mass. In aqueous processing, PVDF is present as latex rather than in a dissolved state, thereby necessitating heat treatment above its melting point. Upon melting, PVDF demonstrates a reduced viscosity, which facilitates enhanced wetting of the solid components within the cathode. [155] Consequently, the mechanical integrity of the cathode is improved not only by the increased contact area which results from improved wetting but also by the mechanical interconnecting of PVDF with the solid components. When molten, PVDF infiltrates cavities and gaps and subsequently solidifies, which results in robust mechanical bonds. [154]

To differentiate the effects of varying surface areas and surface chemistries of the CAs on adhesion strength and binder distribution, coatings of C65/VGCF$_{norm.}$ and VGCF$_{norm.}$ were produced. Assuming a quantity of 100 g, the total surface area (A) of all components in cathode C65$_{2.8wt\%}$ is 200.5 m². According to Landesfeind et al. [156] the theoretical binder layer thickness inside an electrode can be calculated according to the following equation:

$$d_{Bi} = \frac{\sum(\frac{m_{Bi}}{\rho_{Bi}})}{m_{LNMO} * BET_{LNMO} + m_{CA} * BET_{CA}} \tag{35}$$

The theoretical binder layer thickness for C65$_{2.8wt\%}$ is then calculated to be 13.5 nm from equation (35. The binder contents in C65/VGCF$_{norm.}$ (A = 130.5 m²) and VGCF$_{norm.}$ (A = 60.5 m²) were normalized to achieve a theoretical binder layer thickness of 13.5 nm, facilitating a comparison of the CAs independent of their surface area. The electrode compositions of these normalized samples are detailed in Table 7, reported with two decimal places to minimize rounding errors. The resulting adhesion strengths are presented in Figure 21.
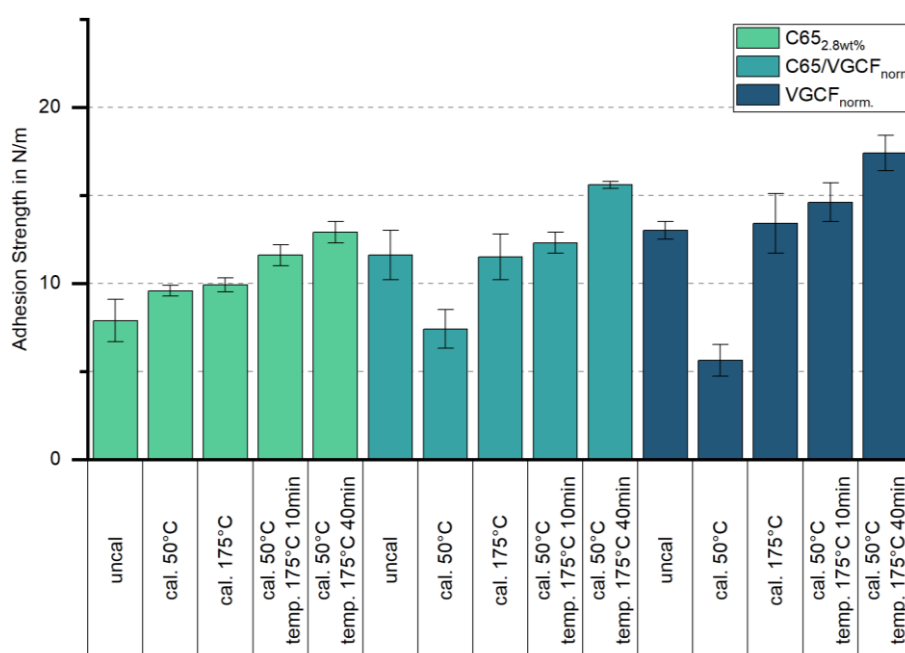
Figure 21 - Adhesion strength of cathodes with normalized binder contents, n=3, reproduced from Weber et al. [154]

A decrease in adhesion strength can be observed for both cathodes with normalized binder-to-surface area ratio when calendered at 50 °C. Meyer et al [141] attributed this reduction to the lateral stretching of the coatings due to differing elastic moduli between binder and aluminum and further demonstrated that the decline is particularly pronounced within the porosity range of 30 % to 35 %. However, annealing proves to be an effective way of restoring and improving mechanical integrity. With a normalized binder content, the impact of the type of CA becomes more evident. The maximum adhesion strength after 40 minutes of heat treatment ranges from 12.9 N/m for C65$_{2.8wt\%}$ to 15.6 N/m and 17.4 N/m for C65/VGCF$_{norm.}$ and VGCF$_{norm.}$, respectively, indicating a positive effect of VGCFs on mechanical integrity beyond their smaller surface area. [154]

Surface Free Energy

The results of the contact angle measurements for the tested cathode constituents using the reference liquids specified in chapter 2.3, along with the corresponding measurement methods are summarized in Table A 1. Since the WB method requires prior determination of the sample powder's capillary constant, these values are also provided. Contact angle measurements for CMC with water were omitted due to its solubility yielding unreliable results. As compiled in Table 7, the contact angles can be converted into the SFE of the individual electrode components, applying the OWRK model. [29–31] Included in the table are the overall SFE, the dispersive component (γ_s^d), the polar component (γ_s^p), and the interfacial free energy of interaction (ΔG^{IF}). The results demonstrate that coth C65 and C45 have a significantly large dispersive component and only a small polar component, which is consistent with literature findings. [87,157–159] C45 shows to be even slightly more disperse than C65. The current collector's SFE is highly similar to that of both CBs. The dispersive component of both polymer binders, PVDF and CMC, is dominant, though the polar component is higher than that of CB. The disperse and polar components of VGCF are more balanced compared to the CBs, yet they still exhibit predominantly dispersive SFE. The only

constituent with a larger polar than dispersive component is LNMO, which aligns with findings on another active material, namely LCO, in the literature. [87,154]

Table 8 - Surface free energy and free energy of adhesion of slurry components in relation to PVDF latex and CMC binder ± standard deviation (ΔG^{IF}_{132} annotated as $\Delta G^{IF}_{S\text{-}H2O\text{-}PVDF}$ and $\Delta G^{IF}_{S\text{-}H2O\text{-}CMC}$ with 1 representing the solid sample s, 3 the immersion liquid H$_2$O and 2 the respective polymer binder) reproduced from Weber et al. [154]

Solid sample	γ_S	γ_S^d	γ_S^p	$\Delta G^{IF}_{S\text{-}H2O\text{-}PVDF}$	$\Delta G^{IF}_{S\text{-}H2O\text{-}CMC}$
	(mJ/m²)				
C45	33.8 ± 1.5	31.3 ± 1.3	2.6 ± 0.2	-48.7 ± 0.5	-49.2 ± 0.8
Aluminum CC	35.5 ± 1.5	32.7 ± 1.3	2.8 ± 0.2	-48.5 ± 0.4	-49.0 ± 0.8
C65	31.7 ± 1.2	28.6 ± 1.0	3.1 ± 0.2	-46.7 ± 0.5	-47.1 ± 0.8
CMC	47.3 ± 1.5	38.5 ± 1.2	8.8 ± 0.4	-38.9 ± 0.4	-39.7 ± 0.5
PVDF Latex	44.2 ± 1.0	35.4 ± 0.9	8.8 ± 0.2	-38.2 ± 0.2	-38.9 ± 0.4
VGCF	19.7 ± 1.5	12.8 ± 1.1	6.9 ± 0.4	-34.9 ± 0.8	-34.4 ± 1.0
LNMO	55.6 ± 1.1	25.6 ± 0.9	30.0 ± 0.2	-14.9 ± 0.1	-15.1 ± 0.1

The preferential adhesion order for both binders can be derived from the decreasing magnitude of the free energy of interaction, ranging from the most negative to the least negative as follows: C45 > CC > C65 > (CMC, PVDF) > VGCF > LNMO. The interaction between both C45 and the CC with the polymer binders is almost identical exhibiting the most negative values around -49.0 mJ/m² with CMC and -48.5 mJ/m² with PVDF. They are closely followed by C65 which results in ΔG^{IF} values of -47.1 mJ/m² with CMC and -46.7 mJ/m² with PVDF. Therefore, both binders are expected to preferentially adhere to the CBs and the CC due to the interface formation between them being the most energetically favorable. The favorable interaction of the binders with both CBs indicates the formation of carbon-binder-domains (CBD). ΔG^{IF} between the two binders is -38.9 mJ/m². VGCF shows ΔG^{IF} values of -34.9 mJ/m² with PVDF and -34.4 mJ/m² with CMC. LNMO is indicated to be the least preferred binding partner within the slurry for both polymer binders as ΔG^{IF} results in values of -14.9 mJ/m² and -15.1 mJ/m² with PVDF and CMC, respectively. [154] As the value of ΔG^{IF} for the interaction of PVDF with itself is -38.2 mJ/m², it suggests a higher tendency for PVDF to coagulate than to form an interface with the VGCF or the LNMO. The same is true for the CMC with a value of -39.7 mJ/m². This may lead to homogeneity issues when solely VGCF and LNMO are applied.

Binder Distribution

The LNMO particles in electrodes C65$_{2.8wt\%}$ and C45$_{2.8wt\%}$ are seemingly covered by the CBDs as can be seen in the respective SEM images in Figure 22 A/1 and F/1. Nonetheless, the formation of large gaps between the LNMO particles and the CBDs, observable in Figure 22 A/1 and F/1, indicates insufficient adhesion of the CMC and PVDF towards the active material. Interestingly, Foster et al. [139] observed the same peeling behavior while working with a combination of NMC as active material and PVDF. The CCs of C65$_{2.8wt\%}$ and C45$_{2.8wt\%}$ were further found to be almost bare, with slightly more CBDs adhering to the CC of C45$_{2.8wt\%}$ but generally only where LNMO particles have been pressed into the aluminum during calendering. A reduction of the CA content to 1.4 wt% or 0.0 wt% results in reduced or complete absence of the gaps as well as improved active material coverage by the polymer binders, as depicted in Figure 22 B/1 and C/1, respectively.
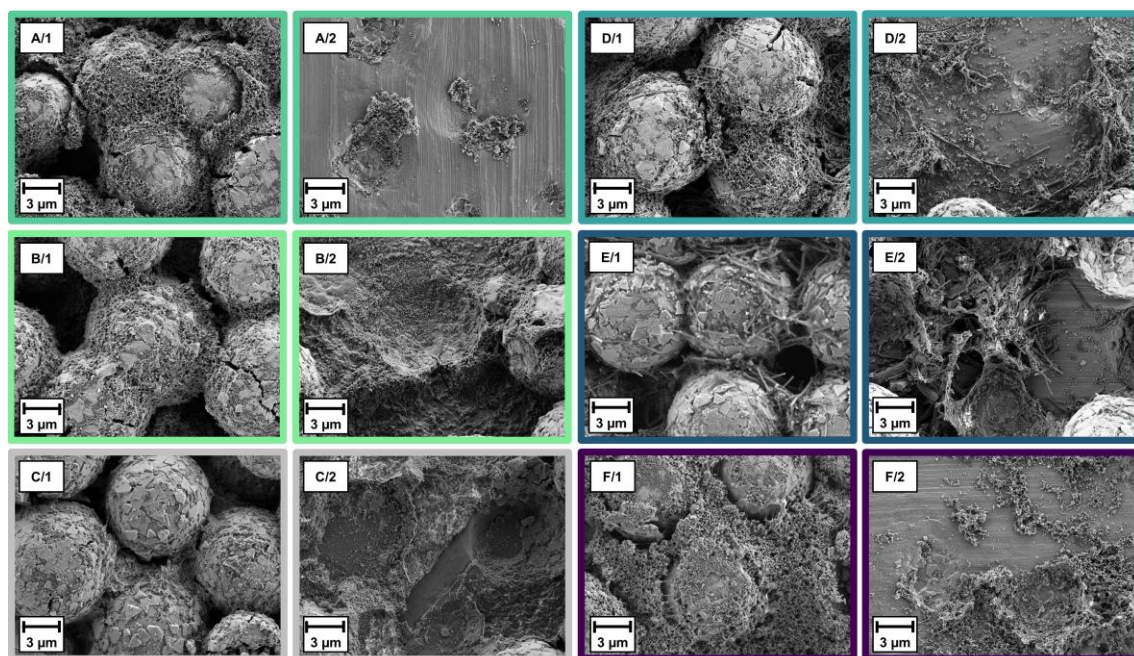
Figure 22 - SEM micrographs of coatings C65$_{2.8wt\%}$ (A), C65$_{1.4wt\%}$ (B), C65$_{0.0wt\%}$ (C), C65/VGCF$_{1.4+1.4wt\%}$ (D), VGCF$_{2.8wt\%}$ (E), C45$_{2.8wt\%}$ (F), after calendering at 50 °C to 30 % porosity and heat treatment treatment at 175 °C for 40 minutes of top view (X/1) and current collector (X/2) after 90 ° peel tests adapted from Weber et al. [154]

As illustrated in Figure 23, EDS analysis of the CC revealed the formation of a thin coating layer consisting of intermingled CMC and PVDF for some of the investigated electrodes. Due to the installation angle of the EDS detector and resulting shadowing effects, the upper left corner of the elemental mappings appears dark. No gap formation between the CBDs and the LNMO can be observed in electrodes C65/VGCF$_{1.4+1.4wt\%}$ and VGCF$_{2.8wt\%}$ (Figure 22 D/1 and E/1). Although the amount of CA in both coatings is identical to C65$_{2.8wt\%}$ and C45$_{2.8wt\%}$, they contain the coating film on the surface of the CC.
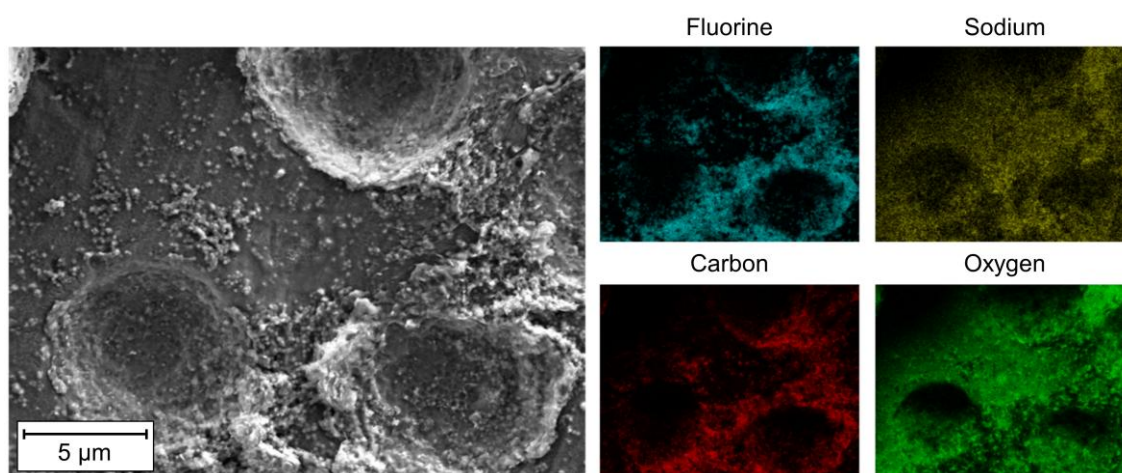
Figure 23 - Current collector of electrode C65$_{1.4wt\%}$ after 90° peel test analyzed by EDS revealing the formation of a CMC/PVDF layer reproduced from Weber et al. [154]

SEM images of cross-sections prepared by ion milling are compiled in Figure 24. The formation of large gaps between the CBDs and the active material is observable throughout the entire thickness of electrode C65$_{2.8wt\%}$. Some active material particles lie seemingly contactless between the CBDs, which again illustrates the poor adhesive behavior of the CBDs towards the LNMO. Moreover, C65$_{2.8wt\%}$ showed partial delamination of the coating from the CC (Figure 24 A). Improved adhesion of the binders towards LNMO becomes evident with partial substitution of CB by VGCF as well as overall reduction of the CA. In the absence of CA (Figure 24 B) the polymer binders fully cover the active material particles. An improved coverage of LNMO by the binders can be seen in cathode C65/VGCF$_{1.4+1.4wt\%}$ (Figure 24 C). Nonetheless, gap formation, in a lesser extent, is still visible. With both lesser CA content and CB substitution delamination does not occur. The predicted homogeneity issues can be evidenced in the form of non-deagglomerated VGCF clusters throughout electrode C65/VGCF$_{1.4+1.4wt\%}$. They are argued to arise due to both binders preferably coagulating rather than binding onto the VGCF. [154]
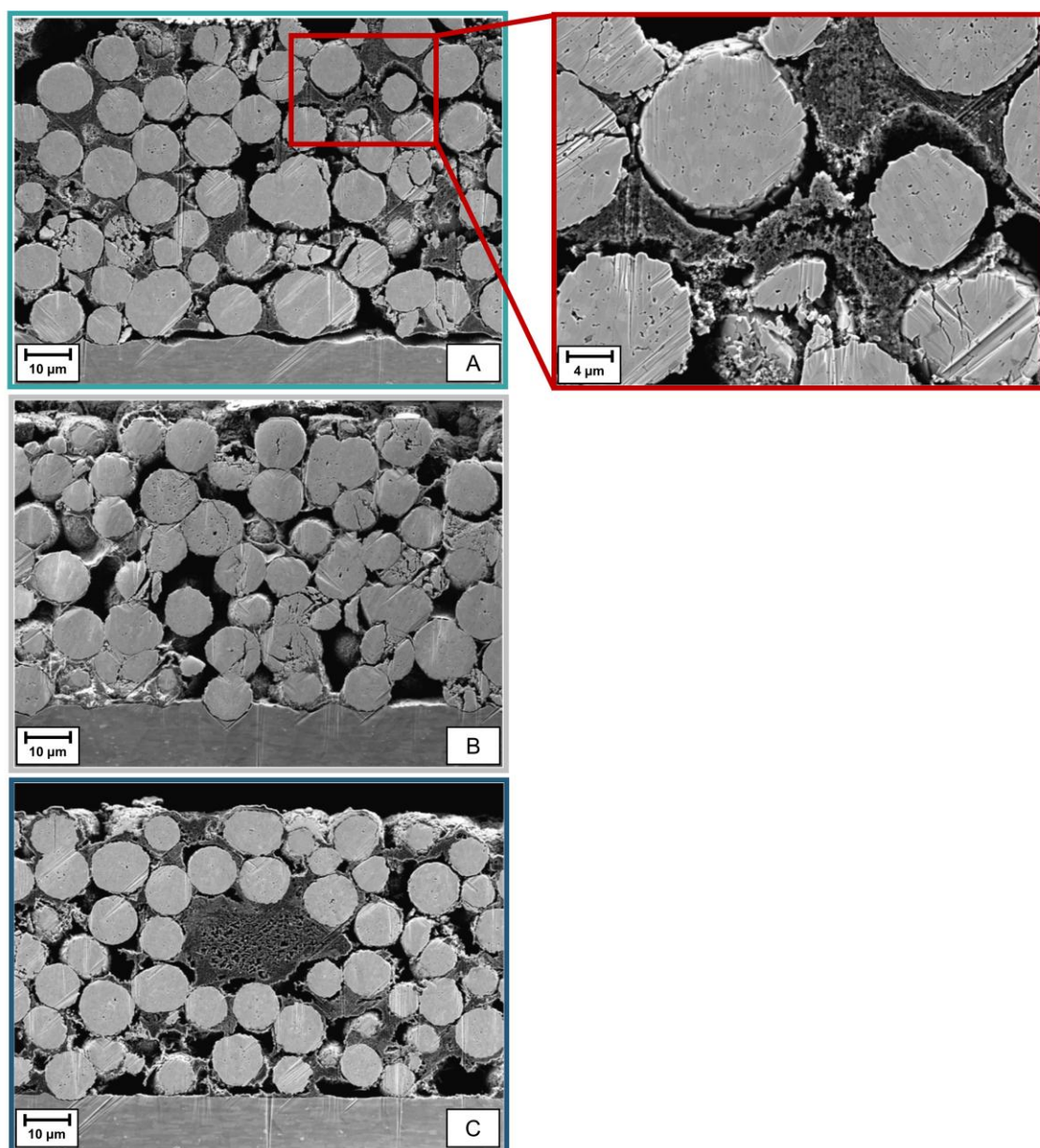
Figure 24 - SEM micrographs of ion-milled cross sections of (A) C65$_{2.8wt\%}$, (B) C65$_{0.0wt\%}$ and (C) C65/VGCF$_{1.4+1.4wt\%}$ (left) and a higher magnification of C65$_{2.8wt\%}$ showing the lack of interaction between LNMO and CBDs (right) reproduced from Weber et al. [154]

Due to the energetically favorable interaction between both polymeric binders and CB the preferred formation of carbon-binder-domains is to be expected and is evidenced by Figure 22 A/1 and F/1. Further, the unfavored interaction of LNMO with both binders is indicated by the calculation of ΔG^{IF}. [160] The CBDs only disperse around the active material while not properly adhering to its surface due to this lack of attraction. [160,161] Polymers display a tendency for chemical bonding or adsorption when coming into contact with the surfaces of the CA or the active material as reported in literature. [40,88] By aligning their chain ends with the respective surface they form bound polymer layers. Interaction with neighboring polymer layers leads to the polymer chains losing their mobility resulting in fixed/immobilized layers. Only when the surface

of the conductive additive and the active material are saturated by fixed polymer layers, unbound polymer domains start to form. It can be observed in Figure 22 A/1 and F/1 that because of the high affinity of PVDF and CMC towards both C45 and C65 and their significantly large surface area within the respective electrode the vast majority of binder polymers are fixed inside the CBDs. However, the free binder domains are substantial for maintaining both adhesive and cohesive integrity of the electrode. [40,162,163] Focusing on the cathodes containing C65, the aluminum CC acts as an even more preferred surface to the binders than the CB, which would hint at high adhesion strength due to migration of the binders towards the CC being thermodynamically favored. However, the overall process of cathode manufacturing has to be kept in mind. During preparation of the slurry CMC, PVDF, and CB undergo dispersing by a disc agitator. The CC only comes into contact with the polymer binders during the subsequent casting. The binders have already formed immobilized polymer layers on the CA during slurry preparation which only leaves a minuscule fraction of free binder to form an adhesive bond towards the CC. By reducing the CA's surface area, the surface of the CA is saturated faster by the binder. This is followed by the formation of free polymer domains which will then tend to adsorb onto the CC as expected according to the calculations in Table 8 and evidenced in Figure 23.

Going back to the results of the adhesion strength tests in Figure 20, the differently pronounced improvements after heat-treatment can also be explained by the free energy of adhesion and the resulting binder distribution. With regard to C65$_{2.8wt\%}$ and C45$_{2.8wt\%}$, containing mostly dispersive, high surface area carbon black, heat treatment beyond T$_{melt}$ leads mostly to additional wetting of the CB because the majority of CMC and PVDF is already occupied inside the CBDs. In the absence of CB, e.g. in C65$_{0.0wt\%}$ and VGCF$_{2.8wt\%}$, molten PVDF is able to directly wet the CC and the active material making heat treatment at T$_{melt}$ for 10 minutes sufficient to reach maximum adhesion strength. When molten, PVDF initially wets CB in electrodes C65$_{1.4wt\%}$ and C65/VGCF$_{1.4+1.4wt\%}$. As evidenced in Figure 23, through longer exposure times above T$_{melt}$, PVDF proceeds to also wet LNMO and the CC. The enhanced coverage of the active material in the absence of C65 as well as the observed coating layer on the CC are also evidenced by a rise in interface resistance and bulk resistivity (Figure 25). Electrode C65$_{1.4wt\%}$ after calendering and annealing did not allow for the measurement of bulk resistivity and interface resistance as they were out of the upper measuring limit of the Hioki resistance meter. Electrode C65$_{0.0wt\%}$ was not measurable at all. [154]
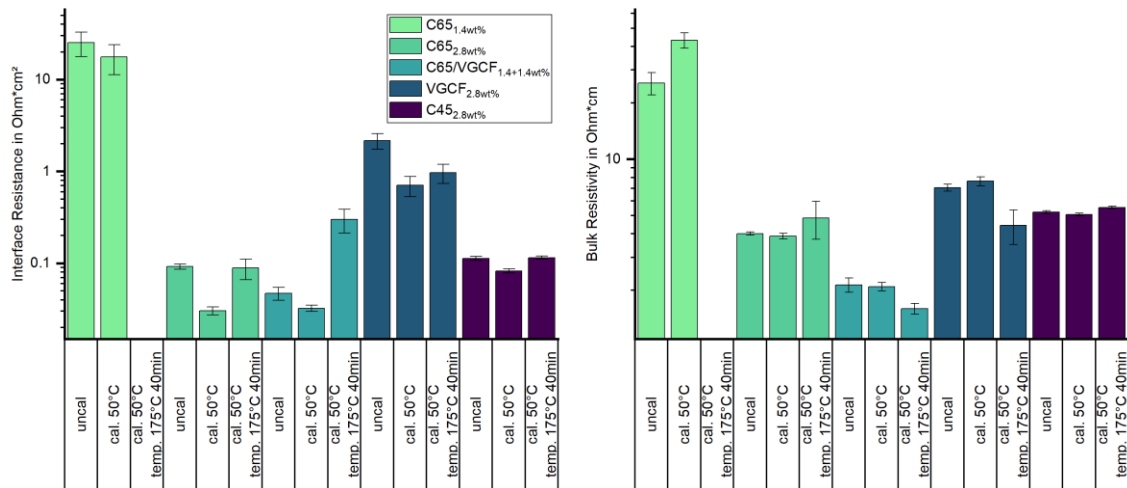
Figure 25 - Bulk resistivity (left) and interface resistance (right) of uncalendered, calendered and annealed cathodes with standard deviation, n = 5, adapted from Weber et al. [154]

Electrochemical Characterization

Rate capability tests, depicted in Figure 27, range from 0.1 C up to 10 C. Cathodes with a reduced amount of CA, namely C65$_{1.4wt\%}$ and C65$_{0.0wt\%}$, show inferior rate performance compared to cathodes containing 2.8 wt% CA. Due to its very high bulk resistance and interface resisitivity, C65$_{0.0wt\%}$ cannot be cycled potentiostatically. The theoretical binder layer thickness of each individual cathode, illustrated in Figure 26, can be calculated according to Equation 35. [156] Thus, a reduction of the total surface area of CA results in higher tortuosity of the electrode. In accordance with the literature this is argued to be due to an excess amount of free binder accumulating in the spandrels of the active material particles effectively disconnecting the individual pores of the cathode. [164]
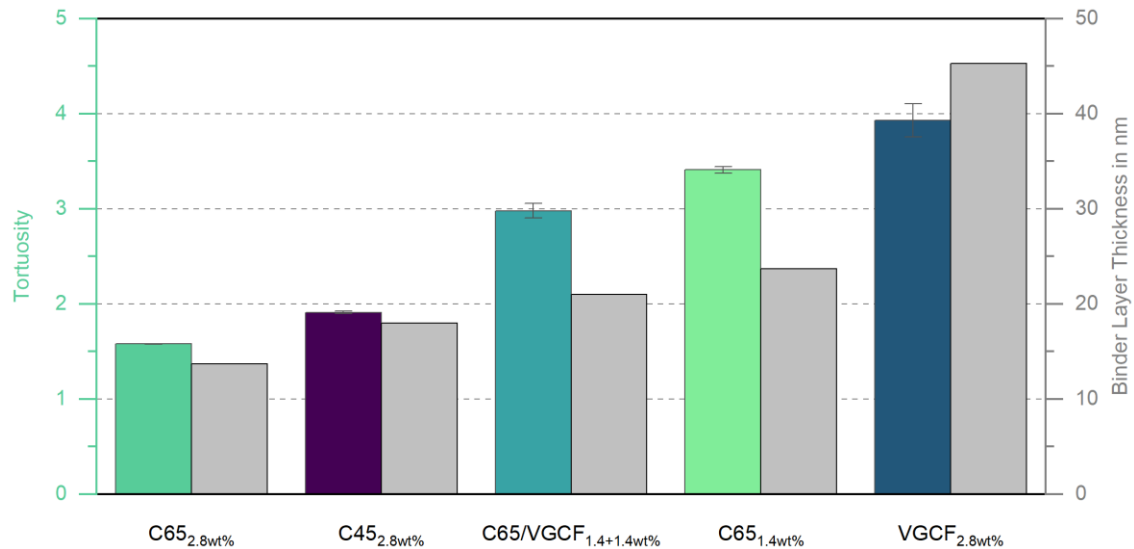
Figure 26 - Tortuosity of cathodes after calendering and annealing for 40 minutes at 175 °C in relation to theoretical binder layer thickness with standard deviation, n=3, adapted from Weber et al. [154]

Yet, there is no correlation between tortuosity and rate performance of the cathodes. However, they correspond well with both bulk and interface resistivity of the coatings (Figure 25). The heightened electrical resistivity results in an increased overpotential during charging and discharging. This ultimately leads to an incomplete sequence of redox reactions in the chosen voltage window of 3.5 V - 4.9 V vs Li/Li$^+$. It cannot be determined whether interface resistance or bulk resistivity is dominating the limitation of C-rate performance. It can, however, be concluded that at the examined porosity and loadings overall electrical resistivity is the limiting factor of C-rate performance.
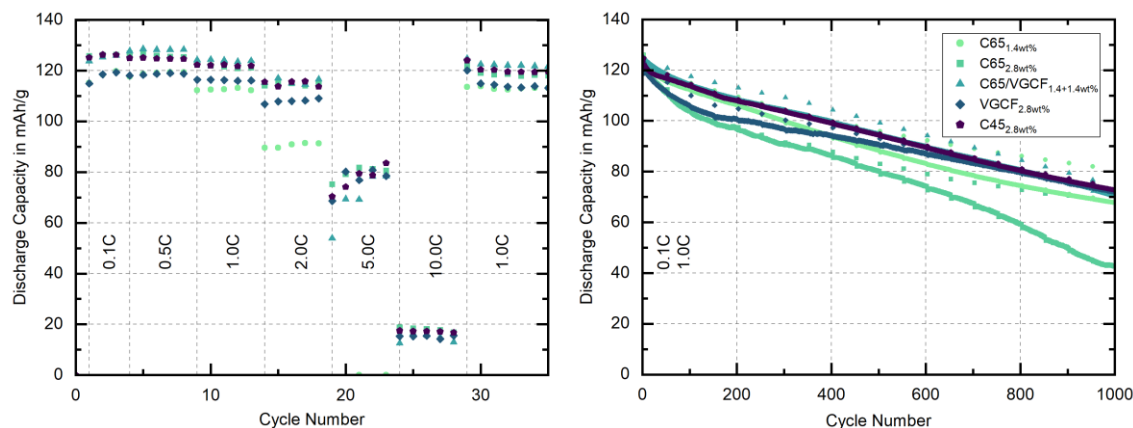
Figure 27 - Rate capability (left) and long-term cycling performance (right) of cathodes containing different conductive additives in full cell configuration, n=3, adapted from Weber et al. [154]

The initial discharge capacity of all investigated cathodes is very similar around 124 mAh/g, as can be seen in the right plot of Figure 27. While the degradation of cathodes C65$_{0.0wt\%}$, C65$_{1.4+1.4wt\%}$, VGCF$_{2.8wt\%}$, and C45$_{2.8wt\%}$ is comparable, C65$_{2.8wt\%}$ starts exhibiting a continuously increasing sharp degradation after approx. 500 cycles. With every 50th cycle performed at a C-rate of 0.1 C/0.1 C (charge/discharge) it can be observed that a discharge capacity comparable to all other cathodes is achieved when charging at a low C-rate. This indicates that the loss in discharge capacity is not mainly a result of active material degradation but rather delamination of the cathode coating from the current collector or the reduction of contact points between the CBDs and LNMO induced by volume changes during cycling. [29] At the applied C-rate of 1 C, discharging cannot be completed in time as charge transfer is impeded by the loss of contact points to the current collector. At lower C-rates, however, the time for charge transfer through the remaining contact points is sufficient, resulting in a higher capacity retention. [134,135,165,166]
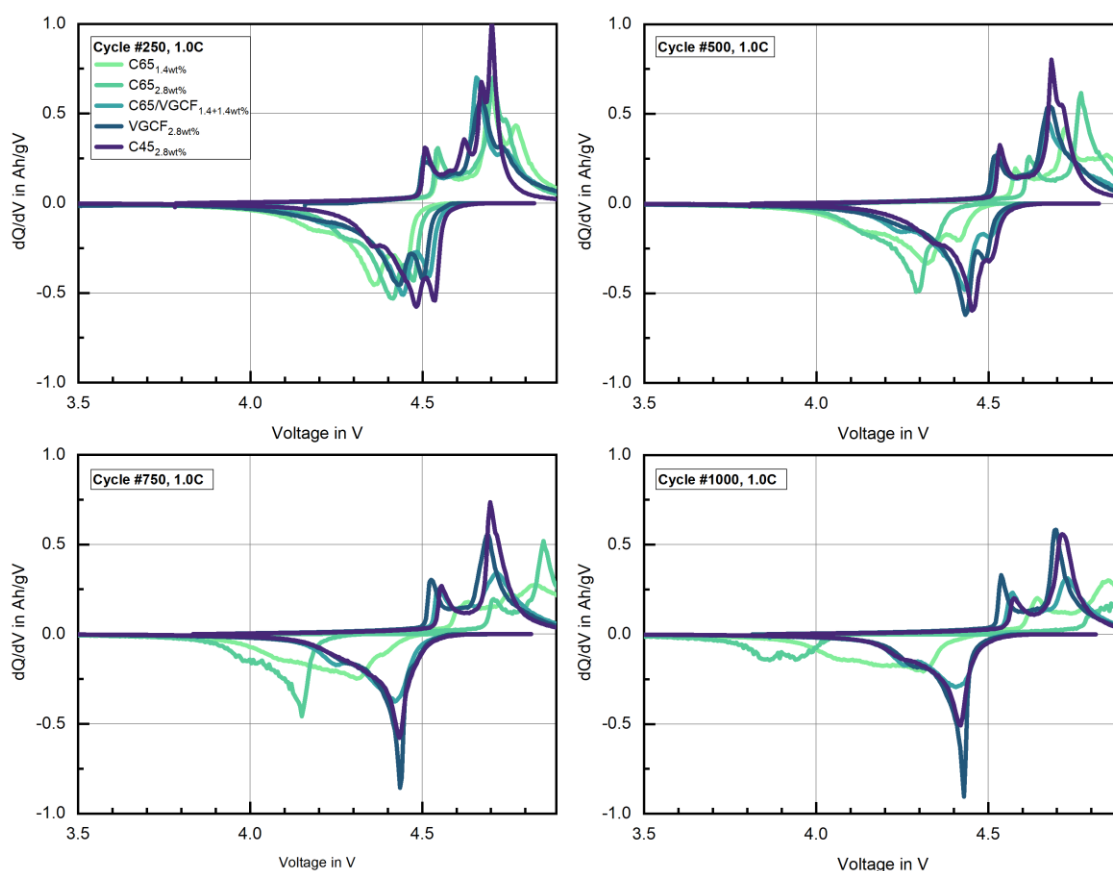
Figure 28 - Comparison of differential capacity curves of cycles 250, 500, 750 and 1000 adapted from Weber et al. [154]

The shifts in charge and discharge potentials between cycles 250, 500, 750, and 1000 are illustrated in Figure 28. C65$_{2.8wt\%}$, containing only C65 as CA, displays a significant increase in polarization. This further proves delamination to be the main cause for loss of discharge capacity because it leads to incomplete charging and discharging as the cathodes move out of the charging window of 3.5 V - 4.9 V. To some extent, this can be compensated by a CV step in the charging protocol. However, as delamination progresses the CV step becomes insufficient. It is interesting to note that Sahore et al. [29] demonstrated the same degradation mechanism in their work on NMC 811 also using a combination of CMC and PVDF latex as binder system. Yet, a rise in polarization is also observable for electrodes C65$_{1.4wt\%}$ and C45$_{2.8wt\%}$ containing only CB as CA. This can be attributed to the advancing deterioration of the conductive network as several authors have demonstrated that at high potentials both LP30 and CB are unstable. [15–18,167,168] C65/VGCF$_{1.4+1.4wt\%}$ exhibits a lesser degree of polarization. VGCF provide fewer reaction sites for parasitic oxidation of the electrolyte due to their smaller surface area which results in less hydrogen fluoride generation and consequently less damage to the cathode. [16,18,121] The long-range conductivity of the VGCFs is argued to simultaneously compensate for the loss of electrical conductivity associated with the oxidation of the CB to CO and CO$_2$. [18] Only a negligible change in polarization over 1000 cycles is visible for VGCF$_{2.8wt\%}$. This indicates that loss of lithium inventory and loss of active material are the leading factors for the exhibited capacity loss. [134,135,166]

6.1.3 Conclusion

By the obtained surface free energies, one of the main driving forces in binder distribution, the interfacial free energy of adhesion, could be calculated for each relation between two electrode constituents. It has been found that the interaction of constituents inside aqueous slurries is highly dependent upon the surface free energy of the applied conductive additive. Surface chemistry causes preferential adhesion of the polymeric binders towards the CA, resulting in the formation of CBDs and low mechanical integrity due to a lack of free polymer domains. It was shown that there are two possible solutions to improve the adhesion strength of aqueously processed cathodes. The first and most effective one is the reduction of the CA's surface area as unbound polymer domains will become available with saturation of the CA surface. Secondly, the application of VGCFs exhibiting lesser affinity towards the binders was also demonstrated to be an adequate way of improving adhesion strength. Whilst the exact threshold of sufficient mechanical integrity regarding long-term cycling has not been investigated, all of the applied methods proved the successful elimination of capacity loss due to delamination from the CC. It has further been established that an excess amount of free binder domains results in an increase of electrode tortuosity due to clogging of the pores, validating simulation works on electrode tortuosity for the first time with experimental data. The beneficial effect of the VGCFs' smaller surface area was found to go beyond the improvement of adhesion strength. Due to fewer reaction sites for parasitic side reactions of the electrolyte at high voltages of 4.9 V the respective cathodes exhibited less degradation.

6.2 Influence of the PVDF Latex Binder

Partial findings of this chapter have been published in Nature Scientific Reports, Volume 15, on March 23rd 2025 as "The Impact of Binder Polarity on the Properties of Aqueously Processed Positive and Negative Electrodes for Lithium-Ion Batteries". The following chapter investigates the influence of varying SFE of various PVDF latex binders on the properties and the electrochemical performance of the resulting cathodes. The latices are chosen to cover a large spectrum of different SFE distributions from primarily dispersive to mainly polar contributions. All latices investigated in this work have the same PVDF backbone. However, they differ in their distinctive functionalizations, which cannot be disclosed in this work.

6.2.1 Experimental

Materials

Table 9 - Materials - influence of the binder

Reference	Name	Manufacturer	Particle size d_{50} (nm)
LNMO	TBM-129	Haldor Topsoe, Denmark	10700
C65	C-NERGY Super C65	Imerys Graphite & Carbon, Switzerland	40
CMC	Walocel CRT 2000 PA 07	DuPont, USA	-
Latex 1	Kynar®, experimental	Arkema, France	145
Latex 2	Kynar®, experimental	Arkema, France	148
Latex 3	Kynar® Latex 32	Arkema, France	152
Latex 4	Kynar® LBG4330X	Arkema, France	149
LP30	LP30, battery grade	Sigma-Aldrich, USA	-

Electrode Manufacturing

Table 10 - Cathode properties - influence of the binder

Reference	LNMO	CMC	PVDF	C65	Areal capacity
	(wt%)				(mAh/cm²)
Latex 1	92.6	1.8	2.8	2.8	1.9 ± 0.1
Latex 2	92.6	1.8	2.8	2.8	2.0 ± 0.1
Latex 3	92.6	1.8	2.8	2.8	1.9 ± 0.1
Latex 4	92.6	1.8	2.8	2.8	1.9 ± 0.1

Cell Assembly

Foregoing the assembly of the cells, the electrodes were dried at 110 °C for 4 h in a vacuum oven to evaporate residual water. Alternatively, the electrodes were dried at 110 °C for 24 h under vacuum and additional 24 h under vacuum at room temperature.

Surface Free Energy

The PVDF latices were pressed into pellets with a diameter of 14 mm by applying a nominal load of 500 kPa after drying at 50 °C under vacuum and subsequently measured via sessile drop. LP30 was measured by pendant drop. All investigations involving electrolyte were performed in a dry room (dew point T_d = -60 °C) to preclude measurement errors due to the reaction of LiPF$_6$ with atmospheric water.

Adhesion Strength Testing

Measurements were conducted after calendering at 50 °C (GKL200, Saueressig, Germany) and drying in a vacuum oven at 110 °C for 4 h or 24 h.

Corona Treatment

The wattage was constantly set to 900 W at a line speed of 0.2 m/min, corresponding to a watt density of 25.5 J/cm².

6.2.2 Results and Discussion

Mechanical Properties

Adhesion strength tests of the coatings show significant differences depending on the applied PVDF latex. The coating containing Latex 1 as main binding agent exhibited an adhesion strength right after coating so low that the electrode delaminated from the current collector at the slightest bending which made it impossible to prepare samples for the adhesion strength measurement. Through calendering at 50 °C and subsequent heat treatment at 110 °C for 4 h or 24 h adhesion strength marginally improved to 1.4 N/m, 1.6 N/m, and 2.2 N/m, respectively. The cathode comprising Latex 4 has an adhesion strength of 22.5 N/m already in its uncalendered state. While calendering causes an initial decline of mechanical integrity to 7.6 N/m, which is in line with the findings on adhesion strength by Meyer et al. [141], it can be restored by successive heat treatment at 110 °C. This even results in a further rise to 26.8 N/m for a heat treatment of 4 h and 31.4 N/m when subjecting the cathode to 110 °C for 24 h.
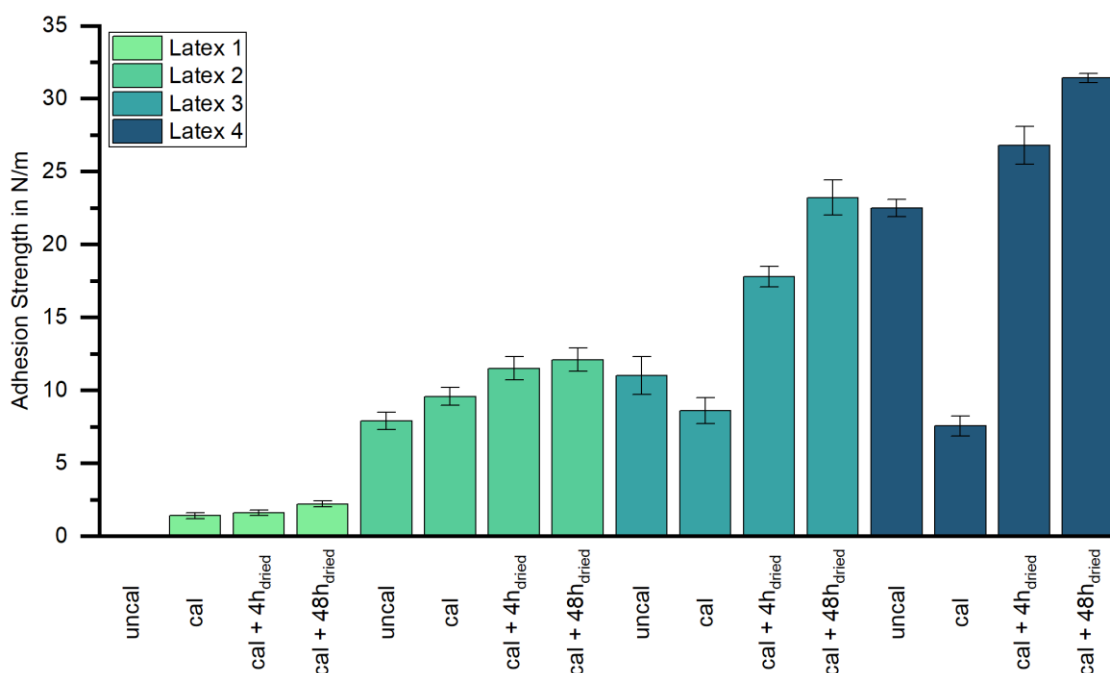
Figure 29 - Adhesion Strength of uncalendered, calendered and dried cathodes in dependence of the applied PVDF latex adapted from Weber and Keim et al. [64]

Surface Free Energy

The results of the contact angle measurements of the latices with DIM, EG, and water are listed in Table A 2. Applying the OWRK model makes it possible to calculate the latices' surface free energy from the measured contact angles. SFE of all applied cathode constituents is given in Table 11 with γ_S denoting the overall SFE of the solid sample and γ_S^d and γ_S^p designating the dispersive and polar component, respectively. Latex 1 throughout Latex 3 all show very similar dispersive components around 36 mJ/m². They vary, however, in their polar parts, ranging from 4.5 mJ/m² for Latex 1 to 11.3 mJ/m² for Latex 3. Therefore, also exhibiting an increase in their overall SFE.

Latex 4 is the only PVDF latex with a larger polar (31.6 mJ/m²) than dispersive component (22.4 mJ/m²). Looking at the polarity, an increasingly larger percentage of the binders can be noted. Latex 1 has the lowest polarity of 11.1 %, Latex 2 exhibits a surface polarity of 19.9 %, Latex 3 with 24.0 % and Latex 4 shows the highest polarity of 58.5 %. All other investigated cathode constituents showed significantly larger dispersive than polar components with exception of LNMO having a dispersive contribution of 25.6 mJ/m² and a polar contribution of 30.0 mJ/m².

Table 11 - Surface free energy of different cathode materials calculated from contact angles with DIM, EG and water according to the OWRK method, SFE of LP30 was determined through the pendant drop method, n=3

Sample	γ_s	γ_s^d	γ_s^p	Polarity
	(mJ/m²)			(%)
Aluminum CC [1]	35.5 ± 1.5	32.7 ± 1.3	2.8 ± 0.2	7.9
C65 [1]	31.7 ± 1.2	28.6 ± 1.0	3.1 ± 0.2	9.8
CMC [1]	47.3 ± 1.5	38.5 ± 1.2	8.8 ± 0.4	18.6
LNMO [1]	55.6 ± 1.1	25.6 ± 0.9	30.0 ± 0.2	54.0
Latex 1	40.4 ± 0.5	35.9 ± 0.4	4.5 ± 0.1	11.1
Latex 2	43.7 ± 0.7	36.5 ± 0.6	7.2 ± 0.1	16.5
Latex 3	47.0 ± 2.8	35.7 ± 2.4	11.3 ± 0.4	24.0
Latex 4	54.0 ± 2.9	22.4 ± 2.4	31.6 ± 0.5	58.5
LP30	53.4 ± 0.4	53.2 ± 5.4	0.2 ± 5.4	0.4

[1] Values reproduced from Weber et al. [154]

By applying equations 21 and 25 to the SFE values in Table 11 the interfacial free energy of adhesion for each individual slurry component with each binder can be calculated.

Table 12 - Free energy of adhesion of slurry components with the different PVDF latices (ΔG^{IF}_{132} annotated as $\Delta G^{IF}_{S\text{-}H2O\text{-}Latex}$ with 1 representing the solid sample s, 3 the immersion liquid H_2O and 2 the respective PVDF latex), n=3

Sample	$\Delta G^{IF}_{S\text{-}H2O\text{-}Latex\ 1}$	$\Delta G^{IF}_{S\text{-}H2O\text{-}Latex\ 2}$	$\Delta G^{IF}_{S\text{-}H2O\text{-}Latex\ 3}$	$\Delta G^{IF}_{S\text{-}H2O\text{-}Latex\ 4}$
	(mJ/m²)			
Aluminum CC	-57.8 ± 0.6	-51.7 ± 0.3	-44.2 ± 0.4	-16.8 ± 0.1
C65	-55.9 ± 0.5	-49.8 ± 0.4	-42.5 ± 0.6	-16.4 ± 0.4
CMC	-46.1 ± 0.5	-41.5 ± 0.3	-35.7 ± 0.1	-13.5 ± 0.8
LNMO	-17.7 ± 0.1	-15.9 ± 0.1	-13.7 ± 0.1	-5.1 ± 0.1

From the obtained values for $\Delta G^{IF}_{S\text{-}H2O\text{-}Latex}$ it can be concluded that all latices show the same order of preferential adhesion while submerged in water with the highest affinity towards the current collector as the largest amount of energy would be released during the creation of an interface. This is followed by the C65 and the CMC. LNMO poses as the least preferred surface. As the latices are thoroughly dispersed with the C65, the CMC, and the LNMO already during slurry preparation before coming into contact with the aluminum it is fitting to initially disregard the free energies of adhesion with the current collector when interpreting the calculated values. While the order of preferential adhesion remains the same for all latices they, however, vary greatly in the values of $\Delta G^{IF}_{S\text{-}H2O\text{-}Latex}$. Focusing on $\Delta G^{IF}_{S\text{-}H2O\text{-}Latex\,1}$ the difference in free energy of adhesion between C65 and LNMO is 39.2 mJ/m² making C65 a much more probable binding partner for Latex 1 than the LNMO. When comparing $\Delta G^{IF}_{S\text{-}H2O\text{-}Latex}$ of C65 and LNMO for the other latices, it can be observed that the difference in ΔG^{IF} continuously decreases to 34.9 mJ/m² for Latex 2, 29.8 mJ/m² for Latex 3 and reaches a value of as little as 11.6 mJ/m² for Latex 4. This makes it much more likely for Latex 4 to also interact with LNMO while in the presence of C65 than it is for Latex 1 which further translates to a more homogeneous distribution between all components of the slurry. [63] This can be evidenced by a rise in bulk resistivity, depicted in Figure 30, as the interaction between the conductive additive and the respective binders lessens from Latex 1 to Latex 4 leading to less conductive carbon binder domains and more insulating free polymer binder particles throughout the electrode. It is further indicated by the heightened interface resistance. Since all binders show the highest affinity towards the aluminum current collector while submerged in water, polymer domains that are unbound due to the lessened interaction with the carbon black tend to form an interface with the aluminum foil. Moreover, calendering leads to a decrease in both interface resistance and bulk resistivity due to improved particle-particle contact and shortening of electrical pathways which is in line with findings of various other authors. [169,170] Cathodes dried for 24 h at 110 °C under vacuum and subsequent 24 h under vacuum at room temperature exhibited heightened resistivity values compared to cathodes dried for 4 h at 110 °C under vacuum. This is in good agreement with the findings in chapter 6.1.2 and is attributed to the more pronounced wetting of all constituents in the cathode by the insulating PVDF latex upon heat treatment. [154]
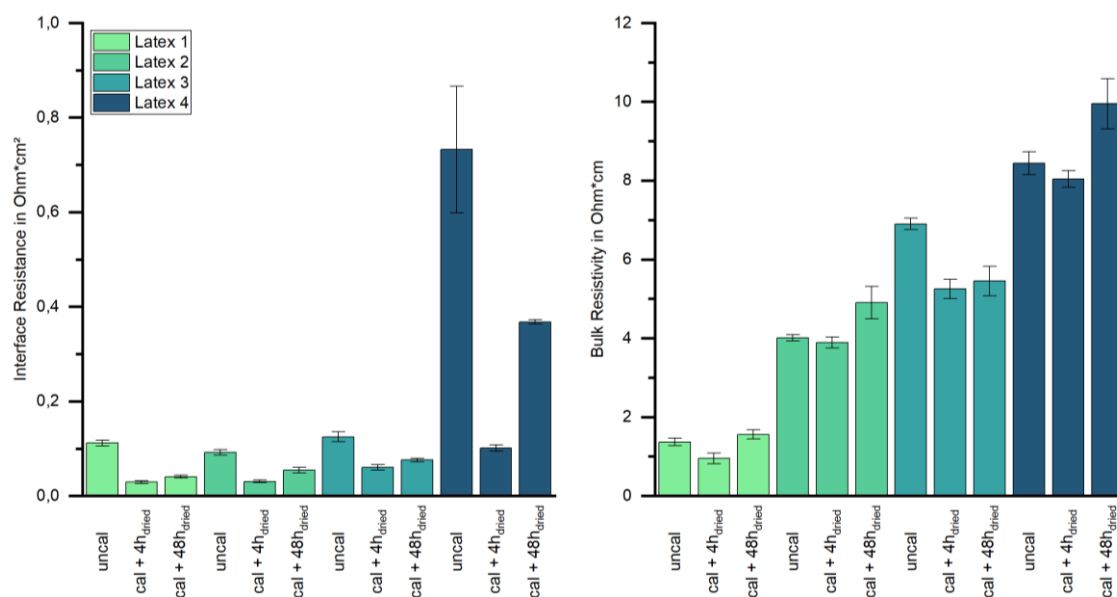
Figure 30 - Interface resistance (left) and bulk resistivity (right) of uncalendered and calendered and dried cathodes with standard deviation, n=5, adapted from Weber and Keim et al. [64]

Electrolyte Wettability

Further investigations show that the applied latex, even though it makes up as little as 2.8 wt% of the electrode, has a substantial impact on the wettability of the cathode by the electrolyte used in this work. To obtain accurate absorption rates it is essential to calender the electrodes to the exact same porosities since differences could potentially distort the measurement. Figure 31 illustrates the absorption rates of LP30 on the different cathodes based on the advancing contact angle. Latex 2 and Latex 3 both form initial contact angles right after drop deposition with the electrolyte of approx. 48°. In comparison, Latex 4 already has a higher initial contact angle with LP30 of 56.9°. The contact angles of LP30 with Latex 2 and 3 proceed to rapidly become smaller, reaching roughly 2° after 1.5 s and then stay constant throughout the remaining measurement, indicating almost ideal wettability of the cathodes. In contrast, the contact angle of LP30 with Latex 4 rapidly decreases to 15° and then continues to slowly advance to 8° over the course of the measurement, showing overall lesser wettability of the cathode.
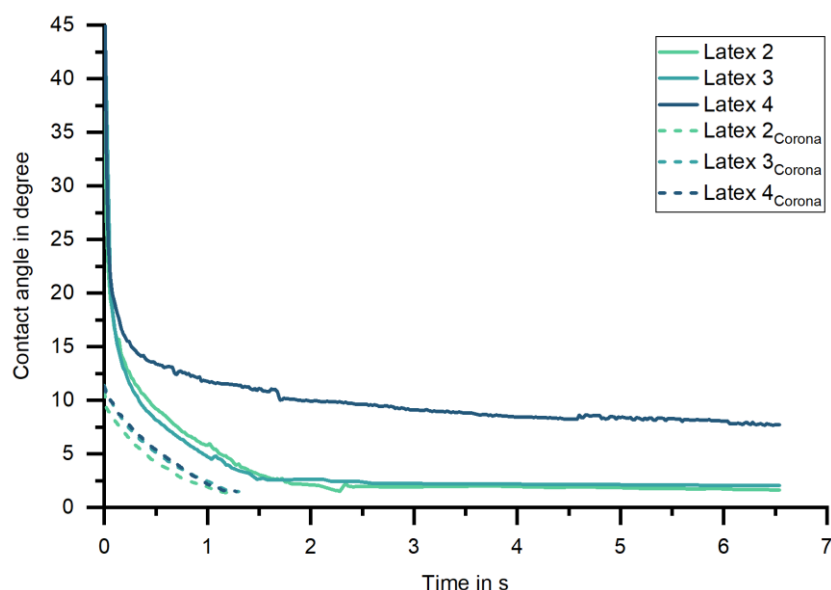
Figure 31 - Absorption rate determined through the advancing contact angle of LP30 on cathodes containing different latices calendered to a porosity of exactly 30 %, n=3

The differences in wettability can be accounted to the interaction of the latices with the electrolyte. Latex 2 and 3 both have predominantly dispersive SFE while the SFE of Latex 4 is polar for the most part. As the SFE of LP30 (1:1 EC/DMC, 1 M LiPF$_6$) is almost solely dispersive, lower contact angles, i.e. better wettability is to be expected with Latex 2 and 3 than with Latex 4. It seems plausible that the differences in residual water retention might also influence the polarity of the electrode and therefore the wettability by the electrolyte. Yet, Davoodabadi et al. [171] demonstrated that the effect of residual water on the SFE of cathodes is negligible compared to the influence of different binders. Interestingly, cathodes that underwent a corona treatment after calandering at a watt density of 25.5 J/cm², generally improved with respect to wettability. The initial contact angles of all cathodes are drastically reduced to about 11°. After 1.3 s the contact angles reach values below 1.4° which are not properly detectable by the measuring setup. The treatment can be used to equalize the surfaces of the cathodes, as evidenced in Table 13, by the almost identical SFE values of the different cathodes after corona treatment. This further translates to the diminishment of the aforementioned latex-dependent differences in wettability and a uniform wetting behavior of the electrolyte.

Table 13 - Surface free energy of different cathodes calculated from contact angle measurements with DIM, DMSO and EG

Sample	γ_s	γ_s^d	γ_s^p
	(mJ/m²)		
Latex 2	64.1 ± 2.0	46.4 ± 0.6	17.7 ± 1.4
Latex 3	68.6 ± 1.7	48.3 ± 0.6	20.3 ± 1.1
Latex 4	69.1 ± 1.1	45.4 ± 0.5	23.7 ± 0.6
Latex 2$_{Corona}$	79.8 ± 0.9	49.2 ± 0.5	30.6 ± 0.4
Latex 3$_{Corona}$	80.2 ± 1.5	49.9 ± 0.9	30.3 ± 0.6
Latex 4$_{Corona}$	80.6 ± 1.1	50.2 ± 0.7	30.4 ± 0.4

Water Retention

All latices investigated in this work have the same PVDF backbone. The differences in surface free energy can therefore be accounted to their distinctive functionalizations, which cannot be disclosed in this work. With regard to the increased surface polarity of the different latices, the capability for water retention in electrodes was investigated by Karl-Fischer titration and the results are depicted in Figure 32. An NMP-based PVDF cathode was tested as a reference. While the organic solvent-based reference only contained around 140 ppm of water, the water-based cathodes all withheld considerable amounts of residual water ranging from 906 up to 1168 ppm after 4 hours of vacuum drying at 110 °C. The measurement further revealed a correlation between the binder's polarity and the amount of retained water after drying. This result can be explained by the free energy of hydration $\Delta G_{1\text{-}H_2O}$, between a condensed phase material 1 and water H_2O, which can be calculated according to equations 23 and 21. Starting with Latex 1 the values for $\Delta G_{Latex\text{-}H_2O}$ become increasingly more negative towards Latex 4 ($\Delta G_{Latex\ 1\text{-}H_2O}$ = -86.1 mJ/m², $\Delta G_{Latex\ 2\text{-}H_2O}$ = -94.8 mJ/m², $\Delta G_{Latex\ 3\text{-}H_2O}$ = -103.8 mJ/m² and $\Delta G_{Latex\ 4\text{-}H_2O}$ = -124.5 mJ/m²), indicating a progressively higher degree of hydrophilicity and hydration. [63] Now looking at the work of adhesion, which is the inverse of the free energy of adhesion or hydration, e.g. the energy needed to separate an interface, it becomes apparent that when subjecting the latices to the same amount of energy during drying, Latex 4 will retain a larger amount of water since more energy is needed to separate the hydration layer from the surface of the particles than it is for Latex 1. It has to be noted that the differences in the water retention behavior of the latices only become apparent when there is no large excess of energy input during drying as demonstrated with the 48 h drying procedure.

It is well described in literature that residual water is detrimental to both rate capability and long-term cycling performance of LIBs as it causes a multitude of unfavorable side reactions with the electrolyte as well as the cathode and anode. [119,120,132,168,172–180] Therefore, all cathodes were dried extensively for 24 h under vacuum at 110 °C and subsequently another 24 h under vacuum at room temperature. Following the extended drying protocol, the residual water content in all water-

based cathodes decreased significantly to concentrations between 110 and 120 ppm, which is in the range of the organic solvent-based reference. Regarding the NMP reference, the extended drying did not lead to a further reduction of the water content which remained constant at 137 ppm.
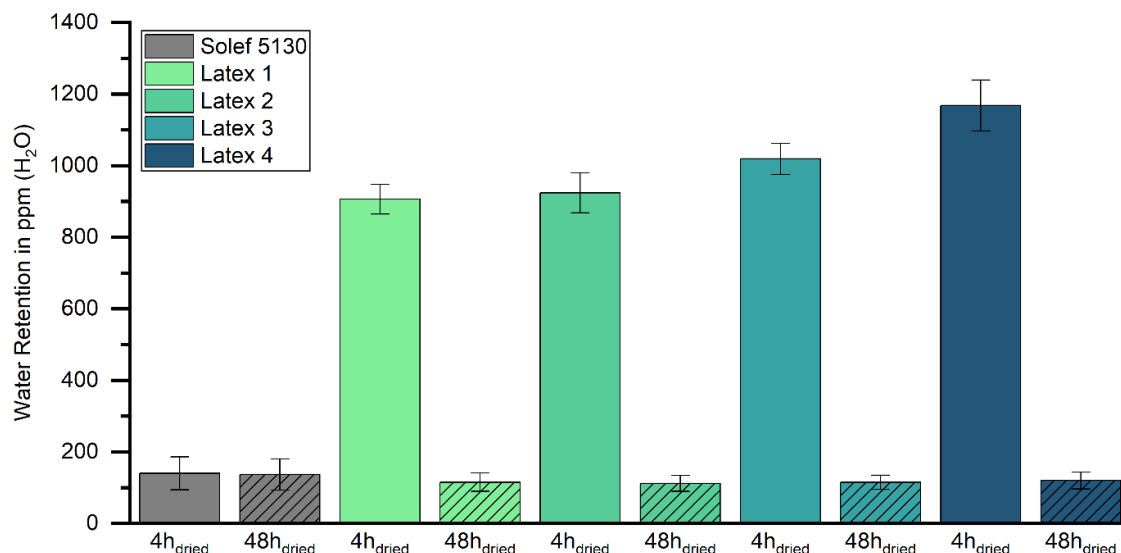
Figure 32 - Water Retention of an NMP-based cathode in comparison to aqueously processed cathodes after drying for 4 h at 110 °C under vacuum and drying for 24 h at 110 °C under vacuum plus 24 h under vacuum at RT with standard deviation, n=3, adapted from Weber and Keim et al. [64]

Electrochemical Characterization

The rate capability of the electrodes is depicted in Figure 33. Due to its low mechanical integrity it was not possible to prepare the electrode containing Latex 1 as it repeatedly peeled off the current collector during cell assembly. Rate capability tests showed that the cathodes dried for 4 h outperformed the extensively dried cathodes at every C-rate. Latex 2 yielded the highest capacities, followed by Latex 3 and Latex 4 which is in good correlation with both interface resistance and bulk resistivity, showing that higher electric resistivity leads to worse C-rate performance. The slightly decreased rate capability of the extensively dried cathodes can also be accounted to the increased electrical resistivity which results from the drying and additional wetting of the cathode components by the insulating PVDF, illustrated in Figure 30. [154] The rate performance of the corona treated electrodes is highly similar to the untreated electrodes at all C-rates up to 2 C. At 5 C the specific discharge capacity of the treated cathodes, especially Latex 2 - 4h$_{\text{dried Corona}}$ and Latex 3 - 4h$_{\text{dried Corona}}$, exceeds the respective untreated cathode significantly by 5 - 10 mAh/g. It was demonstrated by Frankenberger et al. [181] that corona treatment of the cathode can lead to an enhanced rate capability through the decrease of surface and charge transfer resistance. With regard to the findings on the improved adsorption rate of the electrolyte it is argued that the improved wetting of the electrolyte leads to a lower lithium-ion charge transfer resistance at the electrode/electrolyte interface and consequently a higher specific discharge capacity. It is further important to mention that the differences between the untreated and treated electrodes might be partially overshadowed by the excessive amount of electrolyte

(200 µL) used in the coin cell setup and might be more pronounced in pouch cells with significantly less electrolyte per electrode surface area.
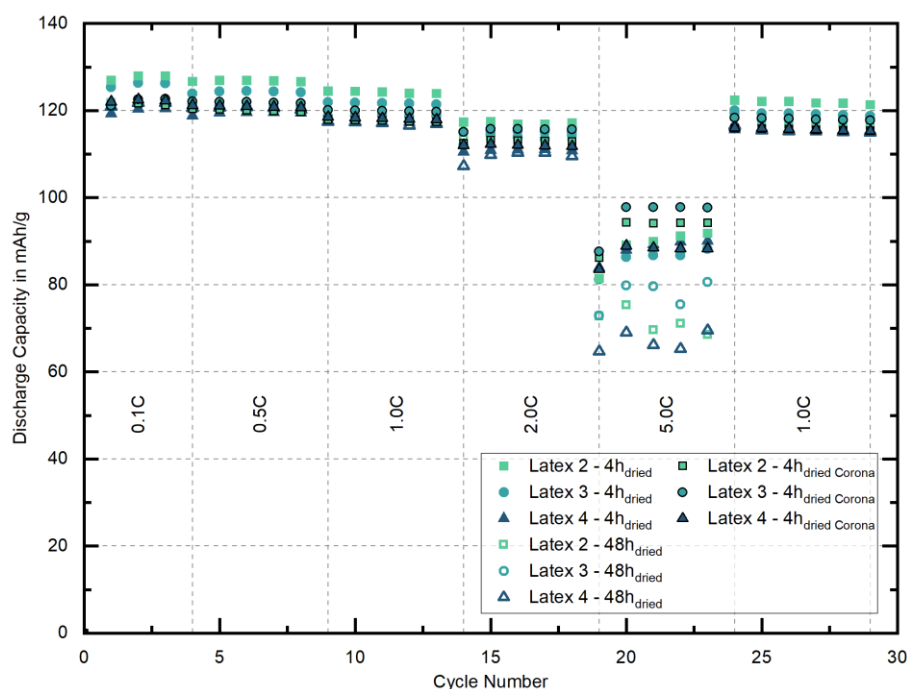
Figure 33 - Rate capability test of electrodes containing different PVDF latices dried for 4 h at 110 °C under vacuum and dried for 24 h at 110 °C under vacuum plus 24 h under vacuum at RT, n=3, adapted from Weber and Keim et al. [64]

Figure 34 shows the long-term capacity retention of the tested cathodes. It is reported in literature that extensive drying of the cathode can lead to rapid capacity decay. Huttner et al. linked the inferior electrochemical performance of long-term dried electrodes to the embrittlement of the binder in use and the damaging of the electric percolation pathways. [182] In this work, however, employing a combination of CMC and PVDF latex, it becomes clear that the degradation of the cathodes dried for 4 h is far more pronounced than for the longer dried cathodes. Latex 4, retaining the highest amount of water, only achieved 52.6 % capacity retention over 1000 cycles. Latex 3, holding the second most yielded 55.7 % and the cathode containing the least amount of residual water, Latex 2, completed 1000 cycles at 61.2 % of its initial capacity. Through extensive drying all cathodes exhibited a lesser degree of degradation. Latex 2 retained 65.9 % capacity. Latex 3 and Latex 4 even outperformed Latex 2 with 69.5 % and 69.4 %, respectively.

Besides the improved capacity retention of all cathodes dried for 48 h it is interesting to note that the cathodes dried for 4 h displayed a large standard deviation between the tested cells. Yet, the standard deviation reduced significantly after drying the cathodes for 48 h. This also indicates the reduction of unwanted parasitic side reactions due to residual water.
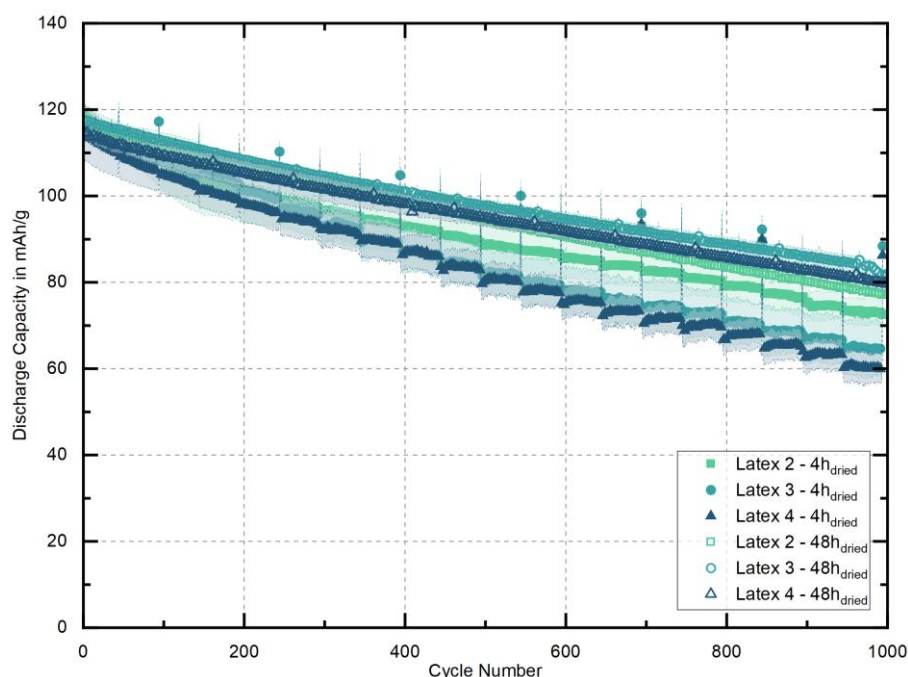
Figure 34 - Long-term capacity retention of electrodes containing different PVDF latices dried for 4 h at 110 °C under vacuum and dried for 24 h at 110 °C under vacuum plus 24 h under vacuum at RT, n=3, adapted from Weber and Keim et al. [64]

Post-mortem EDS analysis of the anodes revealed differences in SEI formation of the cycled anodes. The elemental mappings of selected elements are summarized in Table 14. To factor in residual glass fibers (SiO_2) from the separator which were stuck to the surface of the post-mortem anode samples, the values for oxygen were adjusted by subtracting a 2:1 atomic-% ratio of oxygen to silicon. EDS analysis also showed some form of sodium and borate containing precipitate on all samples. With the exact stoichiometry being unknown and the amount of borate being almost identical in all samples, the amount of oxygen listed in Table 14 was not further adjusted. However, it has to be mentioned that oxygen might therefore be overvalued. With focus on oxygen, fluorine, phosphorus, manganese and nickel, since they are frequently listed in literature as parts of degradation products, an increase in the amount of all elements, except nickel, can be seen from Latex 2 towards Latex 4. [119,120,122,132,172–174,179,180,183] This indicates SEI formation of the anodes dried for 4 h in dependence of the concentration of residual water which is in good correlation with the degradation of the full cells.

Table 14 - Elemental mappings of post-mortem anodes analyzed by EDS

Element	Latex 2 - 4h$_{dried}$	Latex 3 - 4h$_{dried}$	Latex 4 - 4h$_{dried}$
	(atomic-%)		
C	76.1	69.1	59.1
O	15.1	21.1	26.2
B	3.5	3.4	3.5
F	2.7	2.7	4.3
P	1.5	1.7	2.5
Mn	0.2	0.3	0.6
Ni	0.0	0.0	0.0

For better visualization of the differences in SEI formation the layered electron images of carbon (red) and oxygen (green) are compiled in Figure 35. It becomes apparent that the graphite anode cycled against the cathode containing Latex 2 has the least amount of SEI formed as it appears mostly red due to the strong carbon signal of the uncovered graphite. Looking at Latex 3 and Latex 4 the layered electron images become increasingly greener, indicating stronger oxygen signals, which stem from thicker oxygen containing SEI.
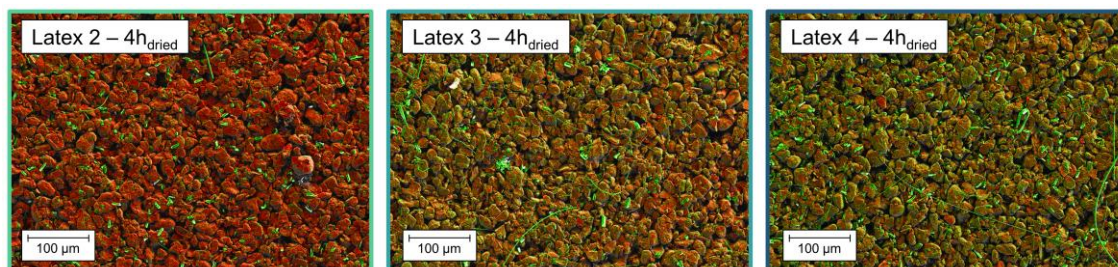
Figure 35 - Layered electron images of carbon (red) and oxygen (green) performed on anodes after long-term capacity retention tests of 1000 cycles, reproduced from Weber and Keim et al. [64]

Various authors have shown that any amount of residual water will trigger a chain of reactions leading to the formation of HF, the decomposition of the electrolyte and ultimately the loss of active Li$^+$. [119,120,132,173,174,179] Residual water will react with unstable, highly reactive P-F bonds of the electrolyte salt LiPF$_6$ resulting in its hydrolysis according to: [119,132,172,173,177,180,183]

$$LiPF_6 + H_2O \rightarrow POF_3 + LiF + 2HF \qquad (36)$$

$$PF_5 + H2O \rightarrow POF_3 + 2HF \qquad (37)$$

$$OPF_3 + 3H_2O \rightarrow PO_4H_3 + 3HF \qquad (38)$$
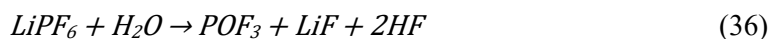
Moreover, the resulting HF is known to intensify the transition metal dissolution in LNMO because it increases the acid-driven disproportionation of $2Mn^{3+} \rightarrow Mn^{2+} + Mn^{4+}$. [120,132,168,179] The disproportionation is then followed by the reaction proposed by Aurbach et al.: [168]

$$4LiNi_{0.5}Mn_{1.5}O_4 + 8H^+ \ (from \ HF)$$
$$\rightarrow \tag{39}$$
$$2\lambda\text{-}MnO_2 + Mn^{2+} + Ni^{2+} + 4Li^+ + 4H_2O + 2Ni_{0.5}Mn_{1.5}O_4$$
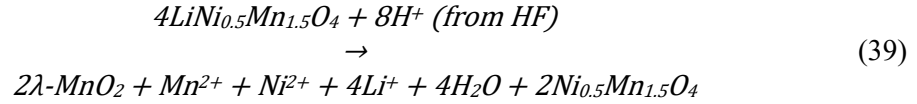
This is in good agreement with the findings on transition metal dissolution in the presence of acidic species in chapter 5.1. Mn^{2+} ions, soluble in the electrolyte, then cross over to the graphite anode causing the partial depletion of active Li^+ according to: [132]

$$Mn^{2+} + 2LiC_6 \rightarrow Mn + 2Li^+ + graphite \tag{40}$$
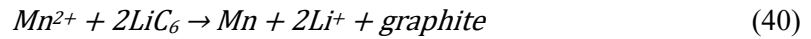
Metallic manganese further leads to the continuous growth of the SEI under decomposition of electrolyte and consumption of active Li^+. [132] Since EDS analysis shows no trace amounts of Ni incorporated into the SEI but both literature and the findings in chapter 5.2 indicate Ni dissolution in the presence of acidic species it is argued that Ni is directly incorporated into the cathode electrolyte interface. [132]

Both LiBOB and TMSP are used as electrolyte additives as they are known in literature to drastically improve long-term capacity retention by suppressing the aforementioned reactions. [119,120,122,174,184] Yet, it is argued that the concentrations of residual water in the cathodes dried for 4 h, as given in Figure 32, is too high to be compensated by the amount of TMSP and LiBOB in the electrolyte.

All cathodes dried for 48 h exhibit substantially smaller amounts of Mn incorporated into the SEI than electrodes dried for 4 h. It can therefore be concluded that the extensive drying of the cathodes for 24 h at 110 °C under vacuum and additional 24 h under vacuum at room temperature leads to a less pronounced SEI due to reduced HF formation which translates into prolonged cycle life of the manufactured cells. [132,168]

6.2.3 Conclusion

It has been found that the interaction of constituents inside aqueous slurries is dependent upon the surface free energy of the applied PVDF latex binder. Latices, showing a predominantly dispersive SFE, resulted in cathodes with low interface resistivities and bulk resistances due to the high affinity towards C65. This, however, caused low mechanical integrity of the electrode to a point where electrode preparation for cell assembly became impossible as there are insufficient free polymer domains adhering to less affine surfaces like the LNMO. With increasing polar component of the latex, free energy of adhesion calculations revealed a more equally pronounced affinity of the latex towards all slurry components which was supported by a rise in adhesion strength as well as in interface resistivity and bulk resistance as the insulating latex particles are homogeneously distributed throughout the electrode. Using the measured SFEs, the free energy of hydration of the latices was calculated showing a correlation between the polarity of the binder and its hydrophilicity. Through Karl-Fischer-Titration it was determined that the same amount of energy input during drying leads to more residual water retained in the cathodes in dependence of the latices' polarity. The differences in the amounts of retained water translated into the long-term capacity retention of the cells as more water resulted in more pronounced SEI formation and therefore more active Li$^+$ loss. It was further shown that the water uptake of the latices is reversible when drying the cathodes extensively and that the residual water content in aqueously processed cathodes can reach concentrations comparable to NMP-based cathodes. Moreover, differences in long-term capacity retention diminished after the extended drying procedure. This demonstrates that PVDF latex binders with high polarity offer enhanced adhesion strength over predominantly dispersive latices, however, they rely on higher energy input during drying to remove the hydration layer of the latex particles and achieve comparable cycling performance.

6.3 Influence of the Current Collector

The following chapter focuses on the influence of the aluminum current collector on the electrode properties. The influence of varying SFE of the CC is investigated by adjusting it through Corona treatment at different watt densities. To gain further insights into the interaction of polymer binders with the current collector, several water-soluble binders are chosen for their distinctive SFE ranging from a low polarity to a polarity of approx. 50 %. In contrast to the previous chapters, the investigation is limited to a single binder per electrode as to simplify the system under investigation.

6.3.1 Experimental

Materials

Table 15 - Materials - influence of the current collector

Reference	Name	Manufacturer
LNMO	TBM-129	Haldor Topsoe, Denmark
C65	C-NERGY Super C65	Imerys Graphite & Carbon, Switzerland
PVP	Polyvinylpyrrolidone M$_w$ ~1.300.000	Sigma-Aldrich, USA
ALG	Sodium alginate Viscarin 41 FF	IFF, USA
CMC 1	Walocel CRT 2000 PA 07	DuPont, USA
CMC 2	Texturecel™, experimental	IFF, USA
Aluminum Foil	Batte-Foil-0004W	Pi-Kem, UK

Electrode Manufacturing

Table 16 - Cathode properties - influence of the current collector

Reference	LNMO	Binder	C65	Areal capacity
		(wt%)		(mAh/cm²)
PVP	94	3	3	1.72
ALG	94	3	3	1.66
CMC 1	94	3	3	1.60
CMC 2	94	3	3	1.69

Surface Free Energy

All of the samples were measured using the Sessile Drop method (DSA30, Kruess Scientific, Germany) as they either already had a closed surface or allowed the manufacturing of a sample with no porosity. The measurement of differently treated aluminum foils was performed on 14 mm circular punch-outs. For the binder samples stock solutions containing 5 wt% of the respective binders, were prepared by disc agitation (Dispermat CA60, VMA Getzmann, Germany) and subsequently coated with a thickness of approximately 20 µm onto glass substrates. To test the wettability of the aqueous slurries on the differently treated current collectors, slurries with compositions according to Table 16 were prepared and diluted with deionized water to 50 wt% solid content.

Adhesion Strength Testing

Measurements were conducted after calendering at 50 °C to a porosity of 30 % (GKL200, Saueressig, Germany).

Corona Treatment

The aluminum current collector was treated at watt densities of 0.75 J/cm², 1.5 J/cm², and 3.0 J/cm² in-line directly before coating. For further investigations, the aluminum foil was also subjected to higher watt densities of 8.5 J/cm², 17.0 J/cm², and 25.5 J/cm².

6.3.2 Results and Discussion

Wetting Behavior

Different slurries, each containing one of the listed binders with a solid content of 50 wt% are applied onto differently treated CCs according to the sessile drop method. The images obtained through the DSA are summarized in Figure 36. The initial contact angles of the slurry on the as-received aluminum foil are 83.7 ° for PVP, 81.1 ° for ALG, 79.9 ° for CMC 1 and 94.2 ° for CMC 2. All slurries exhibit significantly smaller contact angles (29.7 ° for PVP, 36.1 ° for ALG, 38.1 ° for CMC 1 and 53.4 ° for CMC 2) with the CC already after low-intensity corona treatment of 0.75 J/cm². A continuous increase in watt density to 3.0 J/cm² leads to an additional decrease of the contact angle or better wetting (14.6 ° for PVP, 30.8 ° for ALG, 30.3 ° for CMC 1 and 42.2 ° for CMC 2) which is in line with other findings in literature. [153,185,186] Extensive treatment of the aluminum at watt densities beyond 3.0 J/cm² up to 25.5 J/cm² does not yield any further improvement of the wetting behavior.
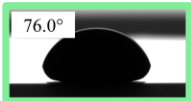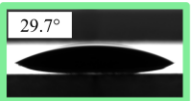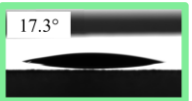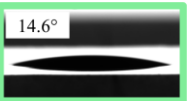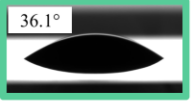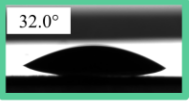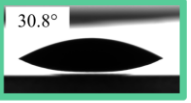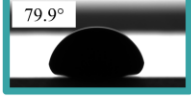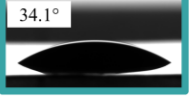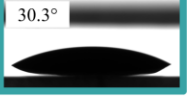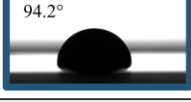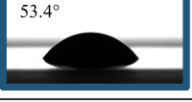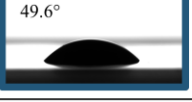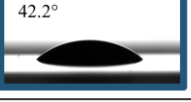
Slurry Sample	Current Collector Treatment			
	0 J/cm²	0.75 J/cm²	1.5 J/cm²	3.0 J/cm²
PVP	76.0°	29.7°	17.3°	14.6°
ALG	81.1°	36.1°	32.0°	30.8°
CMC 1	79.9°	38.1°	34.1°	30.3°
CMC 2	94.2°	53.4°	49.6°	42.2°

Figure 36 - Contact angles of slurries containing different polymeric binders with a solid content of 50 wt% on corona treated aluminum current collectors

Mechanical Properties

The results obtained from the 90° peel tests, illustrated in Figure 37, show the highest adhesion of PVP of 18.4 N/m with the as-received CC. Adhesion strength values of the cathodes containing PVP with the aluminum foil treated with 0.75 J/cm² to 3.0 J/cm² reveal a declining trend to 13.4 N/m over 13.5 N/m to 10.9 N/m. ALG coated on the CC treated with 0.75 J/cm² exhibits an initial rise in adhesion strength to 77.0 N/m over the untreated CC with 73.9 N/m. It is followed by a deterioration of the adhesive strength to 69.4 N/m when coated onto the aluminum foil at 1.5 J/cm² and an even further decline to 58.9 N/m in combination with the CC treated with 3.0 J/cm². The same trend can be observed for both CMC 1 and CMC 2.
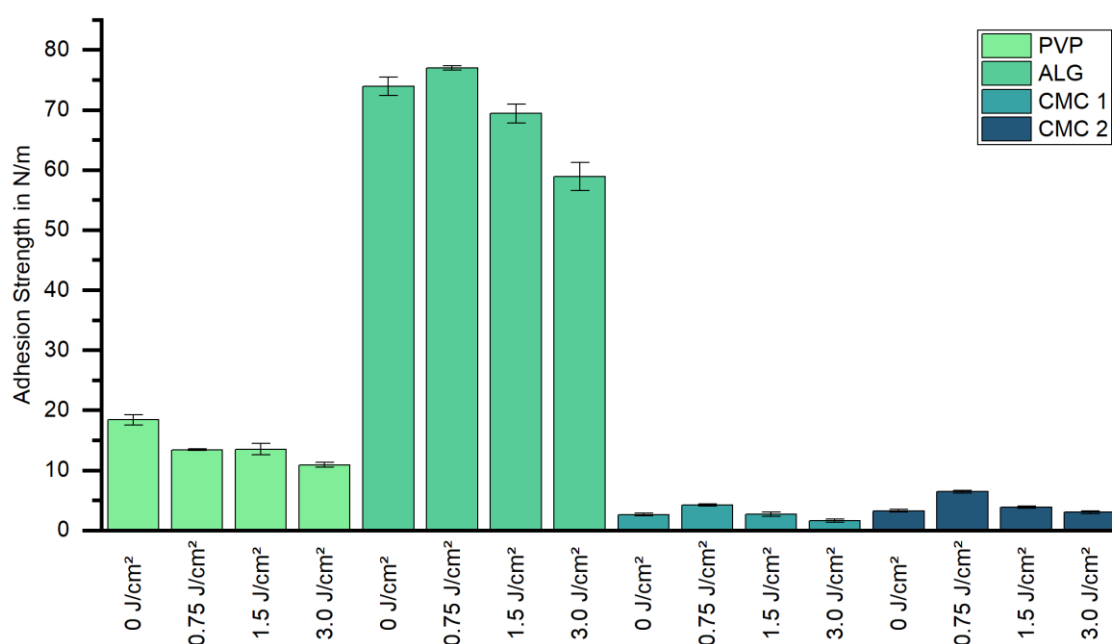
Figure 37 - Adhesion strength of cathodes containing solved binders on different corona treated aluminum current collectors with standard deviation, n=3

The same effect of the corona treatment on the adhesion strength can be observed throughout all the applied polymer binders. However, a comparison between the absolute adhesion strengths of the different binders would be misleading since the differences in adhesion strength far exceed the treatment of the CC. The total mechanical integrity of a binder relies on several factors such as its ability to cross-link [24], its SFE [154] (resulting from functionalization [187] and the number of substituents [188]), its molecular weight [189], or its elastic modulus [190].

Surface Free Energy

The results of the contact angle measurements of various water-soluble binders with DIM, EG and water are listed in Table A 3. By application of the OWRK model the binders' surface free energies are calculated from the measured contact angles. SFE values of the different water-soluble, polymeric binders and differently treated aluminum current collectors are given in Table 17 with γ_S denoting the overall SFE of the sample and γ_S^d and γ_S^p designating the dispersive and polar components, respectively.

Table 17 - Surface free energy of different water-soluble binders and corona-treated current collectors calculated from contact angles with DIM, EG, DMSO and water according to the OWRK method

Solid sample	γ_S	γ_S^d	γ_S^p	Polarity
	(mJ/m²)			(%)
PVP	45.6 ± 0.5	44.9 ± 0.4	0.7 ± 0.1	1.5
ALG	37.6 ± 1.2	28.8 ± 0.2	8.8 ± 0.1	23.4
CMC 1	47.3 ± 1.5	38.5 ± 1.2	8.8 ± 0.4	18.6
CMC 2	44.7 ± 1.6	23.5 ± 0.8	21.2 ± 0.8	47.4
Alu 0 J/cm²	35.5 ± 1.5	32.7 ± 1.3	2.8 ± 0.2	7.9
Alu 0.75 J/cm²	47.8 ± 2.2	37.2 ± 1.9	10.5 ± 0.3	22.2
Alu 1.5 J/cm²	58.2 ± 2.9	35.8 ± 2.5	22.4 ± 0.4	38.5
Alu 3.0 J/cm²	63.5 ± 3.2	35.7 ± 2.7	27.8 ± 0.5	43.8
Alu 8.5 J/cm²	63.8 ± 2.7	32.5 ± 2.3	31.3 ± 0.4	49.1
Alu 17.0 J/cm²	63.8 ± 2.7	32.4 ± 2.3	31.5 ± 0.4	49.4
Alu 25.5 J/cm²	64.4 ± 2.8	32.9 ± 2.4	31.6 ± 0.4	49.1

Surface free energy calculations for the binders showed similar γ_S values around 45 - 47 mJ/m² for all binders except ALG which exhibited a lower overall SFE of 37.6 mJ/m². Nonetheless, the polar component and the consequential percentage of surface polarity vastly differed between the polymers, with values between 1.5 % surface polarity for PVP to 47.4 % for CMC 2. Regarding the CC the untreated aluminum exhibited almost purely dispersive SFE of 32.7 mJ/m² and a small polar component of 2.8 mJ/m². Corona treatment with 0.75 J/cm² leads to a rise of the polar component to 10.6 mJ/m² and a slight increase of the dispersive part to 37.2 mJ/m². By increasing the watt density, the polar component continuously rises to 27.8 mJ/m² for the CC treated with 3.0 J/cm² while the dispersive part remains unchanged within the standard deviation. Consequently, the overall SFE of the aluminum foil and the polarity grow from 35.5mJ/m² to 63.5 mJ/m² and from 7.9 % to 43.8 %, respectively, with higher intensity of the treatment. As mentioned above an increased intensity of the corona treatment beyond 3.0 J/cm² does not result in an improvement in wettability over the CC treated at low intensity. This can also be anticipated through the calculated SFE as treating the CC with 8.5 J/cm² only results in a slight further rise of the polar component to 31.3 mJ/m² and corona discharge with 17.0 J/cm² (γ_S^p = 31.5 mJ/m²) or 25.5 J/cm² (γ_S^p = 31.6 mJ/m²) leads to marginal differences in the polar part as well as overall SFE which remains constant around 64 mJ/m². This plateau indicates the saturation in polar groups on the surface of the foil. [55]

Going forward, the obtained SFE values are used to calculate the free energies of adhesion between two materials submerged in a liquid according to equations 21 and 25. The free energy

of adhesion between the individual binder and the CCs as if they were in direct contact and the free energy of hydration between the CCs and water are also given. The resulting values are compiled in Table 18.

Table 18 - Free energy of adhesion of current collector with different polymer binders while submerged in water (ΔG^{IF}_{132} annotated as $\Delta G^{IF}_{S-H2O-Binder}$ with 1 representing the current collector, 3 the immersion liquid H$_2$O and 2 the respective polymer binder)

Solid sample	ΔG^{IF} S-H2O-PVP	ΔG^{IF} S-H2O-ALG	ΔG^{IF} S-H2O-CMC 1	ΔG^{IF} S-H2O-CMC 2
	(mJ/m²)			
Alu 0 J/cm²	-73.3 ± 0.9	-47.2 ± 0.5	-49.0 ± 0.8	-24.9 ± 0.9
Alu 0.75 J/cm²	-55.0 ± 0.3	-34.6 ± 0.2	-37.0 ± 0.2	-17.7 ± 0.5
Alu 1.5 J/cm²	-35.6 ± 0.1	-21.9 ± 0.1	-24.1 ± 0.1	-10.8 ± 0.4
Alu 3.0 J/cm²	-28.8 ± 0.1	-17.4 ± 0.1	-19.6 ± 0.2	-8.4 ± 0.3

The obtained ΔG^{IF} values of the different binders with the untreated aluminum foil, while submerged in water, range from -73.3 mJ/m² for PVP over approx. 47 - 49.0 mJ/m² for ALG and CMC 1 to -24.9 mJ/m² for CMC 2. This indicates the highest affinity of the mostly dispersive untreated CC with the almost purely dispersive PVP and the lowest affinity with CMC 2 with a polarity of 47.4 %. However, regardless of the binder's polarity, the values of ΔG^{IF} become less negative the more intense the corona treatment or rather the larger the polar contribution of the current collector's surface becomes, which points to lesser affinity between the individual binder and CC.

Going back to the contact angles of the slurries on the CC the calculated ΔG^{IF} values also explain the differences in wettability. The more energetically favorable the formation of an interface, the smaller the resulting contact angle and consequently the larger the resulting interface area will be. The general decrease of the contact angle is accounted to the interaction between the solvent water and the CC as ΔG^{IF}_{S-H2O} becomes increasingly more negative from -77.2 mJ/m² for 0 J/cm² to -131.1 mJ/m² for 3.0 J/cm² showing a heightened affinity of water towards the corona treated CCs. While the determining factor in the wetting behavior of the slurry might be the solvent it is also clearly visible from Figure 36 that the applied binder does have an impact on the contact angle formed between CC and slurry. Comparing $\Delta G^{IF}_{S-H2O-Binder}$ of the different polymers the most energy is released during the interface formation between the CC and PVP, followed by ALG and CMC 1 and lastly CMC 2. This directly translates into the PVP slurry having the lowest contact angle or best wettability followed by ALG and CMC 1, and CMC 2 having the highest contact angle.

The interface resistance of the cathodes, depicted in Figure 38, is in good correlation with the adhesion strength, analogical to the findings in chapters 6.1.2 and 6.2.2. Regarding PVP, the interface resistance is highest with the untreated CC and continuously decreases with respect to the treatment intensity. ALG, CMC 1 and CMC 2 exhibit a rise in interface resistance from

0 J/cm² to 3.0 J/cm². With higher intensity of the corona treatment interface resistance drops similar to PVP. This indicates less binder deposition on the CC with intensified treatment for all binders. The rise in adhesion strength and interface resistance of ALG, CMC 1 and CMC 2 from 0 J/cm² to 0.75 J/cm² is not indicated by the calculated ΔG^{IF}. This might be due to the fact that the measurement of the untreated, as-received CC also represents various adsorbed organic and inorganic contaminants frequently found on aluminum foils stemming from the manufacturing process, e.g. rolling oil, which can act as release agents between CC and coating. Therefore, 0.75 J/cm² outperforms 0 J/cm² regarding adhesion strength as it initially cleans the CC. [55,105,191]
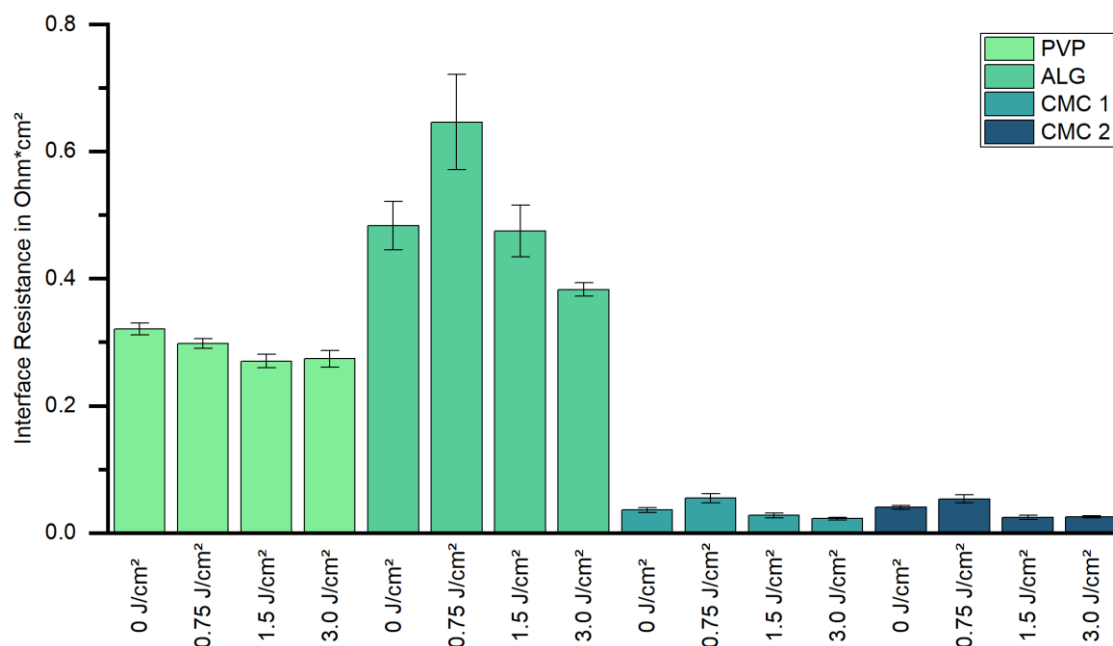
Figure 38 - Interface resistance of the cathodes coated on differently corona treated alumnium current collectors with standard deviation, n=5

It seems counterintuitive at first that higher intensity of the corona treatment leads to lesser affinity between binder and CC, since the surface modification of the CC through corona treatment leads to an improved wetting of the aluminum by all of the aqueous slurries, as depicted in Figure 36. In other applications, e.g. adhesive bonding of wood or metal [192,193] or coating of polymers [194], the improved wettability and higher surface free energy of the substrate after corona discharge is usually accompanied by a higher adhesion strength of the bond. It has to be kept in mind, however, that most joining or coating applications are two- or three-component systems where the binding agent's only possible binding partner is the substrate. Electrodes on the other hand are multi-component systems where changing the surface energy of one constituent does not only alter the interaction between two components but the interactions of all. While the free energy of adhesion of the binder towards the other materials in the slurry remains unchanged, ΔG^{IF} of the binder and the CC continuously decreases with respect to the intensity of the corona treatment. This is due to the binder increasingly competing with the water in the slurry for the wetting of the aluminum surface as the aluminum surface becomes more compatible with water the more intense the corona treatment becomes. The binder may then form interfaces with other particles in the slurry as the surface of the aluminum foil is occupied by the solvent. [195] Jaiser et al. [196] demonstrated that the

solvent occupies the substrate until full depletion of the pores is achieved. At this point, the distribution of the binder is set and redisposition of the binder towards the CC is no longer possible, ultimately resulting in less binder deposited on the current collector of corona treated aluminum. Owens [197] further demonstrated that if the presence of a liquid results in a positive free energy of adhesion, i.e. repulsion, between coating and substrate it can even result in the spontaneous separation of the coating due to displacement by the liquid. To clarify further, $\Delta G^{IF}_{S\text{-Binder}}$ which represents the free energy of interaction between CC and binder as if they were in direct contact with each other in the absence of a solvent was also compiled in Table 18. Here it can be seen that corona treatment of the current collector would be expected to have a positive effect on both affinity and adhesion strength of the binder-aluminum interface since $\Delta G^{IF}_{S\text{-Binder}}$ becomes more negative with higher intensity of the corona treatment. However, in aqueous processing of cathodes this case does not apply due to the presence of the solvent.

Table 19 - Free energy of adhesion of current collector with different polymer binders or water in direct contact (ΔG^{IF}_{12} annotated as $\Delta G^{IF}_{S\text{-Binder/H2O}}$ with 1 representing the current collector and 2 the respective polymer binder or water)

Solid sample	$\Delta G^{IF}_{S\text{-PVP}}$	$\Delta G^{IF}_{S\text{-ALG}}$	$\Delta G^{IF}_{S\text{-CMC 1}}$	$\Delta G^{IF}_{S\text{-CMC 2}}$	$\Delta G^{IF}_{S\text{-H2O}}$
	(mJ/m²)				
Alu 0 J/cm²	-79.5 ± 2.2	-71.3 ± 2.0	-80.8 ± 2.6	-77.6 ± 1.3	-77.2 ± 2.0
Alu 0.75 J/cm²	-87.2 ± 2.9	-84.7 ± 2.3	-94.9 ± 3.9	-87.6 ± 3.5	-103.2 ± 2.1
Alu 1.5 J/cm²	-88.1 ± 3.8	-92.3 ± 2.7	-102.3 ± 4.6	-101.0 ± 4.0	-123.5 ± 2.6
Alu 3.0 J/cm²	-89.0 ± 4.2	-95.4 ± 3.1	-105.4 ± 4.9	-106.1 ± 4.3	-131.1 ± 2.8

6.3.3 Conclusion

Four water-soluble polymeric binders exhibiting different distributions of polar and dispersive SFE were tested in combination with corona treated aluminum current collectors. It was found that wetting of aqueous slurries improves with increasing intensity of the corona treatment. The improvement of the wettability e.g. the reduction of the contact angle ranged from 50° to 60°. Through contact angle measurements the main influence on the improvement could be accounted to the enhanced interaction between the solvent in the slurry and the current collector. Nonetheless, the differences in SFE between the binders resulted in distinctive slurry contact angles with the highest affinity of binder towards the aluminum resulting in the lowest contact angle. Concerning the adhesion strength of the cathodes, only low intensity treatment was found to have a favorable effect for three of the four tested binders. This is argued to be due to the removal of residual contaminants on the CC. Free energy of adhesion calculations showed that, irrespective of the applied binder, the decrease in adhesion strength is the result of the improved interaction between water and the treated CC. To summarize, when aiming at improving the wetting behavior of the slurry during coating, high intensity corona treatment of the current collector is beneficial. However, when increasing the adhesion strength of the composite electrode towards the aluminum is the objective, only cleaning of the CC by low intensity treatment is advantageous as high intensities lead to the deterioration of the mechanical integrity because of the enhanced interaction of water with the current collector.

7 Manufacturing of High-Loading LiNi$_{0.5}$Mn$_{1.5}$O$_4$ Cathodes

Regarding the most prominent and one of the most demanding application of LIBs, the automotive sector, vehicle manufacturers have sought to continuously improve batteries over the last decade. The aim of optimization has been multifaceted. Some of the most sought after but difficult to achieve targets are the application of alternative manufacturing processes, such as aqueous or dry processing of cathodes [24,87,198,199] or the increase of energy density. Herein, efforts range from optimizing electrode formulation [200] over increasing the active material mass loading [201] up to completely rethinking battery design [202]. Several authors have demonstrated the application of various water-soluble polymers. [203–205] Yet, all of them reported active material loadings below 1.5 mAh/cm². This is presumably owed to insufficient mechanical integrity when notably exceeding the aforementioned loading. Only few publications report on the successful NMP-free manufacturing of high-loading LNMO cathodes. Binder et al. [198] showcased the application of carrageenan in combination with citric acid in the processing of cathodes with an active material loading of 3.9 mAh/cm² and was able to achieve a capacity retention of 75 % after 1000 cycles in full cells. Yao et al. [16] reported on the dry coating of a 3.1 mAh/cm² LNMO cathode using PTFE as the binder showing a capacity retention in full cell configuration of 60 % after 1000 cycles.

The following chapter aims to combine the findings of the foregoing investigations for the aqueous processing of a high-loading (>25.5 mg/cm² or >3.8 mAh/cm²) LNMO cathode using a mixture of PVDF latex and CMC as binding agent. While it was found that low binder content in combination with the use of VGCF is beneficial regarding tortuosity, for the manufacturing of high-loading cathodes the formulation C65/VGCF$_{1.4+1.4wt\%}$, according to chapter 6.1.1 was chosen as it promised the best trade-off between electrical resistance, tortuosity and mechanical integrity. Both Binder et al. [198] and Yao et al. [16] demonstrated the mechanical integrity of the formulation to be one of the decisive factors in successful manufacturing and cycling of high-loading LNMO cathodes. This is in good agreement with own observations as it was not possible to coat a slurry according to the C65$_{2.8wt\%}$ composition with a loading of 3.75 mAh/cm² onto an aluminum current collector as it completely peeled off while drying in a roll-to-roll coating line. Additionally, a latex with a low polar component was chosen due to the findings in chapter 6.2.2 showing that applying a binder with a low polar part of SFE will result in low electrical resistance, less residual water, and improved electrolyte uptake.

7.1 Experimental

Materials

Table 20 - Materials - high-loading cathodes

Reference	Name	Manufacturer
LNMO	TBM-129	Haldor Topsoe, Denmark
C65	C-NERGY Super C65	Imerys Graphite & Carbon, Switzerland
VGCF	VGCF-H	Resonac Corporation, Japan
CMC	Walocel CRT 2000 PA 07	DuPont, USA
PVDF Latex	Kynar®, experimental	Arkema, France

Electrode Manufacturing

Table 21 - Cathode properties - high-loading cathodes

Reference	LNMO	CMC	PVDF	CA	Areal capacity
	(wt%)				(mAh/cm²)
Low-Loading (LL)	92.6	1.8	2.8	1.4 + 1.4	1.9 ± 0.1
High-Loading (HL)	92.6	1.8	2.8	1.4 + 1.4	3.8 ± 0.1

Cell Assembly

Foregoing the assembly of the cells, the electrodes were dried at 110 °C for 4 h in a vacuum oven to evaporate residual water. Alternatively, the electrodes were dried at 110 °C for 24 h under vacuum and an additional 24 h under vacuum at room temperature.

Adhesion Strength Testing

Measurements were conducted after calendering at 50 °C (GKL200, Saueressig, Germany) and drying in a vacuum oven at 110 °C for 4 h or 24 h.

Corona Treatment

The wattage was constantly set to 900 W at a line speed of 0.2 m/min, corresponding to a watt density of 25.5 J/cm².

7.2   Results and Discussion

Electrode Properties

Selected properties of the differently prepared cathodes are compiled in Table 22. Starting with the interface resistance, LL - 4h$_{dried}$ exhibits a value of 0.30 Ω*cm². For HL - 4h$_{dried}$ a smaller resistance of 0.06 Ω*cm² is measured which increases to 0.09 Ω*cm² after drying for 24 h under vacuum at 110 °C and subsequent 24 h under vacuum at room temperature. Adhesion strength of LL - 4h$_{dried}$ exceeds that of HL - 4h$_{dried}$ by almost 2.5 times. The extensive drying step, as also demonstrated in the previous chapters, leads to an improvement in adhesion strength to 27.8 N/m. Haselrieder et al. [206] account the decrease in adhesion strength to pronounced binder migration due to longer drying times of high-loading cathodes which entails the decrease in interface resistance with less binder deposited on the current collector. Bulk resistivity remains rather constant at 1.59 Ω*cm for Low-Loading - 4h$_{dried}$ and 1.63 Ω*cm for HL - 4h$_{dried}$ with again a slight increase after drying. Tortuosity is measured to be 3.00 irrespective of the active material mass loading and is unaffected by the drying step. The findings on bulk resistivity and tortuosity align with literature, as both porperties are specific material constants independent of cathode thickness. [111,207]

Table 22 - Comparison of properties between low- and high-loading aqueously processed cathodes with standard deviation, n=3

Reference	Interface Resistance	Adhesion Strength	Bulk Resistivity	Tortuosity
	(Ω*cm²)	(N/m)	(Ω*cm)	---
LL - 4h$_{dried}$	0.30 $\pm$ 0.03	57.4 $\pm$ 1.4	1.59 $\pm$ 0.12	2.98 $\pm$ 0.07
HL - 4h$_{dried}$	0.06 $\pm$ 0.01	23.1 $\pm$ 0.8	1.63 $\pm$ 0.09	3.00 $\pm$ 0.05
HL - 4h$_{dried-Corona}$	0.06 $\pm$ 0.01	23.1 $\pm$ 0.9	1.63 $\pm$ 0.10	3.00 $\pm$ 0.05
HL - 48h$_{dried}$	0.09 $\pm$ 0.01	27.8 $\pm$ 0.6	1.72 $\pm$ 0.12	3.00 $\pm$ 0.07

As illustrated in Figure 39, the electrolyte forms an initial contact angle on HL - 4h$_{dried}$ right after drop deposition of 31.6°. The contact angle then continuously decreases down to 4° and stays constant. In contrast, HL - 4h$_{dried-Corona}$ already has a lower initial contact angle with LP30 of 27.9°. The contact angle of LP30 on HL - 4h$_{dried-Corona}$ proceeds to rapidly become smaller, reaching roughly 1.5° after 2.5 s and then stays constant throughout the remaining measurement, showing overall better wettability of the corona treated cathode. Analogous to chapter 6.2.2, corona treatment of the high-loading cathode with 25.5 J/cm² leads to improved wettability by LP30.
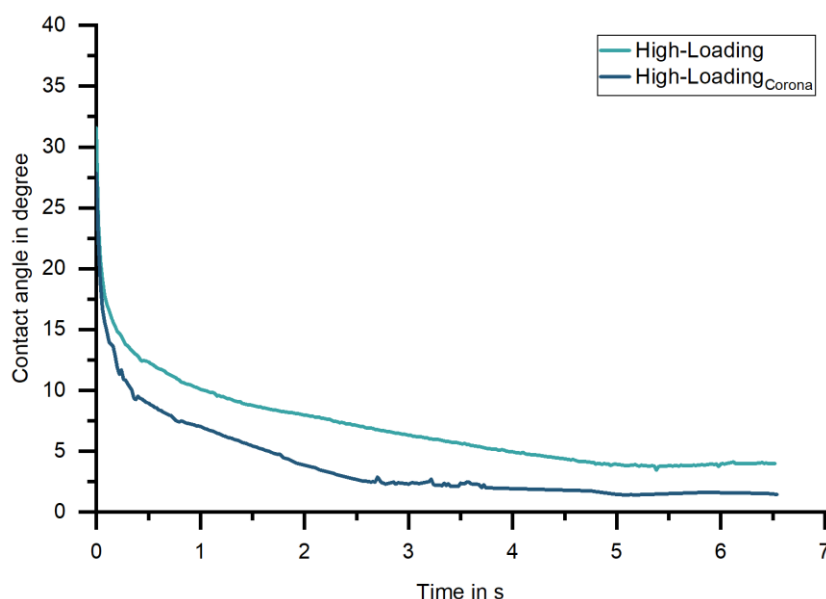
Figure 39 - Average absorption rate determined through the advancing contact angle of LP30 on untreated and corona treated high-loading cathodes calendered to a porosity of exactly 30 %, n=3

Electrochemical Characterization

Rate capability tests in full cell configuration showed that the low-loading cathode and high-loading cathode perform comparable up to 1 C. Starting at 2 C large discrepancies in discharge capacity between the the different loadings can be observed. While the low-loading cathode still delivers around 115.6 mAh/g, the high-loading cathode only yields around 96.5 mAh/g which is due to diffusion limitation as a result of the increased thickness. At a C-rate of 5 C, the differences become even more apparent with the low-loading averaging 69.8 mAh/g and the high-loading being able to access only 20.9 mAh/g. Similar to the rate capability of low-loading cathodes, as demonstrated in 6.2.2, significant improvements in rate capability can be observed when applying a 25.5 J/cm² corona treatment to the high-loading cathode. Low C-rates of 0.1 C and 0.5 C remain visibly unchanged. Starting at 1 C an improvement from 119.6 mAh/g to 122.9 mAh/g can be noted after corona treatment. The beneficial effect of the treatment becomes larger the higher the C-rate. At 2 C the discharge capacity of the high-loading cathode improves from 96.5 mAh/g to 107.4 mAh/g, at 5 C the treatment results in an even larger increase from 20.9 mAh/g to 39.5 mAh/g. Frankenberger et al. demonstrated that corona treatment of the cathode leads to a decrease of both surface and charge transfer resistance which in turn leads to an enhanced rate capability. [181] Furthermore, similar findings by Xu et al [208] showed that by enhancing wettability through a surface coating of the separator, an increase in rate capability is achieved. It is, therefore, argued that the enhanced wetting of the cathode by the electrolyte, as evidenced in Figure 39, is the responsible factor behind the improved lithium-ion charge transfer at the electrode/electrolyte interface and the superior rate capability of corona treated cathodes [181,209]
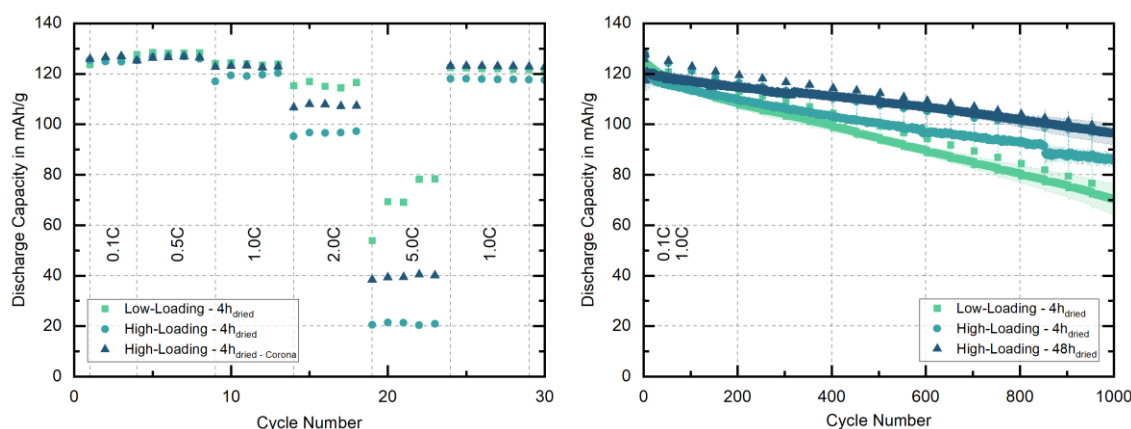
Figure 40 - Comparison of rate capability (left) and long-term cycling performance (right) between low-loading and high-loading aqueously processed cathodes in full cell configuration, n=3

Long-term capacity retention tests show, analogous to chapter 6.2.2, that extensive drying of the high-loading cathode for 48 h significantly improves the cycle life. LL - 4h$_{dried}$ achieves a capacity retention of 60.3 % over 1000 cycles. In comparison HL - 4h$_{dried}$ maintains a retention of 73.2 % while HL - 48h$_{dried}$ yields 80.3 %. The visible drop in discharge capacity of HL - 4h$_{dried}$ after approx. 850 cycles is due to a software problem of the battery cycler where the cells remained at a high voltage for a longer period of time expediting degradation. As compiled in Table 22, there are only negligible differences between the low- and high-loading cathodes regarding the main physical properties influencing capacity retention with adhesion strength even decreasing with higher loading. Concerning the electrode properties, the only significant advantage of the high-loading over the low-loading is in the interface resistivity which is arguably the reason for the higher capacity retention as it leads to less overpotential build-up during charging and discharging and therefore to a more complete process of redox reactions.

7.3 Conclusion

Through combination of the findings made throughout this work, the aqueous processing of sturdy high-loading LNMO cathodes (3.8 mAh/cm²) was demonstrated. The resulting cathodes showed good adhesion strength of 27.8 N/m, low bulk resistivity (1.72 Ω*cm) and interface resistance (0.09 Ω*cm²) as well as a moderate tortuosity of 3.00. The findings further validated previous works by other authors that resistivity and tortuosity are independent of electrode loading and thickness while adhesion strength is strongly dependent. With regard to the electrochemical performance it was found that the high-loading cathodes only achieve comparable discharge capacities to the low-loading cathodes up to C-rates of 1C. However, it was demonstrated that rate capability of high-loading cathodes at higher C-rates can be significantly improved by a corona treatment of the cathode at 900 W due to enhanced wetting by the electrolyte. Through high adhesion strength, extensive drying of the cathode as well as the application of well-known electrolyte additives, namely LiBOB and TMSP, a remarkable long-term capacity retention of 80 % after 1000 cycles was achieved.

8   Overall Conclusion

In conclusion, this study advances the methodology for producing durable, high-loading LNMO cathodes through optimized aqueous processing. By evaluating the interaction of LNMO with various aqueous environments, as well as the effects of conductive additives, PVDF latex binders, and current collector treatments, key factors that enhance both mechanical and electrochemical stability were indentified. The major findings can be summarized as follows:

1. **Impact of Submersion on LNMO:** LNMO exhibited minimal leaching when submerged in pure water, but significant lithium and transition metal leaching occurred in the presence of phosphoric acid, which restricts the use of PVDF latices due to coagulation effects. However, pure water submersion effectively removed resistive surface impurities, improving capacity retention. While acidification formed cyrstalline Li_3PO_4 species on the active material that are beneficial for stability, its negative effects on lithium and transition metal dissolution highlight limitations in using phosphoric acid for aqueous LNMO processing.

2. **Surface Free Energy - Influence of the Conductive Additive:** The study demonstrated that conductive additives with highly dispersive surface free energy significantly affect binder distribution. The binders are preferentially drawn towards the additive surface, creating pronounced carbon-binder-domains which compromise mechanical strength. Due to the particle form of the PVDF latex and its rather brittle behavior at room temperature, the mechanical integrity of the electrode greatly benefits from heat treatment above the melting temperature of the PVDF. Reducing the conductive additive's surface area or using vapor-grown carbon fibers with lower binder affinity improved both mechanical integrity and resistance to degradation at high voltage, proving effective strategies to enhance electrode stability and minimize capacity loss due to delamination.

3. **Surface Free Energy - Influence of the PVDF Latex Binder:** The polarity of PVDF latex binders impacted adhesion strength, resistance, and water retention. High-polarity binders improved uniform adhesion across all slurry components, but with increased interface and bulk resistances due to the insulating properties of latex particles. These latices also absorbed more water, leading to additional SEI formation and potential lithium loss during cycling. However, extended drying of these cathodes eliminated this drawback, indicating that high-polarity latices are suitable for enhanced adhesion if drying conditions are optimized.

4. **Surface Free Energy - Influence of the Current Collector:** Corona treatment on aluminum current collectors was found to increase aqueous slurry wettability as evidenced by reduced contact angles, particularly at high treatment intensities. However, only low-intensity treatment improved adhesion strength by removing contaminants without compromising the electrode's mechanical integrity. High-intensity corona treatment led to a deterioration of adhesion strength through strong interaction of water with the CC therefore displacing and hindering the polymer binders to effectively adhere to the CC.

5. **Manufacturing of High-Loading LNMO Cathodes:** By applying the insights gained from previous chapters, high-loading LNMO cathodes with favorable adhesion strength, resistivity, and tortuosity values were developed, performing comparably to low-loading cathodes up to a C-rate of 1 C. Through corona treatment, the cathodes demonstrated improved rate capability at high C-rates up to 5 C due to better electrolyte wetting. With an extended drying protocol and the addition of LiBOB and TMSP as electrolyte additives, the cathodes provided excellent long-term stability with 80 % capacity retention over 1000 cycles.

To conclude, the theory of surface free energy and the methods applied in this work offer great potential to create further understanding of the driving forces behind the interactions of electrode components during processing and how they affect the final electrode properties not only in aqueously processed but also organic solvent based and dry processed electrodes.

References

(1)   European Commission: Directorate-General for Mobility and Transport. *EU Transport in Figures – Statistical Pocketbook 2023*; Publications Office of the European Union, Luxembourg, **2023**. https://doi.org/10.2832/319371.

(2)   Gül, T.; Pales, A. F.; Connelly, E. *Global EV Outlook 2024 Moving towards increased affordability*. Electric Vehicles Intitiative. https://www.iea.org/reports/global-ev-outlook-2024 (accessed 2024-10-15).

(3)   Davis, S. C.; Boundy, R. G. *Transportation Energy Data Book (Edition 40)*; U.S. Department of Energy: Washington, D.C., **2022**. https://doi.org/10.2172/1878695.

(4)   Schmuch, R.; Wagner, R.; Hörpel, G.; Placke, T.; Winter, M. Performance and Cost of Materials for Lithium-Based Rechargeable Automotive Batteries. *Nat. Energy* **2018**, *3* (4), 267–278. https://doi.org/10.1038/s41560-018-0107-2.

(5)   Lestriez, B. Functions of Polymers in Composite Electrodes of Lithium Ion Batteries. *Comptes Rendus Chimie*. Elsevier Masson SAS **2010**, pp 1341–1350. https://doi.org/10.1016/j.crci.2010.01.018.

(6)   Wang, N.; NuLi, Y.; Su, S.; Yang, J.; Wang, J. Effects of Binders on the Electrochemical Performance of Rechargeable Magnesium Batteries. *J. Power Sources* **2017**, *341*, 219–229. https://doi.org/10.1016/j.jpowsour.2016.12.003.

(7)   Sung, S. H.; Kim, S.; Park, J. H.; Park, J. D.; Ahn, K. H. Role of PVDF in Rheology and Microstructure of NCM Cathode Slurries for Lithium-Ion Battery. *Materials (Basel).* **2020**, *13* (20), 1–11. https://doi.org/10.3390/ma13204544.

(8)   Bresser, D.; Buchholz, D.; Moretti, A.; Varzi, A.; Passerini, S. Alternative Binders for Sustainable Electrochemical Energy Storage-the Transition to Aqueous Electrode Processing and Bio-Derived Polymers. *Energy Environ. Sci.* **2018**, *11* (11), 3096–3127. https://doi.org/10.1039/c8ee00640g.

(9)   Liu, Y.; Zhang, R.; Wang, J.; Wang, Y. Current and Future Lithium-Ion Battery Manufacturing. *iScience*. **2021**. https://doi.org/10.1016/j.isci.2021.102332.

(10)   Kazzazi, A.; Bresser, D.; Birrozzi, A.; Von Zamory, J.; Hekmatfar, M.; Passerini, S. Comparative Analysis of Aqueous Binders for High-Energy Li-Rich NMC as a Lithium-Ion Cathode and the Impact of Adding Phosphoric Acid. *ACS Appl. Mater. Interfaces* **2018**, *10* (20), 17214–17222. https://doi.org/10.1021/acsami.8b03657.

(11)   Schuer, A. R.; Kuenzel, M.; Yang, S.; Kosfeld, M.; Mueller, F.; Passerini, S.; Bresser, D. Diagnosis Tools for Humidity-Born Surface Contaminants on Li[Ni0.8Mn0.1Co0.1]O2 Cathode Materials for Lithium Batteries. *J. Power Sources* **2022**, *525*. https://doi.org/10.1016/j.jpowsour.2022.231111.

(12)   Hawley, W. B.; Parejiya, A.; Bai, Y.; Meyer, H. M.; Wood, D. L.; Li, J. Lithium and Transition Metal Dissolution Due to Aqueous Processing in Lithium-Ion Battery Cathode

Active Materials. *J. Power Sources* **2020**, *466*. https://doi.org/10.1016/j.jpowsour.2020.228315.

(13) Yi, T. F.; Mei, J.; Zhu, Y. R. Key Strategies for Enhancing the Cycling Stability and Rate Capacity of LiNi0.5Mn1.5O4 as High-Voltage Cathode Materials for High Power Lithium-Ion Batteries. *Journal of Power Sources*. Elsevier B.V. June 1, **2016**, pp 85–105. https://doi.org/10.1016/j.jpowsour.2016.03.070.

(14) Fink Elkjaer, C.; Højberg, J. *Technical status for Haldor Topsoe LNMO material TBM-129 high-voltage LNMO spinel material*. https://engage.topsoe.com/y1050501368 (accessed 2023-10-24).

(15) Demeaux, J.; Caillon-Caravanier, M.; Galiano, H.; Lemordant, D.; Claude-Montigny, B. LiNi0.4Mn1.6O4 /Electrolyte and Carbon Black/Electrolyte High Voltage Interfaces: To Evidence the Chemical and Electronic Contributions of the Solvent on the Cathode-Electrolyte Interface Formation. *J. Electrochem. Soc.* **2012**, *159* (11), A1880–A1890. https://doi.org/10.1149/2.052211jes.

(16) Yao, W.; Chouchane, M.; Li, W.; Bai, S.; Liu, Z.; Li, L.; Chen, A. X.; Sayahpour, B.; Shimizu, R.; Raghavendran, G.; Schroeder, M. A.; Chen, Y. T.; Tan, D. H. S.; Sreenarayanan, B.; Waters, C. K.; Sichler, A.; Gould, B.; Kountz, D. J.; Lipomi, D. J.; Zhang, M.; Meng, Y. S. A 5 V-Class Cobalt-Free Battery Cathode with High Loading Enabled by Dry Coating. *Energy Environ. Sci.* **2023**, *16* (4), 1620–1630. https://doi.org/10.1039/d2ee03840d.

(17) Metzger, M.; Sicklinger, J.; Haering, D.; Kavakli, C.; Stinner, C.; Marino, C.; Gasteiger, H. A. Carbon Coating Stability on High-Voltage Cathode Materials in H2O-Free and H2O-Containing Electrolyte. *J. Electrochem. Soc.* **2015**, *162* (7), A1227–A1235. https://doi.org/10.1149/2.0461507jes.

(18) Metzger, M.; Marino, C.; Sicklinger, J.; Haering, D.; Gasteiger, H. A. Anodic Oxidation of Conductive Carbon and Ethylene Carbonate in High-Voltage Li-Ion Batteries Quantified by On-Line Electrochemical Mass Spectrometry. *J. Electrochem. Soc.* **2015**, *162* (7), A1123–A1134. https://doi.org/10.1149/2.0951506jes.

(19) Isozumi, H.; Kubota, K.; Tatara, R.; Horiba, T.; Hida, K.; Matsuyama, T.; Yasuno, S.; Komaba, S. Impact of Newly Developed Styrene–Butadiene–Rubber Binder on the Electrode Performance of High-Voltage LiNi0.5Mn1.5O4 Electrode. *ACS Appl. Energy Mater.* **2020**, *3* (8), 7978–7987. https://doi.org/10.1021/acsaem.0c01334.

(20) Yabuuchi, N.; Kinoshita, Y.; Misaki, K.; Matsuyama, T.; Komaba, S. Electrochemical Properties of LiCoO2 Electrodes with Latex Binders on High-Voltage Exposure. *J. Electrochem. Soc.* **2015**, *162* (4), A538. https://doi.org/10.1149/2.0151504jes.

(21) Gelinski, E. Coagulation, Fouling, and Mixing during VDF Emulsion Polymerization, Doctoral Dissertation, l'Université Claude Bernard Lyon, 2023. https://theses.hal.science/tel-03967165.

(22) Bichon, M.; Sotta, D.; De Vito, E.; Porcher, W.; Lestriez, B. Performance and Ageing Behavior of Water-Processed LiNi0.5Mn0.3Co0.2O2/Graphite Lithium-Ion Cells. *J. Power Sources* **2021**, *483*. https://doi.org/10.1016/j.jpowsour.2020.229097.

(23) He, J.; Melinte, G.; Darma, M. S. D.; Hua, W.; Das, C.; Schökel, A.; Etter, M.; Hansen, A. L.; Mereacre, L.; Geckle, U.; Bergfeldt, T.; Sun, Z.; Knapp, M.; Ehrenberg, H.; Maibach, J. Surface Structure Evolution and Its Impact on the Electrochemical Performances of Aqueous-Processed High-Voltage Spinel LiNi0.5Mn1.5O4 Cathodes in Lithium-Ion Batteries. *Adv. Funct. Mater.* **2022**. https://doi.org/10.1002/adfm.202207937.

(24) Kuenzel, M.; Bresser, D.; Diemant, T.; Carvalho, D. V.; Kim, G. T.; Behm, R. J.; Passerini, S. Complementary Strategies Toward the Aqueous Processing of High-Voltage LiNi0.5Mn1.5O4 Lithium-Ion Cathodes. *ChemSusChem* **2018**, *11* (3), 562–573. https://doi.org/10.1002/cssc.201702021.

(25) Romoli, L.; Lutey, A. H. A.; Lazzini, G. Laser Texturing of Li-Ion Battery Electrode Current Collectors for Improved Active Layer Interface Adhesion. *CIRP Ann.* **2022**, *71* (1), 481–484. https://doi.org/10.1016/j.cirp.2022.04.034.

(26) Kierzek, K. Influence of Binder Adhesion Ability on the Performance of Silicon/Carbon Composite as Li-Ion Battery Anode. *J. Mater. Eng. Perform.* **2016**, *25* (6), 2326–2330. https://doi.org/10.1007/s11665-016-2083-7.

(27) Jeschull, F.; Brandell, D.; Wohlfahrt-Mehrens, M.; Memm, M. Water-Soluble Binders for Lithium-Ion Battery Graphite Electrodes: Slurry Rheology, Coating Adhesion, and Electrochemical Performance. *Energy Technol.* **2017**, *5* (11), 2108–2118. https://doi.org/10.1002/ente.201700200.

(28) Ibing, L.; Gallasch, T.; Schneider, P.; Niehoff, P.; Hintennach, A.; Winter, M.; Schappacher, F. M. Towards Water Based Ultra-Thick Li Ion Battery Electrodes – A Binder Approach. *J. Power Sources* **2019**, *423*, 183–191. https://doi.org/10.1016/j.jpowsour.2019.03.020.

(29) Sahore, R.; Wood, M.; Kukay, A.; Du, Z.; Livingston, K. M.; Iii, D. L. W.; Li, J. Performance of Different Water-Based Binder Formulations for Ni-Rich Cathodes Evaluated in LiNi0.8Mn0.1Co0.1O2//Graphite Pouch Cells. *J. Electrochem. Soc.* **2022**, *169* (4). https://doi.org/10.1149/1945-7111/ac682d.

(30) Lee, J. T.; Chu, Y. J.; Peng, X. W.; Wang, F. M.; Yang, C. R.; Li, C. C. A Novel and Efficient Water-Based Composite Binder for LiCoO2 Cathodes in Lithium-Ion Batteries. *J. Power Sources* **2007**, *173* (2 SPEC. ISS.), 985–989. https://doi.org/10.1016/j.jpowsour.2007.07.073.

(31) Borah, R.; Hughson, F. R.; Johnston, J.; Nann, T. On Battery Materials and Methods. *Mater. Today Adv.* **2020**, *6*, 100046. https://doi.org/10.1016/j.mtadv.2019.100046.

(32) Neeb, C. *Development perspectives for lithium-ion battery cell formats*. https://www.isi.fraunhofer.de/en/blog/themen/batterie-update/lithium-ionen-batteriezellen-entwicklung-batteriezellformate.html (accessed 2024-10-15).

(33) Murray, V.; Hall, D. S.; Dahn, J. R. A Guide to Full Coin Cell Making for Academic Researchers. *J. Electrochem. Soc.* **2019**, *166* (2), A329–A333. https://doi.org/10.1149/2.1171902jes.

(34) Yoo, S.; Hong, C.; Chong, K. T.; Seul, N. Analysis of Pouch Performance to Ensure Impact Safety of Lithium-Ion Battery. *Energies* **2019**, *12* (15), 1–10.

https://doi.org/10.3390/en12152865.

(35) Birke, K. P.; Schweitzer, D. N. Fundamental Aspects of Achievable Energy Densities in Electrochemical Cells. In *Modern Battery Engineering*; WORLD SCIENTIFIC, 2018; pp 1–30. https://doi.org/10.1142/9789813272163_0001.

(36) Hambitzer, G.; Pinkwart, K.; Ripp, C.; Schiller, C. Thermodynamics and Mechanistics. In *Handbook of Battery Materials*; Wiley-VCH Verlag: Weinheim, 1998; pp 1–17. https://doi.org/10.1002/9783527611676.ch1.

(37) Deng, C.; Li, X.; Chen, R.; Ye, K.; Lipton, J.; Maclean, S. A.; Wang, H.; Taylor, A. D.; Weng, G. M. Recent Advances in Rocking Chair Batteries and Beyond. *Energy Storage Mater.* **2023**, *60* (April). https://doi.org/10.1016/j.ensm.2023.102820.

(38) Ghiji, M.; Novozhilov, V.; Moinuddin, K.; Joseph, P.; Burch, I.; Suendermann, B.; Gamble, G. A Review of Lithium-Ion Battery Fire Suppression. *Energies* **2020**, *13* (19), 1–30. https://doi.org/10.3390/en13195117.

(39) Cholewinski, A.; Si, P.; Uceda, M.; Pope, M.; Zhao, B. Polymer Binders: Characterization and Development toward Aqueous Electrode Fabrication for Sustainability. *Polymers (Basel).* **2021**, *13* (4). https://doi.org/10.3390/polym13040631.

(40) Liu, G.; Zheng, H.; Kim, S.; Deng, Y.; Minor, A. M.; Song, X.; Battaglia, V. S. Effects of Various Conductive Additive and Polymeric Binder Contents on the Performance of a Lithium-Ion Composite Cathode. *J. Electrochem. Soc.* **2008**, *155* (12), A887. https://doi.org/10.1149/1.2976031.

(41) Liu, G.; Zheng, H.; Song, X.; Battaglia, V. S. Particles and Polymer Binder Interaction: A Controlling Factor in Lithium-Ion Electrode Performance. *J. Electrochem. Soc.* **2012**, *159* (3), A214–A221. https://doi.org/10.1149/2.024203jes.

(42) Gyulai, A. Dry Manufacturing of Lithium-Ion Battery Cathodes by Direct Powder Compaction in a Two-Roll Calender; Doctoral Dissertation, Karlsruher Institut für Technologie (KIT), 2024. https://doi.org/10.5445/IR/1000170189.

(43) Armand, M.; Axmann, P.; Bresser, D.; Copley, M.; Edström, K.; Ekberg, C.; Guyomard, D.; Lestriez, B.; Novák, P.; Petranikova, M.; Porcher, W.; Trabesinger, S.; Wohlfahrt-Mehrens, M.; Zhang, H. Lithium-Ion Batteries – Current State of the Art and Anticipated Developments. *J. Power Sources* **2020**, *479*. https://doi.org/10.1016/j.jpowsour.2020.228708.

(44) Schmitt, M.; Baunach, M.; Wengeler, L.; Peters, K.; Junges, P.; Scharfer, P.; Schabel, W. Slot-Die Processing of Lithium-Ion Battery Electrodes- Coating Window Characterization. *Chem. Eng. Process. Process Intensif.* **2013**, *68*, 32–37. https://doi.org/10.1016/j.cep.2012.10.011.

(45) Wood, D. L.; Li, J.; Daniel, C. Prospects for Reducing the Processing Cost of Lithium Ion Batteries. *J. Power Sources* **2015**, *275*, 234–242. https://doi.org/10.1016/j.jpowsour.2014.11.019.

(46) Susarla, N.; Ahmed, S.; Dees, D. W. Modeling and Analysis of Solvent Removal during Li-Ion Battery Electrode Drying. *J. Power Sources* **2018**, *378*, 660–670.

https://doi.org/10.1016/j.jpowsour.2018.01.007.

(47) Goldbach, J. T.; Amin-Sanayei, R.; He, W.; Henry, J.; Kosar, W.; Lefebvre, A.; O'Brien, G.; Vaessen, D.; Wood, K.; Zerafati, S. Commercial Synthesis and Applications of Poly(Vinylidene Fluoride). In *Fluorinated Polymers: Volume 2: Applications*; Ameduri, B., Sawada, H., Ameduri, B., Sawada, H., Eds.; The Royal Society of Chemistry, 2016; Vol. 2, p 0. https://doi.org/10.1039/9781782629368-00127.

(48) Guerre, M.; Wahidur Rahaman, S. M.; Améduri, B.; Poli, R.; Ladmiral, V. RAFT Synthesis of Well-Defined PVDF-b-PVAc Block Copolymers. *Polym. Chem.* **2016**, *7* (45), 6918–6933. https://doi.org/10.1039/C6PY01247G.

(49) Pan, M.; Song, S.; Guo, X.; Yuan, J.; Pan, Z. Surface Nucleation-Induced Raspberry-like PVDF@P(St-Co-MPS-Co-AA) Core–Shell Latex Particles via Seeded Emulsion Polymerization and Their High Efficiency for Confined Crystallization of PVDF in Nanospheres. *Ind. Eng. Chem. Res.* **2023**, *62* (43), 17731–17742. https://doi.org/10.1021/acs.iecr.3c02493.

(50) Amin-Sanayei, R.; He, W. Chapter 10 - Application of Polyvinylidene Fluoride Binders in Lithium-Ion Battery; Nakajima, T., Groult, H. B. T.-A. F.-B. M. for E. C., Eds.; Elsevier, 2015; pp 225–235. https://doi.org/10.1016/B978-0-12-800679-5.00010-5.

(51) Spreafico, M. A.; Cojocaru, P.; Magagnin, L.; Triulzi, F.; Apostolo, M. PVDF Latex As a Binder for Positive Electrodes in Lithium-Ion Batteries. *Ind. Eng. Chem. Res.* **2014**, *53* (22), 9094–9100. https://doi.org/10.1021/ie403239s.

(52) Streitberger, H.-J.; Goldschmidt, A. *BASF Handbook Basics of Coating Technology*; Vincentz Network, 2018. https://doi.org/10.1515/9783748600251.

(53) Ebnesajjad, S.; Landrock, A. H. Introduction and Adhesion Theories. In *Adhesives Technology Handbook*; Elsevier, 2015; pp 1–18. https://doi.org/10.1016/b978-0-323-35595-7.00001-2.

(54) Allen, K. W. Some Reflections on Contemporary Views of Theories of Adhesion. *Int. J. Adhes. Adhes.* **1993**, *13* (2), 67–72. https://doi.org/10.1016/0143-7496(93)90015-2.

(55) Billot, N.; Günther, T.; Schreiner, D.; Stahl, R.; Kranner, J.; Beyer, M.; Reinhart, G. Investigation of the Adhesion Strength along the Electrode Manufacturing Process for Improved Lithium-Ion Anodes. *Energy Technol.* **2020**, *8* (2). https://doi.org/10.1002/ente.201801136.

(56) Wake, W. C. Theories of Adhesion and Uses of Adhesives: A Review. *Polymer (Guildf).* **1978**, *19* (3), 291–308. https://doi.org/10.1016/0032-3861(78)90223-9.

(57) Derjaguin, B. V; Krotova, N. A. Elektricheskaya Teoriya Adgezii Plenok k Tverdym Poverkhostyam i Ee Eksperimental'noe Obosnovanie (The Electrical Theory of Adhesion of Films to Solid Surfaces and Its Experimental Justification). *Usp. Fiz. Nauk* **1948**, *36*, 387–406.

(58) Voyutskii, S. S.; Vakula, V. L. The Role of Diffusion Phenomena in Polymer-to-polymer Adhesion. *J. Appl. Polym. Sci.* **1963**, *7* (2), 475–491. https://doi.org/10.1002/app.1963.070070207.

(59) Derjaguin, B. V.; Smilga, V. P. Electronic Theory of Adhesion. *J. Appl. Phys.* **1967**, *38* (12), 4609–4616. https://doi.org/10.1063/1.1709192.

(60) Petrie, E. M. 8 - Adhesive Bonding of Textiles: Principles, Types of Adhesive and Methods of Use. In *Joining Textiles*; Woodhead Publishing: Sawston, 2013; pp 225–274. https://doi.org/10.1533/9780857093967.2.225.

(61) Flowers, P.; Theopold, K.; Langley, R.; Neth, E. J.; Robinson, W. R. Strengths of Ionic and Covalent Bonds. In *Chemistry: Atoms First 2e*; OpenStax, 2019.

(62) Peterangelo, S. C.; Seybold, P. G. Modeling Molecular Boiling Points Using Computed Interaction Energies. *J. Mol. Model.* **2017**, *24* (1), 21. https://doi.org/10.1007/s00894-017-3552-0.

(63) van Oss, C. J. *Interfacial Forces in Aqueous Media*; CRC Press: Boca Raton, 2006; Vol. 2nd ed. https://doi.org/10.1201/9781420015768.

(64) Weber, A.; Keim, N.; Koch, P.; Müller, M.; Bauer, W.; Ehrenberg, H. The Impact of Binder Polarity on the Properties of Aqueously Processed Positive and Negative Electrodes for Lithium-Ion Batteries. *Sci. Rep.* **2025**, *15* (1), 10024. https://doi.org/10.1038/s41598-025-93813-9.

(65) Young, T. An Essay on the Cohesion of Fluids. *Philos. Trans. R. Soc. London* **1805**, *95*, 65–87. https://doi.org/10.1098/rstl.1805.0005.

(66) Law, K.-Y.; Zhao, H. Determination of Solid Surface Tension by Contact Angle. In *Surface Wetting: Characterization, Contact Angle, and Fundamentals*; Law, K.-Y., Zhao, H., Eds.; Springer International Publishing: Cham, 2016; pp 135–148. https://doi.org/10.1007/978-3-319-25214-8_7.

(67) Huhtamäki, T.; Tian, X.; Korhonen, J. T.; Ras, R. H. A. Surface-Wetting Characterization Using Contact-Angle Measurements. *Nat. Protoc.* **2018**, *13* (7), 1521–1538. https://doi.org/10.1038/s41596-018-0003-z.

(68) Ponomar, M.; Krasnyuk, E.; Butylskii, D.; Nikonenko, V.; Wang, Y.; Jiang, C.; Xu, T.; Pismenskaya, N. Sessile Drop Method: Critical Analysis and Optimization for Measuring the Contact Angle of an Ion-Exchange Membrane Surface. *Membranes*. 2022. https://doi.org/10.3390/membranes12080765.

(69) Marmur, A. *Contact Angle, Wettability and Adhesion, Volume 6*; Mittal, K. L., Ed.; CRC Press, 2009. https://doi.org/10.1201/b12247.

(70) Dupré, A.; Dupré, P. *Théorie Mécanique de La Chaleur*; Landmarks of Science; Gauthier-Villars: Paris, 1869.

(71) Fowkes, F. M. Determination of Interfacial Tensions, Contact Angles, and Dispersion Forces in Surfaces by Assuming Additivity of Intermolecular Interactions in Surfaces. *J. Phys. Chem.* **1962**, *66* (2), 382. https://doi.org/10.1021/j100808a524.

(72) Fowkes, F. M. Attractive Forces at Interfaces. *Ind. Eng. Chem.* **1964**, *56* (12), 40–52. https://doi.org/10.1021/ie50660a008.

(73) Fowkes, F. M. Donor-Acceptor Interactions at Interfaces. *J. Adhes.* **1972**, *4* (2), 155–159. https://doi.org/10.1080/00218467208072219.

(74) Owens, D. K.; Wendt, R. C. Estimation of the Surface Free Energy of Polymers. *J. Appl. Polym. Sci.* **1969**, *13* (8), 1741–1747. https://doi.org/10.1002/app.1969.070130815.

(75) Rabel, W. Einige Aspekte Der Benetzungstheorie Und Ihre Anwendung Auf Die Untersuchung Und Veränderung Der Oberflächeneigenschaften von Polymeren. *Farbe und Lack* **1971**, *77* (10), 997–1005.

(76) Kaelble, D. H. Dispersion-Polar Surface Tension Properties of Organic Solids. *J. Adhes.* **1970**, *2* (2), 66–81. https://doi.org/10.1080/0021846708544582.

(77) Matavž, A.; Bobnar, V.; Malič, B. Tailoring Ink–Substrate Interactions via Thin Polymeric Layers for High-Resolution Printing. *Langmuir* **2017**, *33* (43), 11893–11900. https://doi.org/10.1021/acs.langmuir.7b02181.

(78) Etzler, F. M. Determination of the Surface Free Energy of Solids: A Critical Review. *Rev. Adhes. Adhes.* **2013**, *1* (1), 3–45. https://doi.org/10.7569/RAA.2013.097301.

(79) Kitazaki, Y.; Hata, T. Surface-Chemical Criteria for Optimum Adhesion. *J. Adhes.* **1972**, *4* (2), 123–132. https://doi.org/10.1080/00218467208072217.

(80) van Oss, C. J.; Good, R. J.; Chaudhury, M. K. The Role of van Der Waals Forces and Hydrogen Bonds in "Hydrophobic Interactions" between Biopolymers and Low Energy Surfaces. *J. Colloid Interface Sci.* **1986**, *111* (2), 378–390. https://doi.org/10.1016/0021-9797(86)90041-X.

(81) van Oss, C. J.; Ju, L.; Chaudhury, M. K.; Good, R. J. Estimation of the Polar Parameters of the Surface Tension of Liquids by Contact Angle Measurements on Gels. *J. Colloid Interface Sci.* **1989**, *128* (2), 313–319. https://doi.org/10.1016/0021-9797(89)90345-7.

(82) van Oss, C. J.; Good, R. J.; Chaudhury, M. K. Additive and Nonadditive Surface Tension Components and the Interpretation of Contact Angles. *Langmuir* **1988**, *4* (4), 884–891. https://doi.org/10.1021/la00082a018.

(83) van Oss, C. J.; Good, R. J. On the Mechanism of "Hydrophobic" Interactions. *J. Dispers. Sci. Technol.* **1988**, *9* (4), 355–362. https://doi.org/10.1080/01932698808943994.

(84) Mittal, K. L. *Physicochemical Aspects of Polymer Surfaces*; Springer: New York City, 1983; Vol. 2.

(85) Chaudhury, M. K. Interfacial Interaction between Low-Energy Surfaces. *Mater. Sci. Eng. R Reports* **1996**, *16* (3), 97–159. https://doi.org/10.1016/0927-796X(95)00185-9.

(86) van Oss, C. J.; Visser, J.; Absolom, D. R.; Omenyi, S. N.; Neumann, A. W. The Concept of Negative Hamaker Coefficients, II. Thermodynamics, Experimental Evidence and Applications. *Adv. Colloid Interface Sci.* **1983**, *18* (3–4), 133–148. https://doi.org/10.1016/0001-8686(83)87001-8.

(87) Ludwig, B.; Zheng, Z.; Shou, W.; Wang, Y.; Pan, H. Solvent-Free Manufacturing of Electrodes for Lithium-Ion Batteries. *Sci. Rep.* **2016**, *6*. https://doi.org/10.1038/srep23150.

(88) Ludwig, B.; Pan, H.; Liu, J.; Zheng, Z.; Wang, Y. Powder-Based Additive Manufacturing of Li-Ion Batteries and Micropowder Mixing Characteristics. In *Proceedings of the ASME 2017 12th International Manufacturing Science and Engineering Conference*; 2017; pp MSEC2017-2900. https://doi.org/10.1115/MSEC2017-2900.

(89) Kim, T.; Choi, W.; Shin, H.-C.; Choi, J.-Y.; Kim, J. M.; Park, M.-S.; Yoon, W.-S. Applications of Voltammetry in Lithium Ion Battery Research. *J. Electrochem. Sci. Technol* **2020**, *11* (1), 14–25. https://doi.org/10.33961/jecst.2019.00619.

(90) Wang, S.; Zhang, J.; Gharbi, O.; Vivier, V.; Gao, M.; Orazem, M. E. Electrochemical Impedance Spectroscopy. *Nat. Rev. Methods Prim.* **2021**, *1* (1), 41. https://doi.org/10.1038/s43586-021-00039-w.

(91) Saha, B.; Goebel, K. Modeling Li-Ion Battery Capacity Depletion in a Particle Filtering Framework. In *Annual Conference of the Prognostics and Health Management Society*; 2009.

(92) Douvris, C.; Vaughan, T.; Bussan, D.; Bartzas, G.; Thomas, R. How ICP-OES Changed the Face of Trace Element Analysis: Review of the Global Application Landscape. *Sci. Total Environ.* **2023**, *905*, 167242. https://doi.org/10.1016/j.scitotenv.2023.167242.

(93) Bashworth, F.; Adams, J. C. *An Attempt to Test the Theories of Capillary Action*, 1st ed.; University Press: Cambridge, 1883.

(94) Decker, E. L.; Garoff, S. Using Vibrational Noise To Probe Energy Barriers Producing Contact Angle Hysteresis. *Langmuir* **1996**, *12* (8), 2100–2110. https://doi.org/10.1021/la951021n.

(95) Washburn, E. W. The Dynamics of Capillary Flow. *Phys. Rev.* **1921**, *17* (3), 273–283. https://doi.org/10.1103/PhysRev.17.273.

(96) DataPhysics Instruments GmbH. *Dynamic Contact Angle Measuring Device and Tensiometer (DCAT) - Determining the Surface Energy of Powders via Washburn Method.* https://www.anamet.cz/wp-content/uploads/2024/06/ApplicationNote-DCAT-Washburn-method-Surface-energy-of-powders.pdf (accessed 2024-08-31).

(97) Susana, L.; Campaci, F.; Santomaso, A. C. Wettability of Mineral and Metallic Powders: Applicability and Limitations of Sessile Drop Method and Washburn's Technique. *Powder Technol.* **2012**, *226*, 68–77. https://doi.org/10.1016/j.powtec.2012.04.016.

(98) Van Oss, C. J.; Giese, R. F.; Li, Z.; Murphy, K.; Norris, J.; Chaudhury, M. K.; GOOD, R. J. Determination of Contact Angles and Pore Sizes of Porous Media by Column and Thin Layer Wicking. *J. Adhes. Sci. Technol.* **1992**, *6* (4), 413–428. https://doi.org/10.1163/156856192X00755.

(99) Ku, C.-A.; Henry, J. D.; Siriwardane, R.; Roberts, L. Particle Transfer from a Continuous Oil to a Dispersed Water Phase: Model Particle Study 1. *J. Colloid Interface Sci.* **1985**, *106* (2), 377–387. https://doi.org/10.1016/S0021-9797(85)80012-6.

(100) Rotenberg, Y.; Boruvka, L.; Neumann, A. W. Determination of Surface Tension and Contact Angle from the Shapes of Axisymmetric Fluid Interfaces. *J. Colloid Interface Sci.* **1983**, *93* (1), 169–183. https://doi.org/10.1016/0021-9797(83)90396-X.

(101) Hansen, F. K.; Rødsrud, G. Surface Tension by Pendant Drop: I. A Fast Standard Instrument Using Computer Image Analysis. *J. Colloid Interface Sci.* **1991**, *141* (1), 1–9. https://doi.org/10.1016/0021-9797(91)90296-K.

(102) Fischer, K. Neues Verfahren Zur Maßanalytischen Bestimmung Des Wassergehaltes von Flüssigkeiten Und Festen Körpern. *Angew. Chemie* **1935**, *48* (26), 394–396. https://doi.org/10.1002/ange.19350482605.

(103) Schöffski, K. Die Wasserbestimmung mit Karl-Fischer-Titration. *Chemie Unserer Zeit* **2000**, *34* (3), 170–175. https://doi.org/10.1002/1521-3781(200006)34:3<170::AID-CIUZ170>3.0.CO;2-2.

(104) Kosfeld, M.; Westphal, B.; Kwade, A. Correct Water Content Measuring of Lithium-Ion Battery Components and the Impact of Calendering via Karl-Fischer Titration. *J. Energy Storage* **2022**, *51*. https://doi.org/10.1016/j.est.2022.104398.

(105) Habenicht, G. Kleben Der Kunststoffe Und Weiterer Nichtmetallischer Werkstoffe. In *Kleben: Grundlagen, Technologien, Anwendungen*; Habenicht, G., Ed.; Springer Berlin Heidelberg: Berlin, Heidelberg, 2009; pp 645–737. https://doi.org/10.1007/978-3-540-85266-7_15.

(106) Antao, D. S.; Staack, D. A.; Fridman, A.; Farouk, B. Atmospheric Pressure Dc Corona Discharges: Operating Regimes and Potential Applications. *Plasma Sources Sci. Technol.* **2009**, *18* (3). https://doi.org/10.1088/0963-0252/18/3/035016.

(107) Louzi, V. C.; Campos, J. S. de C. Corona Treatment Applied to Synthetic Polymeric Monofilaments (PP, PET, and PA-6). *Surfaces and Interfaces* **2019**, *14*, 98–107. https://doi.org/10.1016/j.surfin.2018.12.005.

(108) Dienwiebel, I.; Diehl, M.; Heidrich, B.; Yang, X.; Winter, M.; Börner, M. Enabling Aqueous Processing for LiNi 0.5 Mn 1.5 O 4 -Based Positive Electrodes in Lithium-Ion Batteries by Applying Lithium-Based Processing Additives . *Adv. Energy Sustain. Res.* **2021**, *2* (11), 2100075. https://doi.org/10.1002/aesr.202100075.

(109) Krüss Scientific GmbH. Krüss LabDesk Library Package Build 3.2.2.3064. Krüss Scientific GmbH: Hamburg, February 7, 2014.

(110) International Organization for Standardization. ISO 813:2019 Rubber, Vulcanized or Thermoplastic - Determination of Adhesion to a Rigid Substrate - 90° Peel Method. International Organization for Standardization 2020, p 15. https://doi.org/10.31030/3205556.

(111) Landesfeind, J.; Hattendorff, J.; Ehrl, A.; Wall, W. A.; Gasteiger, H. A. Tortuosity Determination of Battery Electrodes and Separators by Impedance Spectroscopy. *J. Electrochem. Soc.* **2016**, *163* (7), A1373–A1387. https://doi.org/10.1149/2.1141607jes.

(112) Stüble, P.; Mereacre, V.; Geßwein, H.; Binder, J. R. On the Composition of LiNi0.5Mn1.5O4 Cathode Active Materials. *Adv. Energy Mater.* **2023**, *13* (10), 2203778. https://doi.org/10.1002/aenm.202203778.

(113) Sukiman, N. L.; Zhou, X.; Birbilis, N.; Hughes, A. E.; Mol, J. M. C.; Garcia, S. J.; Zhou, X.; Thompson, G. E. Durability and Corrosion of Aluminium and Its Alloys: Overview,

Property Space, Techniques and Developments. In *Aluminium Alloys*; Ahmad, Z., Ed.; IntechOpen: Rijeka, 2012; p Ch. 2. https://doi.org/10.5772/53752.

(114) Stokes-Rodriguez, K.; Fremann, J. L.; Tolchard, J. R.; Fagerli, F. H.; Wagner, N. P. Investigating the PH Buffering Effects of PAA as a Binder for the Aqueous Processing of LNMO; Battery 2030+ Annual Conference: Grenoble, 2024; p 8.

(115) Bauer, W.; Çetinel, F. A.; Müller, M.; Kaufmann, U. Effects of PH Control by Acid Addition at the Aqueous Processing of Cathodes for Lithium Ion Batteries. *Electrochim. Acta* **2019**, *317*, 112–119. https://doi.org/10.1016/j.electacta.2019.05.141.

(116) Pieczonka, N. P. W.; Borgel, V.; Ziv, B.; Leifer, N.; Dargel, V.; Aurbach, D.; Kim, J. H.; Liu, Z.; Huang, X.; Krachkovskiy, S. A.; Goward, G. R.; Halalay, I.; Powell, B. R.; Manthiram, A. Lithium Polyacrylate (LiPAA) as an Advanced Binder and a Passivating Agent for High-Voltage Li-Ion Batteries. *Adv. Energy Mater.* **2015**, *5* (23). https://doi.org/10.1002/aenm.201501008.

(117) He, J.; Melinte, G.; Darma, M. S. D.; Hua, W.; Das, C.; Schökel, A.; Etter, M.; Hansen, A. L.; Mereacre, L.; Geckle, U.; Bergfeldt, T.; Sun, Z.; Knapp, M.; Ehrenberg, H.; Maibach, J. Surface Structure Evolution and Its Impact on the Electrochemical Performances of Aqueous-Processed High-Voltage Spinel LiNi0.5Mn1.5O4 Cathodes in Lithium-Ion Batteries. *Adv. Funct. Mater.* **2022**, *32* (46). https://doi.org/10.1002/adfm.202207937.

(118) Yang, Y.; Nie, Y.; Shen, Y.; Wei, J.; He, K.; Wen, Y.; Su, J. Alginate-Xylan Biopolymer as a Multifunctional Binder for 5 V High-Voltage LNMO Electrodes. *ACS Appl. Mater. Interfaces* **2023**, *15* (21), 25909–25918. https://doi.org/10.1021/acsami.3c01369.

(119) Han, Y. K.; Yoo, J.; Yim, T. Why Is Tris(Trimethylsilyl) Phosphite Effective as an Additive for High-Voltage Lithium-Ion Batteries? *J. Mater. Chem. A* **2015**, *3* (20), 10900–10909. https://doi.org/10.1039/c5ta01253h.

(120) Song, Y. M.; Kim, C. K.; Kim, K. E.; Hong, S. Y.; Choi, N. S. Exploiting Chemically and Electrochemically Reactive Phosphite Derivatives for High-Voltage Spinel LiNi0.5Mn1.5O4 Cathodes. *J. Power Sources* **2016**, *302*, 22–30. https://doi.org/10.1016/j.jpowsour.2015.10.043.

(121) Li, Y.; Li, W.; Shimizu, R.; Cheng, D.; Nguyen, H. N.; Paulsen, J.; Kumakura, S.; Zhang, M.; Meng, Y. S. Elucidating the Effect of Borate Additive in High-Voltage Electrolyte for Li-Rich Layered Oxide Materials. *Adv. Energy Mater.* **2022**, *12* (11). https://doi.org/10.1002/aenm.202103033.

(122) Dalavi, S.; Xu, M.; Knight, B.; Lucht, B. L. Effect of Added LiBOB on High Voltage (LiNi0.5Mn1.5O4) Spinel Cathodes. *Electrochem. Solid-State Lett.* **2012**, *15* (2). https://doi.org/10.1149/2.015202esl.

(123) Stüble, P.; Geßwein, H.; Indris, S.; Müller, M.; Binder, J. R. On the Electrochemical Properties of the Fe–Ti Doped LNMO Material LiNi0.5Mn1.37Fe0.1Ti0.03O3.95. *J. Mater. Chem. A* **2022**, *10* (16), 9010–9024. https://doi.org/10.1039/D2TA00299J.

(124) Stüble, P.; Müller, M.; Bergfeldt, T.; Binder, J. R.; Hofmann, A. Cycling Stability of Lithium-Ion Batteries Based on Fe–Ti-Doped LiNi0.5Mn1.5O4 Cathodes, Graphite Anodes, and the Cathode-Additive Li3PO4. *Adv. Sci.* **2023**, *10* (24).

https://doi.org/10.1002/advs.202301874.

(125) Billon, S.; Vieillard, P. Prediction of Enthalpies of Formation of Hydrous Sulfates. *Am. Mineral.* **2015**, *100* (2–3), 615–627. https://doi.org/10.2138/am-2015-4925.

(126) Lundén, A.; Mellander, B.-E. On the Electrical Conductivity and Other Transport Properties of Molten Sodium Sulphate. *Solid State Ionics* **1991**, *48* (1), 127–129. https://doi.org/10.1016/0167-2738(91)90208-S.

(127) Bandaranayake, P. W. S. K.; Mellander, B.-E. Electrical Conductivity and Phase Diagram of the Na2SO4-CaSO4 System. *Solid State Ionics* **1988**, *26* (1), 33–36. https://doi.org/10.1016/0167-2738(88)90242-1.

(128) Wijareni, A. S.; Widiyandari, H.; Purwanto, A.; Arif, A. F.; Mubarok, M. Z. Morphology and Particle Size of a Synthesized NMC 811 Cathode Precursor with Mixed Hydroxide Precipitate and Nickel Sulfate as Nickel Sources and Comparison of Their Electrochemical Performances in an NMC 811 Lithium-Ion Battery. *Energies* **2022**, *15* (16). https://doi.org/10.3390/en15165794.

(129) Malik, M.; Chan, K. H.; Azimi, G. Review on the Synthesis of LiNixMnyCo1-x-YO2 (NMC) Cathodes for Lithium-Ion Batteries. *Mater. Today Energy* **2022**, *28*, 101066. https://doi.org/10.1016/j.mtener.2022.101066.

(130) Xing, X.; Dai, S.; Li, W.; Li, X.; Shao, Z.; Shao, H. A Facile Surfactant-Assisted Co-Precipitation Route Preparation of LiNi0.5Mn1.5O4 Cathode Material. *Ionics (Kiel).* **2023**, *29* (11), 4509–4517. https://doi.org/10.1007/s11581-023-05184-8.

(131) Alagar, S.; Madhuvilakku, R.; Mariappan, R.; Piraman, S. Synthesize of Porous LiNi0.5Mn1.5O4 Microcubes for Lithium-Ion Battery and Supercapacitor Applications. *J. Mater. Sci. Mater. Electron.* **2018**, *29* (2), 1173–1181. https://doi.org/10.1007/s10854-017-8019-7.

(132) Pieczonka, N. P. W.; Liu, Z.; Lu, P.; Olson, K. L.; Moote, J.; Powell, B. R.; Kim, J. H. Understanding Transition-Metal Dissolution Behavior in LiNi 0.5Mn1.5O4 High-Voltage Spinel for Lithium Ion Batteries. *J. Phys. Chem. C* **2013**, *117* (31), 15947–15957. https://doi.org/10.1021/jp405158m.

(133) Tsai, H.-L.; Hsieh, C.-T.; Li, J.; Gandomi, Y. A. Enabling High Rate Charge and Discharge Capability, Low Internal Resistance, and Excellent Cycleability for Li-Ion Batteries Utilizing Graphene Additives. *Electrochim. Acta* **2018**, *273*, 200–207. https://doi.org/10.1016/j.electacta.2018.03.154.

(134) BioLogic SAS. *Investigating battery aging using Differential Capacity Analysis (DCA).* https://www.biologic.net/topics/investigating-battery-ageing-using-differential-capacity-analysis-dca/ (accessed 2023-10-24).

(135) Zhu, J.; Dewi Darma, M. S.; Knapp, M.; Sørensen, D. R.; Heere, M.; Fang, Q.; Wang, X.; Dai, H.; Mereacre, L.; Senyshyn, A.; Wei, X.; Ehrenberg, H. Investigation of Lithium-Ion Battery Degradation Mechanisms by Combining Differential Voltage Analysis and Alternating Current Impedance. *J. Power Sources* **2020**, *448*. https://doi.org/10.1016/j.jpowsour.2019.227575.

(136) Bichon, M.; Sotta, D.; Dupré, N.; De Vito, E.; Boulineau, A.; Porcher, W.; Lestriez, B. Study of Immersion of LiNi0.5Mn0.3Co0.2O2 Material in Water for Aqueous Processing of Positive Electrode for Li-Ion Batteries. *ACS Appl. Mater. Interfaces* **2019**, *11* (20), 18331–18341. https://doi.org/10.1021/acsami.9b00999.

(137) Thackeray, M. M. Spinel Electrodes for Lithium Batteries. *J. Am. Ceram. Soc.* **1999**, *82* (12), 3347–3354. https://doi.org/10.1111/j.1151-2916.1999.tb02250.x.

(138) Brown, G. E.; Henrich, V. E.; Casey, W. H.; Clark, D. L.; Eggleston, C.; Felmy, A.; Goodman, D. W.; Grätzel, M.; Maciel, G.; McCarthy, M. I.; Nealson, K. H.; Sverjensky, D. A.; Toney, M. F.; Zachara, J. M. Metal Oxide Surfaces and Their Interactions with Aqueous Solutions and Microbial Organisms. *Chem. Rev.* **1999**, *99* (1), 77–174. https://doi.org/10.1021/cr980011z.

(139) Foster, J. M.; Huang, X.; Jiang, M.; Chapman, S. J.; Protas, B.; Richardson, G. Causes of Binder Damage in Porous Battery Electrodes and Strategies to Prevent It. *J. Power Sources* **2017**, *350*, 140–151. https://doi.org/10.1016/j.jpowsour.2017.03.035.

(140) Son, B.; Ryou, M.-H.; Choi, J.; Lee, T.; Yu, H. K.; Kim, J. H.; Lee, Y. M. Measurement and Analysis of Adhesion Property of Lithium-Ion Battery Electrodes with SAICAS. *ACS Appl. Mater. Interfaces* **2014**, *6* (1), 526–531. https://doi.org/10.1021/am404580f.

(141) Meyer, C.; Weyhe, M.; Haselrieder, W.; Kwade, A. Heated Calendering of Cathodes for Lithium-Ion Batteries with Varied Carbon Black and Binder Contents. *Energy Technol.* **2020**, *8* (2). https://doi.org/10.1002/ente.201900175.

(142) Zhang, J.; Zhong, H.; Zheng, C.; Xia, Y.; Liang, C.; Huang, H.; Gan, Y.; Tao, X.; Zhang, W. All-Solid-State Batteries with Slurry Coated LiNi0.8Co0.1Mn0.1O2 Composite Cathode and Li6PS5Cl Electrolyte: Effect of Binder Content. *J. Power Sources* **2018**, *391*, 73–79. https://doi.org/10.1016/j.jpowsour.2018.04.069.

(143) Baunach, M.; Jaiser, S.; Schmelzle, S.; Nirschl, H.; Scharfer, P.; Schabel, W. Delamination Behavior of Lithium-Ion Battery Anodes: Influence of Drying Temperature during Electrode Processing. *Dry. Technol.* **2016**, *34* (4), 462–473. https://doi.org/10.1080/07373937.2015.1060497.

(144) Westphal, B.; Bockholt, H.; Günther, T.; Haselrieder, W.; Kwade, A. Influence of Convective Drying Parameters on Electrode Performance and Physical Electrode Properties. *ECS Trans.* **2015**, *64* (22), 57. https://doi.org/10.1149/06422.0057ecst.

(145) Klemens, J.; Schneider, L.; Herbst, E. C.; Bohn, N.; Müller, M.; Bauer, W.; Scharfer, P.; Schabel, W. Drying of NCM Cathode Electrodes with Porous, Nanostructured Particles Versus Compact Solid Particles: Comparative Study of Binder Migration as a Function of Drying Conditions. *Energy Technol.* **2022**, *10* (4), 2100985. https://doi.org/10.1002/ente.202100985.

(146) Zhang, L.; Wu, X.; Qian, W.; Pan, K.; Zhang, X.; Li, L.; Jia, M.; Zhang, S. *Exploring More Functions in Binders for Lithium Batteries*; Springer Nature Singapore, **2023**; Vol. 6. https://doi.org/10.1007/s41918-023-00198-2.

(147) De Gennes, P. G. Wetting: Statics and Dynamics. *Rev. Mod. Phys.* **1985**, *57* (3), 827–863. https://doi.org/10.1103/RevModPhys.57.827.

XXX

(148) Pekarovicova, A.; Fleming, P. D. *Innovations in Ink on Paper Technology to Improve Printability*; Pira International: Leatherhead, 2005.

(149) Adamson, A. W.; Gast, A. P. *Physical Chemistry of Surfaces*; Interscience Publishers: New York, 1967; Vol. 150.

(150) Carroll, B. J. Physical Aspects of Detergency. *Colloids Surfaces A Physicochem. Eng. Asp.* **1993**, *74* (2–3), 131–167. https://doi.org/10.1016/0927-7757(93)80262-D.

(151) Abbott, S. *Adhesion Science: Principles and Practice*; DEStech Publications: Lancaster, 2015.

(152) Ludwig, B. J. *Solvent-Free Additive Manufacturing of Electrodes for Li-Ion Batteries*; Doctoral Dissertation, Missouri University of Science and Technology, 2019.

(153) Li, J.; Rulison, C.; Kiggans, J.; Daniel, C.; Wood, D. L. Superior Performance of LiFePO 4 Aqueous Dispersions via Corona Treatment and Surface Energy Optimization. *J. Electrochem. Soc.* **2012**, *159* (8), A1152–A1157. https://doi.org/10.1149/2.018208jes.

(154) Weber, A.; Keim, N.; Gyulai, A.; Muller, M.; Colombo, F.; Bauer, W.; Ehrenberg, H. The Role of Surface Free Energy in Binder Distribution and Adhesion Strength of Aqueously Processed LiNi0.5Mn1.5O4 Cathodes. *J. Electrochem. Soc.* **2024**, *171* (4), 040523. https://doi.org/10.1149/1945-7111/ad3a24.

(155) van Krevelen, D. W.; Te Nijenhuis, K. *Properties of Polymers*, 4th ed.; Van Krevelen, D. W., Te Nijenhuis, K., Eds.; Elsevier: Amsterdam, 2009. https://doi.org/10.1016/B978-0-08-054819-7.00002-9.

(156) Landesfeind, J.; Eldiven, A.; Gasteiger, H. A. Influence of the Binder on Lithium Ion Battery Electrode Tortuosity and Performance. *J. Electrochem. Soc.* **2018**, *165* (5), A1122–A1128. https://doi.org/10.1149/2.0971805jes.

(157) Wang, H. F.; Troxler, T.; Yeh, A. G.; Dai, H. L. Adsorption at a Carbon Black Microparticle Surface in Aqueous Colloids Probed by Optical Second-Harmonic Generation. *J. Phys. Chem. C* **2007**, *111* (25), 8708–8715. https://doi.org/10.1021/jp066873i.

(158) Mezgebe, M.; Shen, Q.; Zhang, J. Y.; Zhao, Y. W. Liquid Adsorption Behavior and Surface Properties of Carbon Blacks. *Colloids Surfaces A Physicochem. Eng. Asp.* **2012**, *403*, 25–28. https://doi.org/10.1016/j.colsurfa.2012.03.045.

(159) Krüss Scientific GmbH. *Predicting the Dispersability of Particles Application Report: AR213e Two-Component Surface Energy Characterization as a Predictor of Wettability and Dispersability*; 2000. https://www.sanyo-si.com/wp-content/uploads/kruss-ar213-en.pdf (accessed 2024-08-12).

(160) Li, C. C.; Wang, Y. W. Importance of Binder Compositions to the Dispersion and Electrochemical Properties of Water-Based LiCoO2 Cathodes. *J. Power Sources* **2013**, *227*, 204–210. https://doi.org/10.1016/j.jpowsour.2012.11.025.

(161) Srivastava, I.; Bolintineanu, D. S.; Lechman, J. B.; Roberts, S. A. Controlling Binder Adhesion to Impact Electrode Mesostructures and Transport. *ACS Appl. Mater. Interfaces*

2020, *12* (31), 34919–34930. https://doi.org/10.1021/acsami.0c08251.

(162) Li, C.-C.; Wang, Y.-W. Binder Distributions in Water-Based and Organic-Based LiCoO2 Electrode Sheets and Their Effects on Cell Performance. *J. Electrochem. Soc.* **2011**, *158* (12), A1361. https://doi.org/10.1149/2.107112jes.

(163) Barsykov, V. Z.; Khomenko, V. G. The Influence of Polymer Binders on the Performance of Cathodes for Lithium-Ion Batteries. *Mater. Sci. Appl. Chem.* **2001**, *21*, 67–71.

(164) Trembacki, B. L.; Mistry, A. N.; Noble, D. R.; Ferraro, M. E.; Mukherjee, P. P.; Roberts, S. A. Editors' Choice—Mesoscale Analysis of Conductive Binder Domain Morphology in Lithium-Ion Battery Electrodes. *J. Electrochem. Soc.* **2018**, *165* (13), E725–E736. https://doi.org/10.1149/2.0981813jes.

(165) Hu, J.; Wang, Y.; Li, D.; Cheng, Y. T. Effects of Adhesion and Cohesion on the Electrochemical Performance and Durability of Silicon Composite Electrodes. *J. Power Sources* **2018**, *397*, 223–230. https://doi.org/10.1016/j.jpowsour.2018.06.103.

(166) Spitthoff, L.; Vie, P. J. S.; Wahl, M. S.; Wind, J.; Burheim, O. S. Incremental Capacity Analysis (DQ/DV) as a Tool for Analysing the Effect of Ambient Temperature and Mechanical Clamping on Degradation. *J. Electroanal. Chem.* **2023**, *944*. https://doi.org/10.1016/j.jelechem.2023.117627.

(167) Syzdek, J.; Marcinek, M.; Kostecki, R. Electrochemical Activity of Carbon Blacks in LiPF6-Based Organic Electrolytes. *J. Power Sources* **2014**, *245*, 739–744. https://doi.org/10.1016/j.jpowsour.2013.07.033.

(168) Aurbach, D.; Markovsky, B.; Talyossef, Y.; Salitra, G.; Kim, H. J.; Choi, S. Studies of Cycling Behavior, Ageing, and Interfacial Reactions of LiNi0.5Mn1.5O4 and Carbon Electrodes for Lithium-Ion 5-V Cells. *J. Power Sources* **2006**, *162* (2 SPEC. ISS.), 780–789. https://doi.org/10.1016/j.jpowsour.2005.07.009.

(169) Westphal, B. G.; Mainusch, N.; Meyer, C.; Haselrieder, W.; Indrikova, M.; Titscher, P.; Bockholt, H.; Viöl, W.; Kwade, A. Influence of High Intensive Dry Mixing and Calendering on Relative Electrode Resistivity Determined via an Advanced Two Point Approach. *J. Energy Storage* **2017**, *11*, 76–85. https://doi.org/10.1016/j.est.2017.02.001.

(170) Oladimeji, C. F.; Moss, P. L.; Weatherspoon, M. H. Analyses of the Calendaring Process for Performance Optimization of Li-Ion Battery Cathode. *Adv. Chem.* **2016**, *2016*, 1–7. https://doi.org/10.1155/2016/7395060.

(171) Davoodabadi, A.; Li, J.; Liang, Y.; Wang, R.; Zhou, H.; Wood, D. L.; Singler, T. J.; Jin, C. Characterization of Surface Free Energy of Composite Electrodes for Lithium-Ion Batteries. *J. Electrochem. Soc.* **2018**, *165* (11), A2493–A2501. https://doi.org/10.1149/2.0341811jes.

(172) Aurbach, D. Review of Selected Electrode-Solution Interactions Which Determine the Performance of Li and Li Ion Batteries. *J. Power Sources* **2000**, *89* (2), 206–218. https://doi.org/10.1016/S0378-7753(00)00431-6.

(173) Kawamura, T.; Okada, S.; Yamaki, J. ichi. Decomposition Reaction of LiPF6-Based Electrolytes for Lithium Ion Cells. *J. Power Sources* **2006**, *156* (2), 547–554.

https://doi.org/10.1016/j.jpowsour.2005.05.084.

(174) Metzger, M.; Strehle, B.; Solchenbach, S.; Gasteiger, H. A. Origin of H 2 Evolution in LIBs: H 2 O Reduction vs. Electrolyte Oxidation . *J. Electrochem. Soc.* **2016**, *163* (5), A798–A809. https://doi.org/10.1149/2.1151605jes.

(175) Stich, M.; Pandey, N.; Bund, A. Drying and Moisture Resorption Behaviour of Various Electrode Materials and Separators for Lithium-Ion Batteries. *J. Power Sources* **2017**, *364*, 84–91. https://doi.org/10.1016/j.jpowsour.2017.08.009.

(176) Terborg, L.; Nowak, S.; Passerini, S.; Winter, M.; Karst, U.; Haddad, P. R.; Nesterenko, P. N. Ion Chromatographic Determination of Hydrolysis Products of Hexafluorophosphate Salts in Aqueous Solution. *Anal. Chim. Acta* **2012**, *714*, 121–126. https://doi.org/10.1016/j.aca.2011.11.056.

(177) Lux, S. F.; Lucas, I. T.; Pollak, E.; Passerini, S.; Winter, M.; Kostecki, R. The Mechanism of HF Formation in LiPF6 Based Organic Carbonate Electrolytes. *Electrochem. commun.* **2012**, *14* (1), 47–50. https://doi.org/10.1016/j.elecom.2011.10.026.

(178) Plakhotnyk, A. V.; Ernst, L.; Schmutzler, R. Hydrolysis in the System LiPF 6 - Propylene Carbonate - Dimethyl Carbonate - H 2O. *J. Fluor. Chem.* **2005**, *126* (1), 27–31. https://doi.org/10.1016/j.jfluchem.2004.09.027.

(179) Hestenes, J. C.; Sadowski, J. T.; May, R.; Marbella, L. E. Transition Metal Dissolution Mechanisms and Impacts on Electronic Conductivity in Composite LiNi0.5Mn1.5O4 Cathode Films. *ACS Mater. Au* **2023**, *3* (2), 88–101. https://doi.org/10.1021/acsmaterialsau.2c00060.

(180) Terborg, L.; Weber, S.; Blaske, F.; Passerini, S.; Winter, M.; Karst, U.; Nowak, S. Investigation of Thermal Aging and Hydrolysis Mechanisms in Commercial Lithium Ion Battery Electrolyte. *J. Power Sources* **2013**, *242*, 832–837. https://doi.org/10.1016/j.jpowsour.2013.05.125.

(181) Frankenberger, M.; Mock, C.; Kaden, N.; Landwehr, I.; Veitl, J.; Ophey, J.; Schälicke, G.; Görke, M.; Holeczek, H.; Kwade, A.; Dröder, K.; Pettinger, K. H. Improving Wetting Behavior and C-Rate Capability of Lithium-Ion Batteries by Plasma Activation. *Energy Technol.* **2023**, *11* (5). https://doi.org/10.1002/ente.202200636.

(182) Huttner, F.; Haselrieder, W.; Kwade, A. The Influence of Different Post-Drying Procedures on Remaining Water Content and Physical and Electrochemical Properties of Lithium-Ion Batteries. *Energy Technol.* **2020**, *8* (2). https://doi.org/10.1002/ente.201900245.

(183) Choi, N. S.; Han, J. G.; Ha, S. Y.; Park, I.; Back, C. K. Recent Advances in the Electrolytes for Interfacial Stability of High-Voltage Cathodes in Lithium-Ion Batteries. *RSC Advances*. Royal Society of Chemistry 2015, pp 2732–2748. https://doi.org/10.1039/c4ra11575a.

(184) Hofmann, A.; Höweling, A.; Bohn, N.; Müller, M.; Binder, J. R.; Hanemann, T. Additives for Cycle Life Improvement of High-Voltage LNMO-Based Li-Ion Cells. *ChemElectroChem* **2019**, *6* (20), 5255–5263. https://doi.org/10.1002/celc.201901120.

(185) Li, J.; Henry, A.; Wood, D. L.; Daniel, C. Effect of the Interface Between Current Collector

and LiNi0.5Mn0.3Co0.2O2 Composite Cathodes on the Electrode Performance. *ECS Meet. Abstr.* **2015**, *MA2015-01* (2), 552. https://doi.org/10.1149/MA2015-01/2/552.

(186) Li, H.; Wang, L.; Song, Y.; Zhang, Z.; Zhang, H.; Du, A.; He, X. Significance of Current Collectors for High Performance Conventional Lithium-Ion Batteries: A Review. *Advanced Functional Materials*. John Wiley and Sons Inc December 1, **2023**. https://doi.org/10.1002/adfm.202305515.

(187) Wang, Y. B.; Yang, Q.; Guo, X.; Yang, S.; Chen, A.; Liang, G. J.; Zhi, C. Y. Strategies of Binder Design for High-Performance Lithium-Ion Batteries: A Mini Review. *Rare Metals*. University of Science and Technology Beijing March 1, **2022**, pp 745–761. https://doi.org/10.1007/s12598-021-01816-y.

(188) Wang, Z.; Huang, T.; Liu, Z.; Yu, A. Dopamine-Modified Carboxymethyl Cellulose as an Improved Aqueous Binder for Silicon Anodes in Lithium-Ion Batteries. *Electrochim. Acta* **2021**, *389*. https://doi.org/10.1016/j.electacta.2021.138806.

(189) Hu, B.; Shkrob, I. A.; Zhang, S.; Zhang, L.; Zhang, J.; Li, Y.; Liao, C.; Zhang, Z.; Lu, W.; Zhang, L. The Existence of Optimal Molecular Weight for Poly(Acrylic Acid) Binders in Silicon/Graphite Composite Anode for Lithium-Ion Batteries. *J. Power Sources* **2018**, *378*, 671–676. https://doi.org/10.1016/j.jpowsour.2017.12.068.

(190) Chang, B.; Kim, J.; Cho, Y.; Hwang, I.; Jung, M. S.; Char, K.; Lee, K. T.; Kim, K. J.; Choi, J. W. Highly Elastic Binder for Improved Cyclability of Nickel-Rich Layered Cathode Materials in Lithium-Ion Batteries. *Adv. Energy Mater.* **2020**, *10* (29). https://doi.org/10.1002/aenm.202001069.

(191) Jeong, C. U.; Lee, S. Y.; Kim, J.; Cho, K. Y.; Yoon, S. Embossed Aluminum as a Current Collector for High-Rate Lithium Cathode Performance. *J. Power Sources* **2018**, *398*, 193–200. https://doi.org/10.1016/j.jpowsour.2018.07.079.

(192) Sakata, I.; Morita, M.; Tsuruta, N.; Morita, K. Activation of Wood Surface by Corona Treatment to Improve Adhesive Bonding. *J. Appl. Polym. Sci.* **1993**, *49* (7), 1251–1258. https://doi.org/10.1002/app.1993.070490714.

(193) Carradò, A.; Sokolova, O.; Donnio, B.; Palkowski, H. Influence of Corona Treatment on Adhesion and Mechanical Properties in Metal/Polymer/Metal Systems. *J. Appl. Polym. Sci.* **2011**, *120* (6), 3709–3715. https://doi.org/10.1002/app.33583.

(194) Hongsriphan, N.; Sanga, S. Antibacterial Food Packaging Sheets Prepared by Coating Chitosan on Corona-Treated Extruded Poly(Lactic Acid)/Poly(Butylene Succinate) Blends. *J. Plast. Film Sheeting* **2018**, *34* (2), 160–178. https://doi.org/10.1177/8756087917722585.

(195) Kendall, K. Adhesion: Molecules and Mechanics. *Science*. **1994**, *263* (5154), 1720–1725. https://doi.org/10.1126/science.263.5154.1720.

(196) Jaiser, S.; Funk, L.; Baunach, M.; Scharfer, P.; Schabel, W. Experimental Investigation into Battery Electrode Surfaces: The Distribution of Liquid at the Surface and the Emptying of Pores during Drying. *J. Colloid Interface Sci.* **2017**, *494*, 22–31. https://doi.org/10.1016/j.jcis.2017.01.063.

(197) Owens, D. K. Some Thermodynamic Aspects of Polymer Adhesion. *J. Appl. Polym. Sci.* **1970**, *14* (7), 1725–1730. https://doi.org/10.1002/app.1970.070140706.

(198) Binder, M.; Keller, E.; Bresser, D. Realization of High Mass Loading LiNi0.5Mn1.5O4 Li-Ion Cathodes Using Water-Soluble Carrageenan as Binder. *J. Power Sources* **2024**, *603* (March), 234487. https://doi.org/10.1016/j.jpowsour.2024.234487.

(199) Gyulai, A.; Bauer, W.; Ehrenberg, H. Dry Electrode Manufacturing in a Calender: The Role of Powder Premixing for Electrode Quality and Electrochemical Performance. *ACS Appl. Energy Mater.* **2023**, *6* (10), 5122–5134. https://doi.org/10.1021/acsaem.2c03755.

(200) Colombo, F.; Müller, M.; Weber, A.; Keim, N.; Jeschull, F.; Bauer, W.; Ehrenberg, H. Electrochemical Investigation of Fluorine-Containing Li-Salts as Slurry Cathode Additives for Tunable Rheology in Super High Solid Content NMP Slurries. *Energy Adv.* **2023**, *2* (12), 2093–2108. https://doi.org/10.1039/D3YA00246B.

(201) Kim, Y.; Kim, M.; Lee, T.; Kim, E.; An, M.; Park, J.; Cho, J.; Son, Y. Investigation of Mass Loading of Cathode Materials for High Energy Lithium-Ion Batteries. *Electrochem. commun.* **2023**, *147*, 107437. https://doi.org/10.1016/j.elecom.2023.107437.

(202) CATL. *CATL launches CTP 3.0 battery "Qilin," achieves the highest integration level in the world*. https://www.catl.com/en/news/958.html (accessed 2024-11-25).

(203) Kuenzel, M.; Choi, H.; Wu, F.; Kazzazi, A.; Axmann, P.; Wohlfahrt-Mehrens, M.; Bresser, D.; Passerini, S. Co-Crosslinked Water-Soluble Biopolymers as a Binder for High-Voltage LiNi0.5Mn1.5O4|Graphite Lithium-Ion Full Cells. *ChemSusChem* **2020**, *13* (10), 2650–2660. https://doi.org/10.1002/cssc.201903483.

(204) Kuenzel, M.; Porhiel, R.; Bresser, D.; Asenbauer, J.; Axmann, P.; Wohlfahrt-Mehrens, M.; Passerini, S. Deriving Structure-Performance Relations of Chemically Modified Chitosan Binders for Sustainable High-Voltage LiNi0.5Mn1.5O4 Cathodes. *Batter. Supercaps* **2020**, *3* (2), 155–164. https://doi.org/10.1002/batt.201900140.

(205) Bigoni, F.; Giorgio, F. De; Soavi, F.; Arbizzani, C. Sodium Alginate: A Water-Processable Binder in High-Voltage Cathode Formulations. *J. Electrochem. Soc.* **2016**, *164*, A6171. https://doi.org/10.1149/2.0281701jes.

(206) Haselrieder, W.; Westphal, B.; Bockholt, H.; Diener, A.; Höft, S.; Kwade, A. Measuring the Coating Adhesion Strength of Electrodes for Lithium-Ion Batteries. *Int. J. Adhes. Adhes.* **2015**, *60*, 1–8. https://doi.org/10.1016/j.ijadhadh.2015.03.002.

(207) Horvath, D. V.; Coelho, J.; Tian, R.; Nicolosi, V.; Coleman, J. N. Quantifying the Dependence of Battery Rate Performance on Electrode Thickness. *ACS Appl. Energy Mater.* **2020**, *3* (10), 10154–10163. https://doi.org/10.1021/acsaem.0c01865.

(208) Xu, R.; Huang, H.; Tian, Z.; Xie, J.; Lei, C. Effects of Coated Separator Surface Morphology on Electrolyte Interfacial Wettability and Corresponding Li–Ion Battery Performance. *Polymers (Basel).* **2020**, *12* (1), 117. https://doi.org/10.3390/polym12010117.

(209) Zheng, H.; Li, J.; Song, X.; Liu, G.; Battaglia, V. S. A Comprehensive Understanding of Electrode Thickness Effects on the Electrochemical Performances of Li-Ion Battery

Cathodes. *Electrochim. Acta* **2012**, *71*, 258–265. https://doi.org/10.1016/j.electacta.2012.03.161.
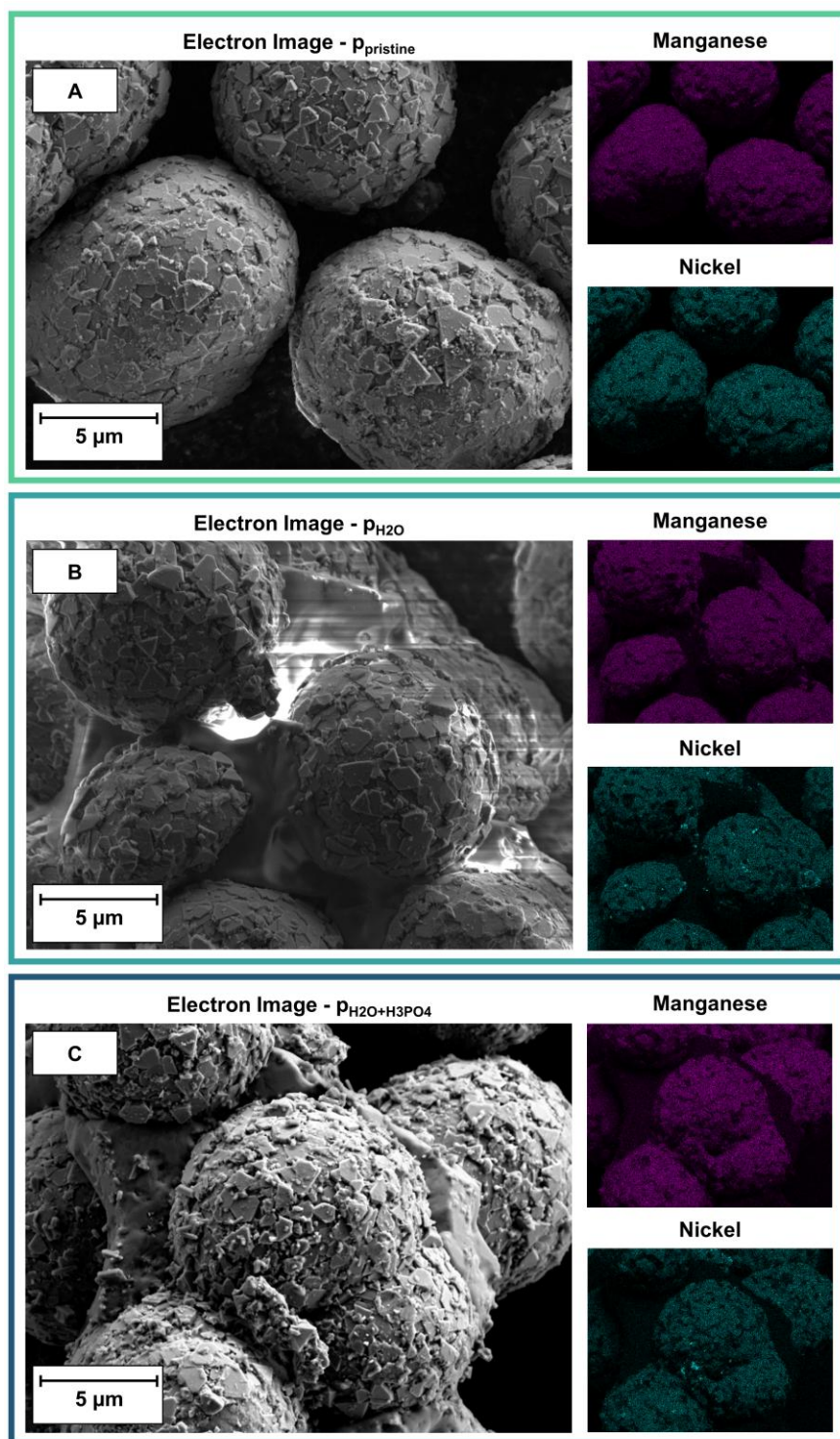
Appendix

Figure A 1 - Elemental mappings of manganese and nickel of (A) pristine LNMO, (B) LNMO submerged in H_2O for 1h and air-dried, (C) LNMO submerged in $H_2O + H_3PO_4$ for 1h and air-dried
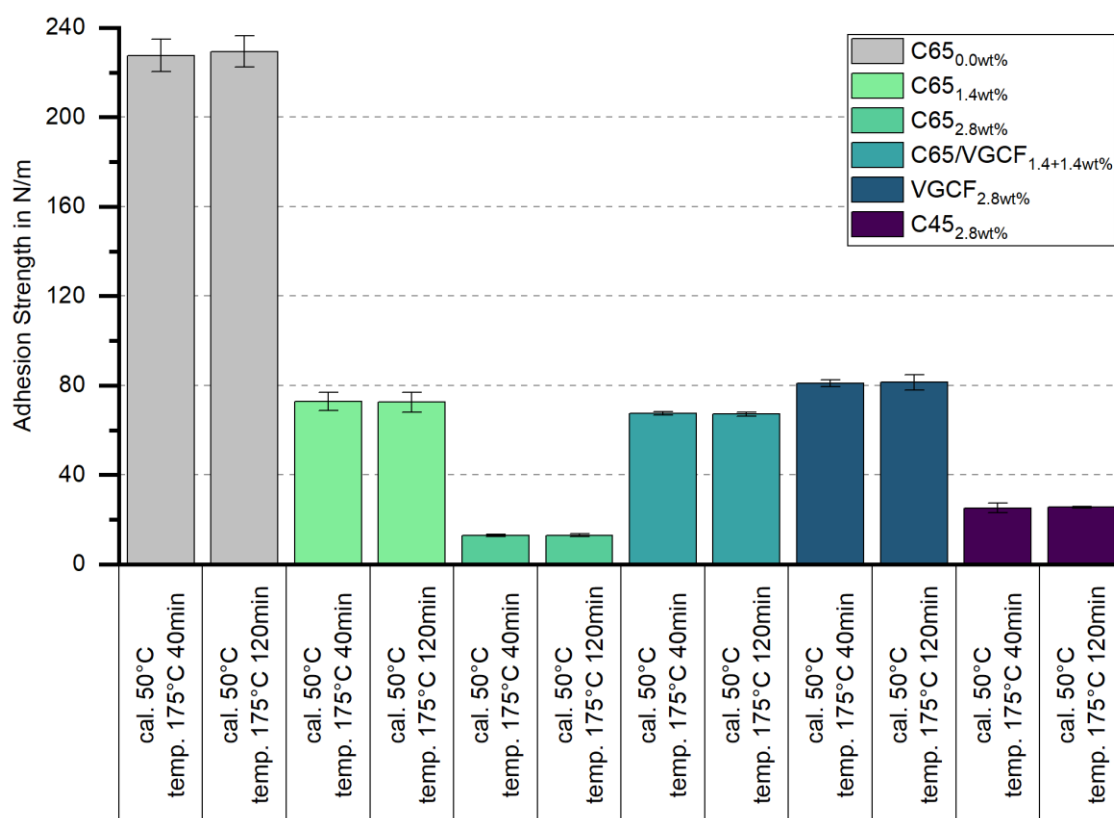
Figure A 2 - Adhesion strength of cathodes, calandered and heat-treated for 40 minutes or 120 minutes
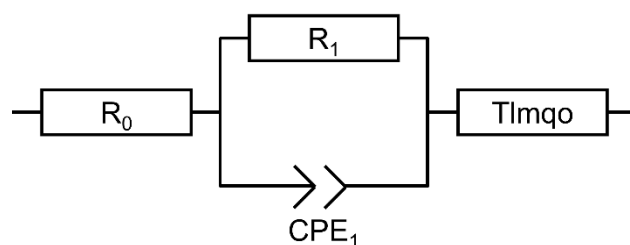
Figure A 3 - Equivalent circuit model applied for the analysis of the obtained impedance spectra according to Landesfeind et al. [111]

The internal resistance of the measurement setup is represented by resistance R_0. Resistance R_1 in parallel with constant phase element CPE_1 represent the interface between cathode and current collector. The transition line model Tlmqo according to Landesfeind et al. [111] describes the ionic resistance.

Table A 1 - Contact angle measurements of reference liquids with different electrode components obtained from sessile drop and Washhburn measurements ± standard deviation, n=3 [154]

Solid sample	n-Hexane	Water	DIM	DMSO	EG	Method
	Capillary Constant	Contact angle (degrees)				
C45	$1.7 \cdot 10^{-5}$	89.8 ± 0.1	63.9 ± 0.2	31.7 ± 2.8	-	WB
C65	$1.7 \cdot 10^{-5}$	89.6 ± 0.4	64.4 ± 1.0	38.7 ± 0.6	-	WB
VGCF	$2.0 \cdot 10^{-5}$	90.0 ± 0.1	80.9 ± 0.5	80.0 ± 3.7	-	WB
LNMO	$3.4 \cdot 10^{-6}$	42.9 ± 1.5	61.3 ± 0.5	2.8 ± 0.1	-	WB
CMC	n/a	-	38.5 ± 2.1	17.0 ± 1.8	9.4 ± 0.2	SDP
PVDF	n/a	69.1 ± 0.4	44.2 ± 0.3	-	37.4 ± 0.5	SDP
Aluminum CC	n/a	85.2 ± 1.0	47.5 ± 2.2	-	62.0 ± 0.1	SDP

Table A 2 - Contact angles of reference liquids with different PVDF latices obtained from sessile drop measurements ± standard deviation, n=3

Solid sample	Water	DIM	EG
	Contact angle (degrees)		
Latex 1	79.7 ± 0.7	45.9 ± 0.3	45.3 ± 0.7
Latex 2	72.1 ± 0.4	43.4 ± 0.3	37.7 ± 0.1
Latex 3	61.5 ± 0.5	36.4 ± 1.8	42.3 ± 0.4
Latex 4	38.2 ± 0.7	60.6 ± 2.5	35.4 ± 0.2

Table A 3 - Contact angles of reference fluids with various water-soluble binders and differently treated aluminum current collectors obtained from sessile drop measurements ± standard deviation, n=3

Solid sample	Water	DIM	DMSO	EG
	Contact angle (degrees)			
PVP	-	26.3 ± 1.9	26.0 ± 1.2	47.6 ± 0.3
CAR	-	59.2 ± 0.9	33.7 ± 0.6	41.5 ± 1.4
CMC 1	-	38.5 ± 2.1	17.0 ± 1.8	9.4 ± 0.2
CMC 2	-	66.8 ± 1.8	22.6 ± 2.9	22.2 ± 2.1
Alu 0 J/cm²	85.2 ± 1.0	47.5 ± 2.2	-	62.0 ± 0.1
Alu 0.75 J/cm²	63.9 ± 0.5	30.0 ± 1.5	30.1 ± 0.6	-
Alu 1.5 J/cm²	43.1 ± 1.0	27.6 ± 0.8	17.9 ± 0.2	-
Alu 3.0 J/cm²	26.1 ± 0.3	33.1 ± 0.4	0.0 ± 0.0	-
Alu 8.5 J/cm²	30.5 ± 0.5	37.1 ± 0.9	0.0 ± 0.0	-
Alu 17.0 J/cm²	30.3 ± 0.7	37.5 ± 1.1	0.0 ± 0.0	-
Alu 25.5 J/cm²	29.3 ± 0.5	35.5 ± 0.4	0.0 ± 0.0	-

List of Publications

Peer-Reviewed Journal Papers

(J5) **Weber, A.** and Keim, N.; Koch, P.; Müller, M.; Bauer, W.; Ehrenberg, H. The Impact of Binder Polarity on the Properties of Aqueously Processed Positive and Negative Electrodes for Lithium-Ion Batteries. *Nature Sci. Rep.* **2025**, *15*, 10024, https://doi.org/10.1038/s41598-025-93813-9.

(J4) Keim, N.; **Weber, A.**; Müller, M.; Burger, D.; Bauer, W.; Scharfer, P.; Schabel, W.; Ehrenberg, H. CMC staining method for the visualisation of the binder distribution in water-based electrodes with EDS. *ACS Appl. Energy Mater.* **2025**, *8* (7), 4501-4505, https://doi.org/10.1021/acsaem.5c00048.

(J3) Keim, N.; **Weber, A.**; Müller, M.; Kaufmann, U.; Bauer, W.; Petermann, O.; Bayer, R.; Ehrenberg, H. Understanding Key NaCMC Properties to Optimize Electrodes and Battery Performance. *Adv. Energy Sustain. Res.* **2025**, *n/a* (n/a), 2400364. https://doi.org/10.1002/aesr.202400364.

(J2) **Weber, A.**; Keim, N.; Gyulai, A.; Muller, M.; Colombo, F.; Bauer, W.; Ehrenberg, H. The Role of Surface Free Energy in Binder Distribution and Adhesion Strength of Aqueously Processed $LiNi_{0.5}Mn_{1.5}O_4$ Cathodes. *J. Electrochem. Soc.* **2024**, *171* (4), 040523. https://doi.org/10.1149/1945-7111/ad3a24.

(J1) Colombo, F.; Müller, M.; **Weber, A.**; Keim, N.; Jeschull, F.; Bauer, W.; Ehrenberg, H. Electrochemical Investigation of Fluorine-Containing Li-Salts as Slurry Cathode Additives for Tunable Rheology in Super High Solid Content NMP Slurries. *Energy Adv.* **2023**, *2* (12), 2093–2108. https://doi.org/10.1039/D3YA00246B.

Conference Posters and Oral Presentations

(C2) **Weber, A.**; Bauer, W. The Effects of the Binder's Surface Free Energy on the Properties of Aqueously Processed LNMO Cathodes. *Electrochemical Society Meeting Abstracts*. **2024**; MA2024-02(5). https://doi:10.1149/ma2024-025553mtgabs

(C1) **Weber, A.**; Bauer, W.; Ehrenberg, H. Influence of Surface Free Energy on Binder Distribution and Adhesion Strength of Aqueously Processed LNMO Cathodes. *International Battery Production Conference*. **2023**